POLITECNICO
MILANO 1863

SCUOLA DI INGEGNERIA INDUSTRIALE
E DELL'INFORMAZIONE

Universal Photonic Processors: Calibration and Operation of a 6-mode Device

TESI DI LAUREA MAGISTRALE IN
ENGINEERING PHYSICS - INGEGNERIA FISICA

Author: **Niki Di Giano**

Student ID: 945052
Advisor: Prof. Roberto Osellame
Co-advisors: Dr. Francesco Ceccarelli, Dr. Andrea Crespi
Academic Year: 2021-22

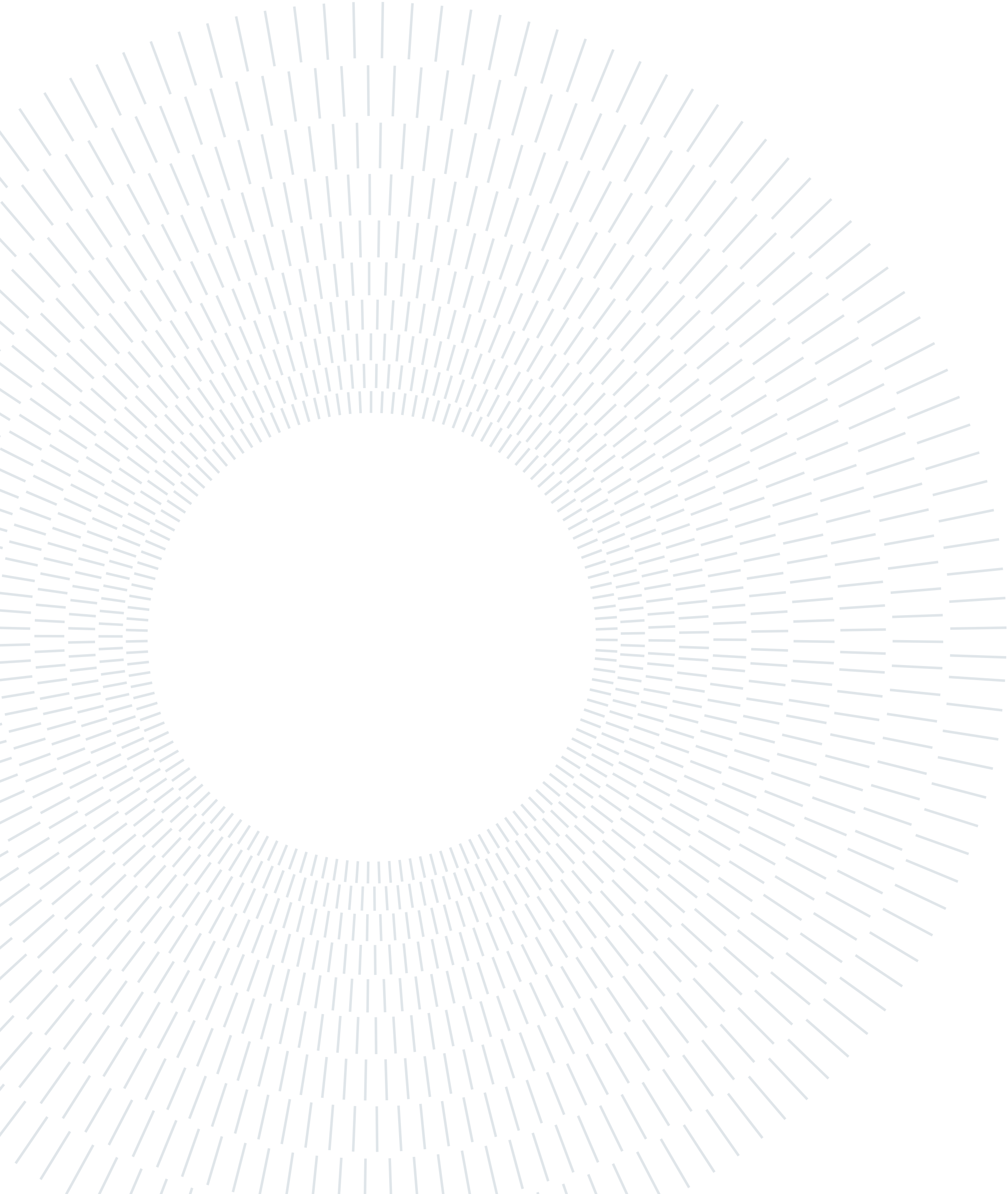

Abstract

Photonic Integrated Circuits (PICs) are a widely used platform for classical communication and today they are leading the advances in optical quantum processing and computation. In the context of an ever-growing need for techniques to realise such circuits, Femtosecond Laser Micromachining (FLM) offers a rapid and cost-effective solution for the fabrication of PICs with transversal advantages with respect to standard platforms based on planar processes.

Universal Photonic Processors (UPPs) are photonic integrated devices capable of implementing an arbitrary unitary transformation between the input and output states of light. A necessary requirement for the operation of UPPs in applications is the ability to reconfigure the chip on demand. In FLM, this is achieved by fabricating a set of electrical microheaters, deposited over the waveguides, in such a way that the phases of the light signal are modulated by exploiting the thermo-optic effect.

As the number of light modes at the input of an UPP increases, so does the number of microheaters and the complexity of the circuit's layout; therefore, it becomes increasingly difficult to calibrate independently the effect of each microheater and operate them effectively in applications.

In this work we introduce a general procedure for the calibration of an UPP fabricated through FLM featuring a square layout, with focus on the case of a 6-mode UPP. In addition, we use the results of this procedure to operate this UPP for its intended purpose of transformation implementation, implementing switching matrices - useful to route optical signals across the outputs - as well as generic Haar random matrices. We extract an average fidelity of 0.99536 ± 0.00077 on switching matrices and 0.89076 ± 0.04660 on the Haar random.

Keywords: Photonic Integrated Circuits, Femtosecond Laser Micromachining, Universal Photonic Processors, Control and calibration

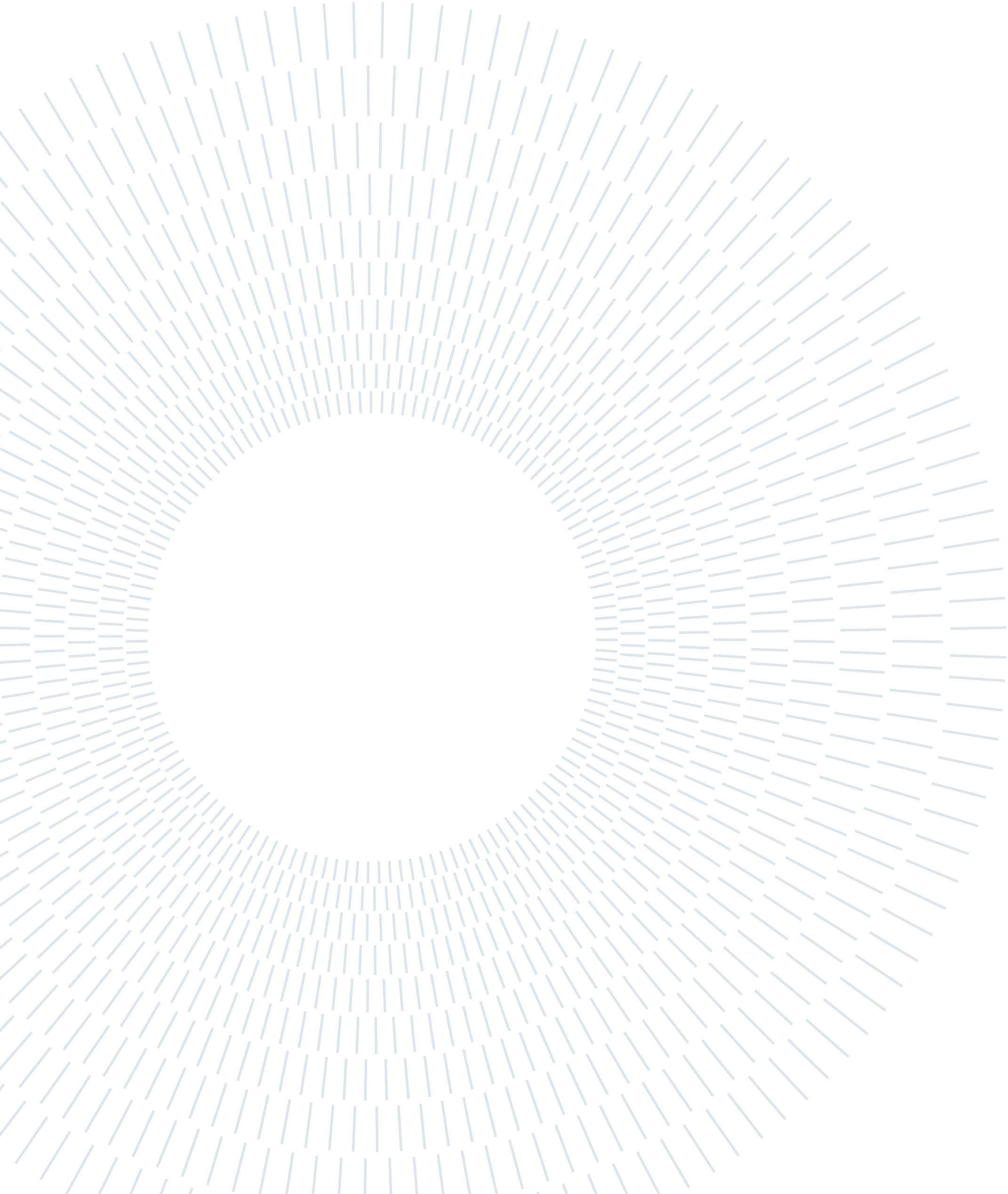

Abstract in lingua italiana

I Circuiti Fotonici Integrati (CFI) sono una piattaforma largamente usata per le telecomunicazioni e oggi guidano gli avanzamenti nell'ottica quantistica e nella computazione quantistica. Nel contesto di un bisogno sempre crescente di realizzare tali circuiti, la Scrittura Laser a Femtosecondi (SLF) offre una soluzione rapida ed efficiente per la fabbricazione di CFI offrendo vantaggi trasversali rispetto alle piattaforme standard basate su processi planari.

I Processori Fotonici Universali (PFU) sono dispositivi fotonici integrati capaci di implementare una trasformazione unitaria qualsiasi fra gli stati quantici della luce tra ingresso e uscita. Un requisito necessario per operare i PFU nelle applicazioni è l'abilità di riconfigurare il chip. In SLF, è possibile fabbricare dei micro-riscaldatori elettronici depositati sopra le guide d'onda, in modo che le fasi del segnale ottico siano modulate attraverso l'effetto termo-ottico.

Aumentando il numero di modi in ingresso al PFU aumentano anche il numero di micro-riscaldatori e la complessità del dispositivo; per questi motivi diventa sempre più difficile calibrare indipendentemente l'effetto di ciascun micro-riscaldatore ed operarli in modo efficace per le applicazioni.

In questo lavoro introduciamo un metodo generale per la calibrazione di un PFU fabbricato con SLF in una configurazione quadrata, con attenzione al caso di un PFU a 6 modi. Inoltre, utilizziamo i risultati di questa procedura per operare il PFU per il suo utilizzo primario di implementazione matrici, implementando matrici di switching - utili per dirigere il segnale da un ingresso verso le varie uscite - e generiche matrici random Haar. Troviamo una fidelity media di 0.99536 ± 0.00077 per le matrici di switching e 0.89076 ± 0.04660 per le Haar random.

Parole chiave: Circuiti di Ottica Integrata, Scrittura Laser a Femtosecondi, Processori Ottici Universali, Controllo e calibrazione

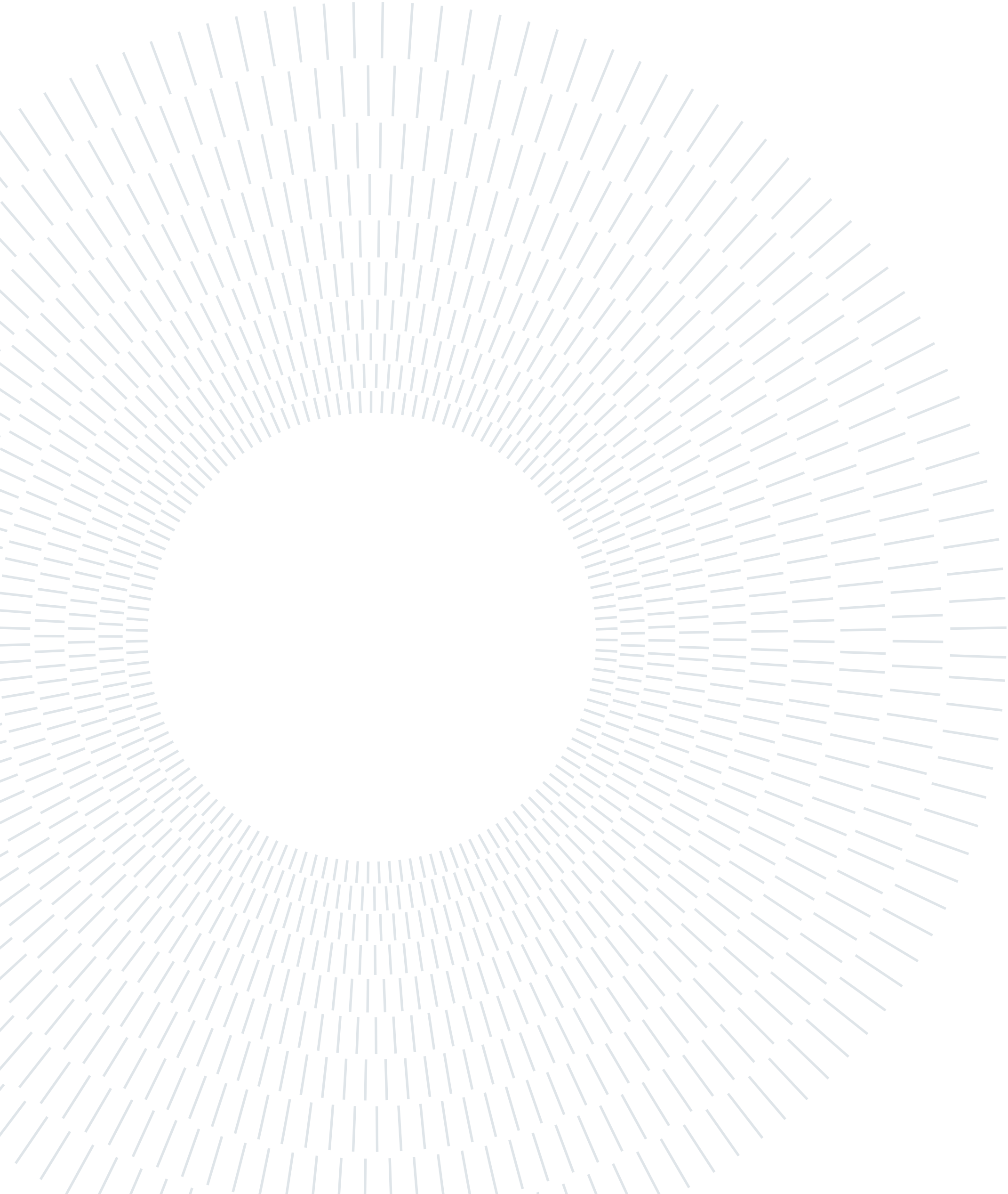

Contents

Abstract **i**

Abstract in lingua italiana **iii**

Contents **v**

1 Introduction **1**

2 Integrated Photonics **3**

- 2.1 Integrated Photonics Building Blocks . . . 3
  - 2.1.1 Optical Waveguides . . . 3
  - 2.1.2 Coupled Waveguides . . . 5
  - 2.1.3 Directional Coupler . . . 7
- 2.2 Universal Photonic Processors . . . 9
  - 2.2.1 Reconfigurable Mach-Zehnder Interferometer . . . 9
  - 2.2.2 Universal Photonic Processors . . . 10
  - 2.2.3 UPP Programming and Control . . . 11
  - 2.2.4 Clements' Decomposition Algorithm . . . 13
  - 2.2.5 Applications of UPPs . . . 16

3 Fabrication Platforms for Integrated Photonics **19**

- 3.1 Planar Fabrication Processes . . . 19
  - 3.1.1 Silicon on Insulator . . . 19
  - 3.1.2 Silica on Silicon . . . 23
  - 3.1.3 Silicon Nitride . . . 25
- 3.2 Direct Laser Writing . . . 27
  - 3.2.1 Principles of FLM Physics . . . 27
  - 3.2.2 FLM Integrated Photonic Circuits . . . 29
  - 3.2.3 Thermal Phase Shifting in FLM Integrated Photonic Circuits . . . 30

3.2.4 Thermal Isolation Structures 33

4 Materials and Methods 37

4.1 6-Mode UPPs 37

4.2 Classical Light Coupling 39

4.3 Electronics and Current Control 40

4.4 Automated Stages 42

5 Calibration of the 6-mode UPP 45

5.1 Linear Model of Thermal Phase Shifting 46

5.1.1 Nonlinearity 47

5.2 Calibration of Internal Phases 50

5.2.1 Cross-Talk 53

5.3 Calibration of External Phases 57

5.3.1 Measurable Static Phases and Equivalent Circuits 59

5.3.2 Cross-Talk of External Phases 61

6 Operation of the 6-mode UPP 65

6.1 Operating the Device without Clements' Algorithm 65

6.1.1 Existence of Solutions 66

6.2 Results of the Experiments 67

6.2.1 Switching Matrices 68

6.2.2 Random Haar Matrices 69

6.3 Common Mode Phase 72

6.3.1 Thermal Cross-talk and Common Mode Phase 74

7 Conclusions and Future Developments 79

Bibliography 81

List of Figures 87

List of Tables 93

Acknowledgements 95

1 | Introduction

Universal Photonic Processors (UPPs) are a type of photonic integrated device built from a network of reconfigurable Mach-Zehnder Interferometers (MZIs). These devices are capable of implementing an arbitrary unitary transformation between different modes, which makes them valuable assets in quantum computation, quantum metrology, and quantum communications. The main feature of UPPs is the possibility to reconfigure the chip on demand; they can implement unitary transformations by controlling the phase shifts on the optical signal and by making the signal interfere with itself.

Several different fabrication platforms are available to realise UPPs. Planar processes are a widely common platform for the realisation of photonic integrated devices in general, and nowadays they stand as a solid technology for the fabrication of UPPs. Planar processes, however, are not the only possibility, as direct writing platforms are available: in this landscape, Femtosecond Laser Micromachining (FLM) is a flexible fabrication platform that offers a plethora of tools to build UPPs and photonic integrated devices in general. In FLM, we employ laser light to impress the design of the layout directly into the substrate. Reconfigurable devices such as UPPs can be fabricated using FLM by exploiting the thermo-optic effect: by depositing a set of resistive microheaters it becomes possible to induce phase shifts on the waveguides by controlling the current flowing through the microheaters.

Operating UPP devices amounts to choosing the correct phase shifts to achieve a specific unitary transformation. Doing so, however, requires a few nontrivial steps. First of all, fabrication tolerances may induce different optical lengths on two arms of an MZI. In other words, this means that after fabrication there is a random distribution of phases - which we call "static phases" - in the MZI network without any active reconfiguration. Before attempting to operate the device, then, one needs to calibrate these phases. Moreover, one needs to find the correct relationship that binds the control variable - in FLM devices, the current flowing through the microheater - and the amount of phase shifting induced. The main challenge in measuring the static phases and the relationship lies in untangling the effect of one MZI from the effect of all the other MZIs. Indeed, it becomes impossible to directly calibrate one MZI in the middle of the network without some algorithmic procedure. In the first part of this work we introduce our algorithmic procedure for the complete calibration of all phases for a network with a square layout; we identify two different kinds of phases in the UPP network, introducing a method to calibrate each. We then show the results of the procedure on two identical 6-mode UPPs fabricated using FLM. Moreover, we develop methods to take into account specific phenomena related to the technology employed to build the 6-mode UPPs, such as nonlinearity of the resistive microheaters and thermal cross-talk.

After the phases have been calibrated, the device can be operated. However, if one's aim is to implement unitary transformations, one needs a procedure to decompose such transformation into the individual phase-shifting contributions of each MZI in the network. This procedure depends on the device's layout, and Clements' algorithm is the procedure we find in the literature for a network with a square layout. The second part of this work focuses on the implementation of Clements' algorithm on the two UPP devices, together with experimental data that show the performance of each device in implementing unitary transformations.

Finally, we introduce novel methods to take into account some additional effects that Clements' algorithm does not contain. In particular, we discuss the effect of the common mode phase of an MZI on the network and we analyse the influence of thermal cross-talk on this effect. From these considerations we extract a new model for the operation of our device, and we report the experimental data confirming that our model takes into account a non-negligible cross-talk effect.

We begin in Chapter 2 by explaining the theoretical basis behind integrated photonic devices and UPPs, demonstrating Clements' algorithm. In Chapter 3 we offer a rundown of the major fabrication platforms for integrated photonics with a focus on the state of the art of UPPs, as well as an in-depth analysis of reconfigurable devices for FLM. In Chapter 4 we explain the setup and the methods used to extract the experimental data. Finally, in Chapter 5 and 6 we discuss the bulk of the work, introducing new methods for the calibration and operation of UPPs.

2 | Integrated Photonics

In this chapter we go over some of the theoretical basis for the work that follows, covering the theory of linear circuits in photonics. In Section 2.1 we begin from the very basics, introducing the elementary building blocks of integrated photonics. In Section 2.2 we cover how from these elements we can build reconfigurable integrated photonic devices starting from the smallest such device, the reconfigurable Mach-Zehnder Interferometer (MZI), all the way up to more general Universal Photonic Processors (UPPs).

2.1. Integrated Photonics Building Blocks

Integrated Photonics has been a commonly used platform in optical signal processing ever since the seminal work performed at Bell Labs in 1969 [1]. There are several advantages demonstrated its position as a solid technology for the purposes of signal processing in general: firstly, it allows for great miniaturization of optical components, which in turn vastly reduces the effects of mechanical instabilities compared to bulk optics; secondly, they allow for reconfigurable devices, which is the main focus of this work. These features make integrated photonics especially attractive for the manipulation of quantum states of light and for implementing the most recent applications of quantum communication, metrology, sensing, and quantum computation.

2.1.1. Optical Waveguides

The simplest building block of Integrated Photonics is the *optical waveguide* [2], shown in Figure 2.1. This is a guiding structure that operates on the same principle as an optical fiber, where the light is guided through the internal medium by the phenomenon of total internal reflection. The most common design is the step-index rectangular waveguide; this design features a refractive index profile $n(x, y, z)$ of the form:

$$n(x, y, z) = n_s + (n_m - n_s)\mathbb{1}_{[a,b]}(x)\mathbb{1}_{[c,d]}(y) \tag{2.1}$$

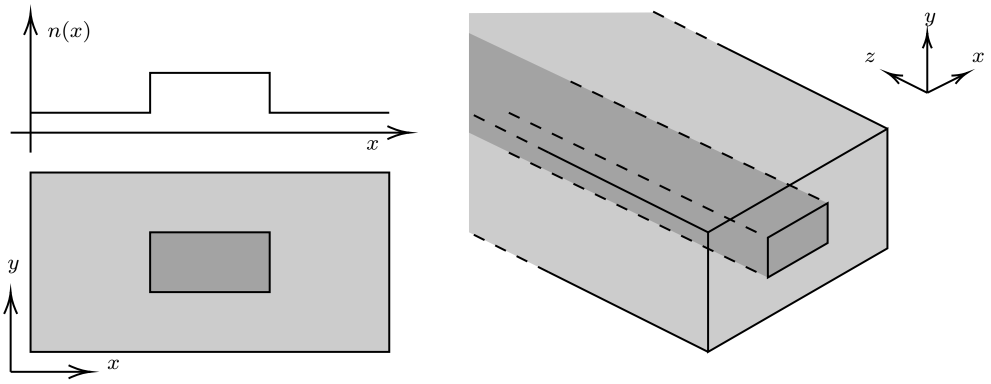

Figure 2.1: Step-index rectangular waveguide. The graph on the left shows the refractive index as a function of the x coordinate and a section of the waveguide. On the right, a three-dimensional view of the device.

where $\mathbb{1}_{[a,b]}$ is the indicator function. n_s is the refractive index of the substrate material, and n_m is the refractive index of the guiding medium. Typically $n_m > n_s$ and we operate under the assumption that $(n_m - n_s)/n_s \ll 1$, called *weakly guiding approximation.*
Maxwell's wave equation for the electric field reads:

$$\nabla^2 E = \mu\varepsilon_0\varepsilon_r \frac{\partial^2 E}{\partial t^2}. \tag{2.2}$$

Here E is the electric field, ε_0 and ε_r are respectively the dielectric constant of vacuum and the relative dielectric constant of the medium, μ is the magnetic permeability of the medium. We can assume $\mu = \mu_0$ since most materials used for optical waveguides do not show magnetic behaviour. The equation depends on the refractive index profile via $\varepsilon_r^2 = n(x, y, z)$.
Solutions to this equation cannot be obtained analytically for a general index profile, but from the continuous translational symmetry of along z it is possible to show that the solution is always of the form

$$E(x, y, z, t) = \epsilon(x, y)e^{i(\omega t - \beta z)} \tag{2.3}$$

where ϵ is the electric field profile, ω is the frequency of the electromagnetic wave, β is a spatial frequency called *propagation parameter* of the wave. Plugging this back into 2.2 and applying the weakly guiding approximation results in an eigenvalue equation [2]. From this eigenvalue problem we obtain a set of solutions for β called *optical modes*, indexed by two integer numbers: $\beta = \beta^p_{nm}$ where p represents the polarisation of the field. The number of solutions depends on the difference $n_m - n_s$, and optical waveguides are dubbed *single mode* if there is only one solution ($m = n = 0$, called *fundamental mode*) and *multimode* otherwise.

The discussion so far assumed materials with zero absorption as well as an index profile independent of z. In real devices, this is not the case; a deviation from either assumption introduces losses in the waveguide. Absorption directly decreases the optical power in the waveguide by turning the energy of the electromagnetic field into heat; deviations from continuous translational symmetry instead induce scattering events, a coupling between an optical mode of the waveguide and an optical mode of the surrounding material. Translational symmetry can be induced not only by deviations in the geometry of the waveguide, but also the mere fact that the devices have a finite length.

The effect of losses can be modeled by introducing an extra term α in Equation 2.3:

$$E(x, y, z, t) = \epsilon(x, y)e^{i(\omega t-(\beta+i\alpha)z)}. \tag{2.4}$$

Throughout this work we will not take into account losses. However, it is important to remark that they are a substantial component in the operation of integrated photonic devices as a whole.

2.1.2. Coupled Waveguides

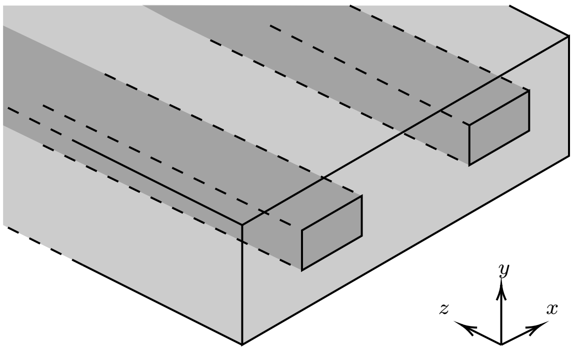

Figure 2.2: Coupled waveguides in a three-dimensional view.

The first step in complexity is achieved by placing two waveguides next to one another, as in Figure 2.2. Assuming both are single mode waveguides (with the same n_m), the distribution of the fundamental modes for each waveguide would overlap with one another. It is possible to show that in this condition there are always at least two solutions to the eigenvalue problem and they are well approximated by a sum $S(x, y, z, t)$ and a difference $A(x, y, z, t)$ of these fundamental modes, called *supermodes*. This approximation is valid as long as the waveguides are not too close to each other [2]. The profile of these modes is shown in Figure 2.3.

$S(z, t)$ and $A(z, t)$ form a basis $\{S(z, t), A(z, t)\}$ for the space of all electric fields guided

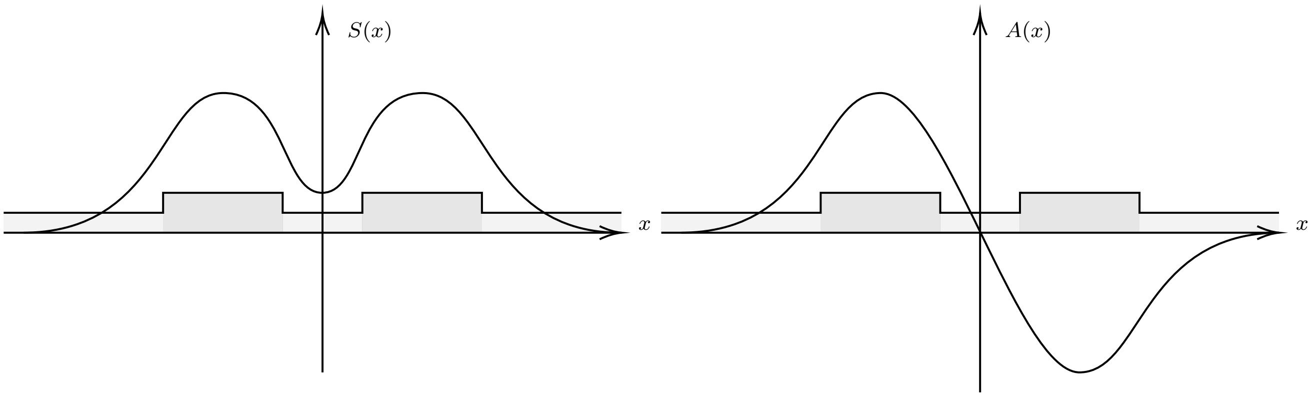

Figure 2.3: The two modes of the coupled waveguides. The refractive index profile is also shown for clarity.

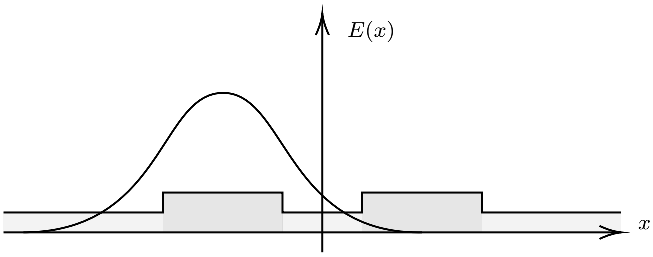

Figure 2.4: Example field distribution where all the optical power is localised in one waveguide. The refractive index profile is also shown for clarity.

within this device - again, assuming both waveguides would be single-mode when isolated. We omit the dependence on x, y for simplicity, but it is important to keep in mind that these objects depend on all three spatial coordinates.

Let us consider the case of a field distribution where the optical power is concentrated only on one waveguide, like in Figure 2.4. This field can be decomposed as follows:

$$E(z,t) = \frac{S(z,t) + A(z,t)}{\sqrt{2}}. \tag{2.5}$$

We now wish to understand how these modes propagate in the two waveguides. It is possible to show that:

$$\begin{aligned} S(z+\Delta z,t) &= e^{-i(\beta_S \Delta z)} S(z,t) \\ A(z+\Delta z,t) &= e^{-i(\beta_A \Delta z)} A(z,t), \end{aligned} \tag{2.6}$$

hence after a propagation of length Δz, the expression of $E(z,t)$ becomes

$$E(z,t) = e^{-i(\beta_S \Delta z)} \frac{S(z,t) + e^{-i(\Delta\beta \Delta z)} A(z,t)}{\sqrt{2}}. \tag{2.7}$$

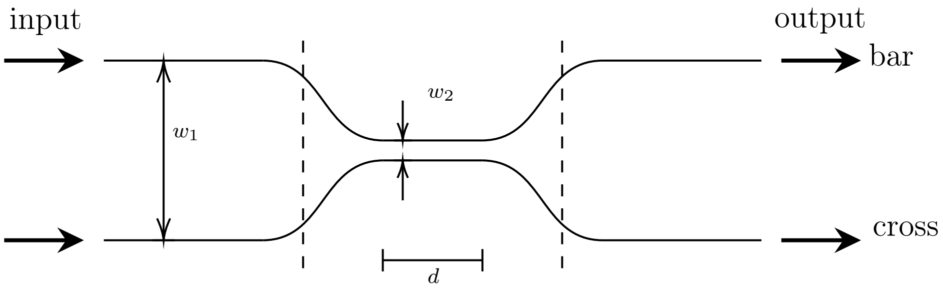

Figure 2.5: Schematic of a directional coupler. The waveguide distance is w_1 in the first and third section, and it becomes w_2 in the second section. The waveguides then interact for a total interaction distance d before parting ways in the third section once more.

Here $\Delta\beta = \beta_A - \beta_S$. This means that over z, the field's distribution oscillates with frequency $\Delta\beta$.
In particular, if $\Delta z = \pi/\Delta\beta$ then the field distribution after Δz is:

$$E(z + \Delta z, t) = e^{-i\frac{\pi\beta_S}{\Delta\beta}} \frac{S(z,t) - A(z,t)}{\sqrt{2}}. \tag{2.8}$$

Taking the square of the field amplitude reveals that the optical power behaves as if it "hopped" over from one guide to the other, with a spatial frequency equal to $\Delta\beta$.
The value of $\Delta\beta$ strongly decreases if the distance between the waveguides increases. If $\Delta\beta$ is low enough, then, the length necessary to obtain a hop can become quite big; for this reason, after a certain point it is easier to treat the waveguides as completely independent and non-interacting.

2.1.3. Directional Coupler

The *directional coupler* is a device made of two single-mode waveguides arranged in curvilinear paths as shown in Figure 2.5. Directional couplers are used to couple two waveguides together in such a way that some optical power is split among them. The device can be divided into three major sections: at the start, the waveguides are far apart and thus independent; in the middle, the waveguides interact through the phenomenon described in the previous section for a certain length d; finally, the waveguides separate and become independent again.
In between each section the waveguides are curvilinear unlike the straight waveguides we have discussed so far; this generally does have an impact on the polarisation of the light, however for the purposes of this thesis we do not consider the effect of polarisation. Since the waveguide is curvilinear, it does not have translational symmetry; this induces unavoidable losses. Moreover, as the waveguides come together, the $\Delta\beta$ parameter increases

and they are no longer independent; this means that the waveguides couple together well before the middle section. Here, however, we do not consider any coupling effect coming from the curved section and treat them as lossless.
We now wish to know the effect that the middle portion induces on the incoming states of light. We represent the state of the electromagnetic field over the basis $\{E_1(z), E_2(z)\}$, where $E_i(z)$ represents the fundamental mode of the i-th waveguide alone. This is a different basis with respect to the one used in the preceding section, but it is also valid. We consider $z = 0$ the beginning of the middle section for simplicity. Then:

$$E(0) = c_1 E_1(0) + c_2 E_2(0). \tag{2.9}$$

After the propagation by d, we know from Equation 2.7:

$$E_1(d) = e^{-i(\beta_S d)} \frac{S(0) + e^{-i(\Delta\beta d)} A(0)}{\sqrt{2}} \tag{2.10}$$

$$E_2(d) = e^{-i(\beta_S d)} \frac{S(0) - e^{-i(\Delta\beta d)} A(0)}{\sqrt{2}} \tag{2.11}$$

and $S(0), A(0)$ in turn are a linear combination of $E_1(0), E_2(0)$. In other words, we can relate $E_i(d)$ to $E_i(0)$ via a linear transformation:

$$\begin{bmatrix} E_1(d) \\ E_2(d) \end{bmatrix} = \frac{e^{-i(\beta_S d)}}{2} \begin{bmatrix} 1 + e^{-i(\Delta\beta d)} & 1 - e^{-i(\Delta\beta d)} \\ 1 - e^{-i(\Delta\beta d)} & 1 + e^{-i(\Delta\beta d)} \end{bmatrix} \begin{bmatrix} E_1(0) \\ E_2(0) \end{bmatrix}. \tag{2.12}$$

In the specific case of $c_1 = 1$, then, we obtain:

$$E(d) = e^{-i(\beta_S d + \frac{\Delta\beta d}{2})} \left(i \sin\left(\frac{\Delta\beta d}{2}\right) E_1(d) + \cos\left(\frac{\Delta\beta d}{2}\right) E_2(d) \right) \tag{2.13}$$

hence by taking the square of the amplitude of the field, we obtain the distribution of power over the two output waveguides

$$P_{\text{bar}} = P \sin^2\left(\frac{\Delta\beta d}{2}\right), \quad P_{\text{cross}} = P \cos^2\left(\frac{\Delta\beta d}{2}\right) \tag{2.14}$$

where *bar* and *cross* are used with reference to Figure 2.5. These quantities, when normalised over the input power P, will be referred to respectively as *reflection* $\mathcal{R}$ and *transmission* $\mathcal{T}$ of the directional coupler. These quantities represent the power splitting from a single waveguide - in this example, the first one - into the two output waveguides. In particular, *balanced* directional couplers have $d = \pi/2\Delta\beta$. In this case, the power from one input is evenly split between the two outputs; the matrix that relates the fields $E_i(d)$

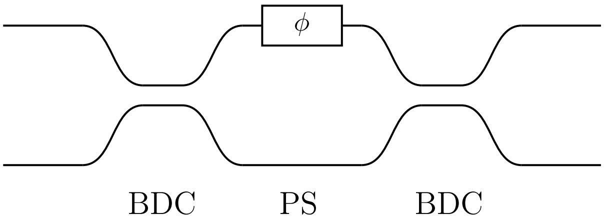

Figure 2.6: Schematic of a Mach-Zehnder interferometer, made with a phase shifter embedded within two balanced directional couplers. The device can be reconfigured if the phase ϕ can be controlled.

and $E_i(0)$ takes the form:

$$M_{\mathrm{BS}} = e^{-i\left(\frac{\pi\beta_S}{\Delta\beta}+\frac{\pi}{4}\right)}\frac{1}{\sqrt{2}}\begin{bmatrix}1 & i\\ i & 1\end{bmatrix}. \tag{2.15}$$

The phase $\pi\beta_S/\Delta\beta + \pi/4$ is global and can therefore be neglected for the purposes of understanding the operation of this device. What matters is that the reflection and transmission in this condition become equal to 1/2.

2.2. Universal Photonic Processors

2.2.1. Reconfigurable Mach-Zehnder Interferometer

Figure 2.6 shows a *Mach-Zehnder Interferometer* (MZI). The device comprises a balanced directional coupler, followed by a phase shifter and another directional coupler. The phase shifter is a device that induces an additional phase shift on the state of light only on one waveguide.

By assuming that the phase shift θ introduced by the shifter can be represented as a matrix on the $\{E_1(z), E_2(z)\}$ basis as:

$$\begin{bmatrix}e^{i\theta} & 0\\ 0 & 1\end{bmatrix}. \tag{2.16}$$

The overall matrix that corresponds to the MZI can be calculated as a product of the matrices of the components:

$$\begin{aligned} M(\theta) &= \frac{1}{2}\begin{bmatrix} 1 & i \\ i & 1 \end{bmatrix}\begin{bmatrix} e^{i\theta} & 0 \\ 0 & 1 \end{bmatrix}\begin{bmatrix} 1 & i \\ i & 1 \end{bmatrix} \\ &= e^{i\left(\frac{\theta}{2}+\frac{\pi}{2}\right)}\begin{bmatrix} \sin\left(\frac{\theta}{2}\right) & \cos\left(\frac{\theta}{2}\right) \\ \cos\left(\frac{\theta}{2}\right) & -\sin\left(\frac{\theta}{2}\right) \end{bmatrix}. \end{aligned} \tag{2.17}$$

It is noted that this device couples two waveguides, much like the directional coupler, however the reflection and transmission parameters now depend on the phase shift ϕ and not on the distance d. This offers many advantages, primarily the ability to reconfigure the device as the length d is generally non-actionable while the phase shift ϕ is much more easily manipulated. In the following chapter the main methods of controlling the shift ϕ will be presented, though virtually all of them achieve it by locally controlling the refractive index of the waveguide; this changes the propagation parameter β.

The reconfigurability of these devices make them perfect candidates for the implementation of more complex circuits and in particular for the realisation of UPPs.

We now consider an extension of this design that employs a second phase shifter placed before the first directional coupler. In this case the matrix that represents the whole device is:

$$M(\theta,\varphi) = e^{i\left(\frac{\theta}{2}+\frac{\pi}{2}\right)}\begin{bmatrix} e^{i\varphi}\sin\left(\frac{\theta}{2}\right) & \cos\left(\frac{\theta}{2}\right) \\ e^{i\varphi}\cos\left(\frac{\theta}{2}\right) & -\sin\left(\frac{\theta}{2}\right) \end{bmatrix} \tag{2.18}$$

where now we are allowed to control independently the two phase shifts θ and φ. This device is the elementary building block of UPPs.

Up to a pair of extra phases at the output of the device, this reconfigurable MZI can implement any arbitrary 2-by-2 unitary matrix. In other words, given a unitary 2-by-2 matrix U, there is a unitary diagonal matrix D and a pair of phase shifts (θ, ϕ) such that

$$M(\theta,\phi)D = U, \tag{2.19}$$

therefore a reconfigurable MZI of this kind is the smallest example of an Universal Photonic Processor.

2.2.2. Universal Photonic Processors

A *Universal Photonic Processor* (UPP) is a device capable of implementing an arbitrary unitary transformation between the states of light from input to output. In other words, if we describe the state of the light arriving at the N ports of the UPP as a vector, the

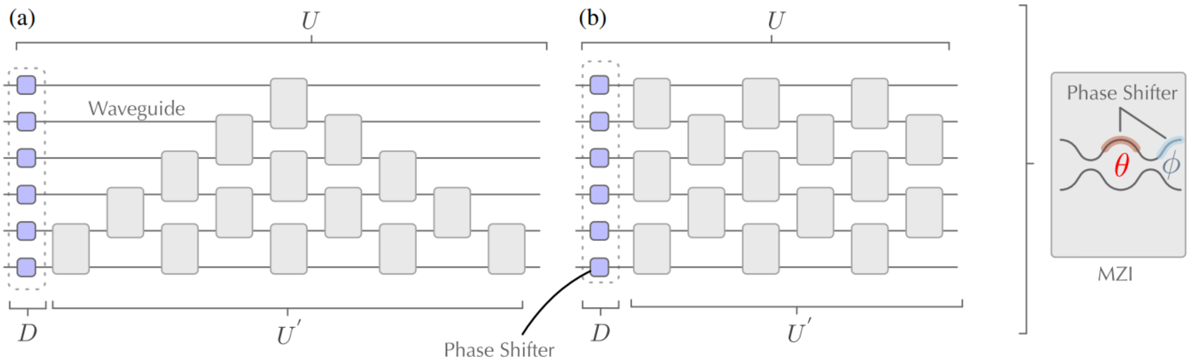

Figure 2.7: Configurations for the implementation of a UPP using reconfigurable MZIs. (*a*) The topology proposed by Reck et al. [3]. (*b*) The topology proposed by Clements [4]. On the right, a schematic representation of the MZI that constitutes the elementary cell. Figures adapted from [5].

UPP implements the multiplication of this vector by an element of the unitary group $U(N)$.

Reck and his group [3] have proven in 1994 that a UPP may be constructed from a mesh of reconfigurable MZIs with a triangular topology; later, in 2016, Clements et al. [4] has proven the same with a more compact and symmetric topology. The two configurations are shown in Figure 2.7. The two topologies both employ the same number of reconfigurable MZIs, equal to $N(N-1)/2$, where each elementary cell is described by the matrix 2.18.

Reck's configuration is quite simple, however it has a major drawback: not all the optical paths have the same length, some going through as many as $2N-3$ cells while a different optical path only goes through 1 cell. Therefore, some optical paths are exposed to the fabrication tolerance of the MZIs more than others; this can lead to inconsistent effects on the optical signal, as well as add significant delays for applications that employ localised packets such as single photons.

In Clements' symmetric configuration, instead, all paths always go through N cells with very few exceptions that can go as low as $N/2$ cells; moreover, this configuration is also optimal in the sense that the overall length of the device is the smallest possible. This not only evenly distributes the exposure to fabrication tolerances, but also decreases the amount of resources needed for the fabrication.

2.2.3. UPP Programming and Control

The operation of a single UPP in general requires tuning $O(N^2)$ phases. This is a nontrivial problem, as between the implementation of a quantum algorithm (i.e. a unitary matrix or sequence thereof) and the actual physical control of the individual phase shifters on the device there are many steps, which are influenced by the specific material platform at hand.

A number of programming protocols have been devised to solve such a problem, which may be summarised in three classes: *element-by-element* methods, where the phase shifters are controlled and considered individually by choosing the phases θ, ϕ directly; *compiled*, where a decomposition algorithm is used to break the unitary matrix down into singular contributions of each MZI in the network, and from there the phase shifts are chosen accordingly [3, 4]; *optimized*, where the unitary matrix is implemented through an optimization algorithm on feedback [6].

Each protocol has its own use. In particular, if the UPP implements a switching matrix then element-by-element methods are advantageous for their simplicity; if the aim is to implement a general unitary matrix instead, compiled methods should instead be used [7]; for implementations where the UPP is used to scramble light or obtain a specific intensity distribution at the output, optimized methods are the best toolbox [8].

In all of these methods, one needs a way to determine how accurate the implementation of the unitary has been. Given a UPP implementing a unitary N-by-N matrix $\mathbf{U}$, there exist methods to completely calibrate both the amplitude and phase of any given entry of the matrix [9]; the matrix measured in this way can be confronted with a target unitary matrix by means of the *fidelity* parameter:

$$\mathcal{F}(\mathbf{U}, \mathbf{U}_T) = \frac{1}{N} \operatorname{Tr}\left\{ \left| \mathbf{U}^\dagger \mathbf{U}_T \right| \right\}. \tag{2.20}$$

Here the absolute value brackets around a matrix imply we take the absolute values of each entry. This is effectively a measure of closeness between the matrices, yielding 1 if $\mathbf{U} = \mathbf{U}_T$ and less than 1 otherwise. State of art values for this parameter for photonic integrated applications are in the range $[0.95, 1]$ [10]. If the measurement of phase for each entry is not available, it is still possible to define an alternative fidelity parameter as follows:

$$\bar{\mathcal{F}}(\mathbf{U}, \mathbf{U}_T) = \frac{1}{N} \operatorname{Tr}\left\{ |\mathbf{U}^\dagger| |\mathbf{U}_T| \right\}. \tag{2.21}$$

This parameter is insensitive to difference in phases between the implemented and target matrices, but it offers a similar understanding of the closeness between the target and the implementation. As a matter of fact, $\bar{\mathcal{F}} = 1$ means that the entries of the two matrices have the exact same square modulus, hence the distribution of power at the output of the device will match the target.

2.2.4. Clements' Decomposition Algorithm

This work focuses on the calibration and operation of UPPs featuring the Clements topology [4]. In the article, Clements also showcases an algorithm to correctly operate the device with this particular topology: in short, given a unitary matrix Clements' algorithm retrieves all the phases (θ, ϕ) that each reconfigurable MZI in the network must have in order to implement such a matrix.

We now give some details of how this algorithm works. We start by assuming that each reconfigurable MZI in the network acts on the incoming state using the matrix

$$A(\theta, \phi) = \begin{bmatrix} e^{i\phi}\cos\theta & -\sin\theta \\ e^{i\phi}\sin\theta & \cos\theta \end{bmatrix} \tag{2.22}$$

where the role of θ, ϕ is analogous to the internal and external phases of our circuit. We also take the following matrix as our "elementary component":

$$T_{mn}(\theta, \phi) = \begin{bmatrix} 1 & 0 & & & & & & & \\ 0 & 1 & & & & & & & \\ & & \ddots & & & & & & \\ & & & e^{i\phi}\cos\theta & \dots & -\sin\theta & & & \\ & & & \vdots & \ddots & \vdots & & & \\ & & & e^{i\phi}\sin\theta & \dots & \cos\theta & & & \\ & & & & & & \ddots & & \\ & & & & & & & 1 & 0 \\ & & & & & & & 0 & 1 \end{bmatrix}. \tag{2.23}$$

More in detail, $T_{mn}(\theta, \phi)$ is the matrix obtained by embedding matrix $A(\theta, \phi)$ into the identity matrix in such a way that $(T_{mn})_{mm} = A_{11}, (T_{mn})_{mn} = A_{12}, (T_{mn})_{nm} = A_{21}, (T_{mn})_{nn} = A_{22}$. In what follows, we drop the dependence on θ, ϕ for the sake of notational simplicity. It can be shown [3] that these matrices have the property to null specific elements of a unitary matrix U in the following sense: given a pair of integers a, b, there is a T_{mn} such that the ab element of UT_{mn} is zero.

Clements shows that if U is an N-by-N unitary matrix, then there is an N-by-N diagonal matrix D such that

$$U = D\left(\prod_{mn \in S} T_{mn}\right). \tag{2.24}$$

D contains only phase terms on the diagonal (i.e. every entry is of the form $e^{i\varphi}$ for some ϕ); S is a sequence of pairs of integers containing exactly $N(N-1)/2$ terms. With reference to Clements' configuration of an UPP (Figure 2.7b), each term corresponds to an MZI in the network. In other words, Clements' algorithm decomposes a unitary matrix into the contributions due to each MZI in the network, assuming this network uses Clements' configuration.

In practice for the purposes of the operation of such a device, Clements' algorithm takes as an input a unitary matrix and returns $N(N-1)/2$ pairs (θ_i, ϕ_i) that correspond to the phase shifts each MZI needs to apply in order to obtain at the output a specific unitary matrix - up to an extra set of phases at the very output of the device, represented by the diagonal matrix D. For the purposes of this work, these extra phases will not be measured and do not have any influence on the operation of the device as described in the preceding chapter.

More in detail, each T_{mn} is found by nulling entries sequentially in the unitary matrix U. We show here the process for a 6-mode UPP as well; the steps are essentially the same, the only real difference is in the amount of steps required to fully determine all the phases. The elements of U are nulled by multiplying either U from the right by T_{mn}^{-1} for some mn, or by multiplying from the left by T_{mn} for some mn. The matrices physically correspond to MZIs in the network; the pattern for a 5-mode UPP is shown in Figure 2.8.

We now describe the steps of the algorithm in pseudo-code.

Algorithm 2.1 **Clements' Decomposition Algorithm**

```
for $i$ from 1 to $N-1$ do
    if $i$ is odd then
        for $j$ from 0 to $i-1$ do
            find $T_{i-j,i-j+1}$ such that the $(N-j, i-j)$ entry of $UT_{i-j,i-j+1}^{-1}$ is zero
            $U \leftarrow UT_{i-j,i-j+1}^{-1}$
        end for
    else
        for $j$ from 1 to $i$ do
            find $T_{N+j-i-1,N+j-i}$ such that the $(N+j-i, j)$ entry of $T_{N+j-i-1,N+j-i}U$ is zero
            $U \leftarrow T_{N+j-i-1,N+j-i}U$
        end for
    end if
end for
```

After the procedure is completed we have sequentially nulled every off-diagonal element of U. Then, tracing back through the update steps, we obtain the following equation:

$$\left(\prod_{mn\in S'} T_{mn}\right) U \left(\prod_{mn\in S''} T_{mn}^{-1}\right) = J. \tag{2.25}$$

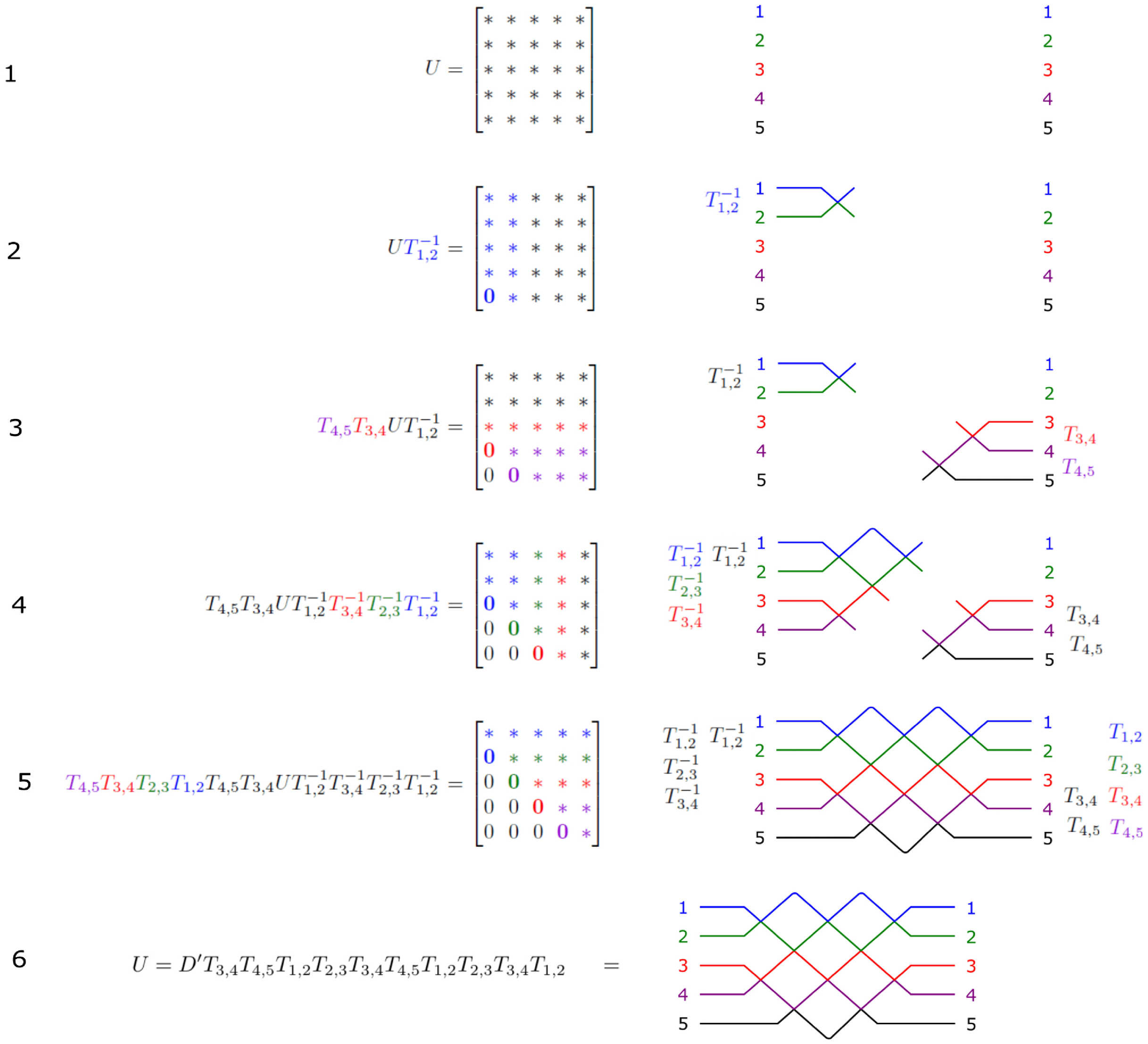
1
$U =$
2
$UT_{1,2}^{-1} =$
3
$T_{4,5}T_{3,4}UT_{1,2}^{-1} =$
4
$T_{4,5}T_{3,4}UT_{1,2}^{-1}T_{3,4}^{-1}T_{2,3}^{-1}T_{1,2}^{-1} =$
5
$T_{4,5}T_{3,4}T_{2,3}T_{1,2}T_{4,5}T_{3,4}UT_{1,2}^{-1}T_{3,4}^{-1}T_{2,3}^{-1}T_{1,2}^{-1} =$
6
$U = D'T_{3,4}T_{4,5}T_{1,2}T_{2,3}T_{3,4}T_{4,5}T_{1,2}T_{2,3}T_{3,4}T_{1,2} =$
$T_{1,2}^{-1}$
$T_{2,3}^{-1}$
$T_{3,4}^{-1}$
$T_{1,2}$
$T_{2,3}$
$T_{3,4}$
$T_{4,5}$
1
2
3
4
5

Figure 2.8: Clements' algorithm for a 5-mode UPP. Each step determines T_{mn} for a certain m and n by nulling some entry of U. Figure from [4].

Here S' and S'' are sequences of integer pairs and J is a diagonal matrix. Notice that for every diagonal matrix J there is a diagonal matrix J' such that

$$T_{mn}^{-1} J = J' T_{mn}.$$

Therefore, all terms of the products can be rearranged to obtain Equation 2.24, where D for that equation will in general be a diagonal matrix different from J [4].
From here one can extract (θ_i, ϕ_i) from each T matrix to determine which phase shifts must be applied to the circuit in order to implement the matrix U up to the extra phases at the output represented by D.

2.2.5. Applications of UPPs

The realisation of UPPs paves the way for the setup of new classical and quantum experiments [11, 12], and they allow breakthroughs in quantum simulation [13], quantum machine learning [14], and optical networking [15]. There is also a number of applications for what concerns the use of UPPs with classical light beams, and we now offer a quick rundown.

Annoni and collaborators in 2017 [8] have devised a protocol of the optimised kind to operate a UPP as a mode unscrambler. In mathematical terms, the circuit can be reconfigured into turning any set of N orthogonal vectors in $\mathbb{C}^N$ into the standard set of orthogonal basis vectors of $\mathbb{C}^N$. Remarkably, this is done in a totally automatic way by employing a self-configuring real-time algorithm which optimises the phases in order to implement the correct unitary transformation; this dynamical aspect was shown by introducing a time-varying perturbation of the mode mixing.
This can also be done in the opposite way, turning the device into a mode scrambler instead. This has many applications in integrated optics, especially to enable precise spatial multiplexing and de-multiplexing; it may be applied to every situation where mode superposition may happen in the transfer of optical information, may it be due to waveguide-bending in an optical fiber or simple loss due to fabrication defects.

Photons are attractive as carriers of quantum information, so it is natural that UPPs can provide the means to achieve the fine control of the unitary transformations needed for many quantum information applications. In particular, their reconfigurability offers rapid prototyping for quantum algorithms which is a great step forward with respect to static circuits.
Quantum computing protocols generally adopt two possible models: the *circuit model* [16], in which single-qubit and many-qubit gate operations are performed sequentially on

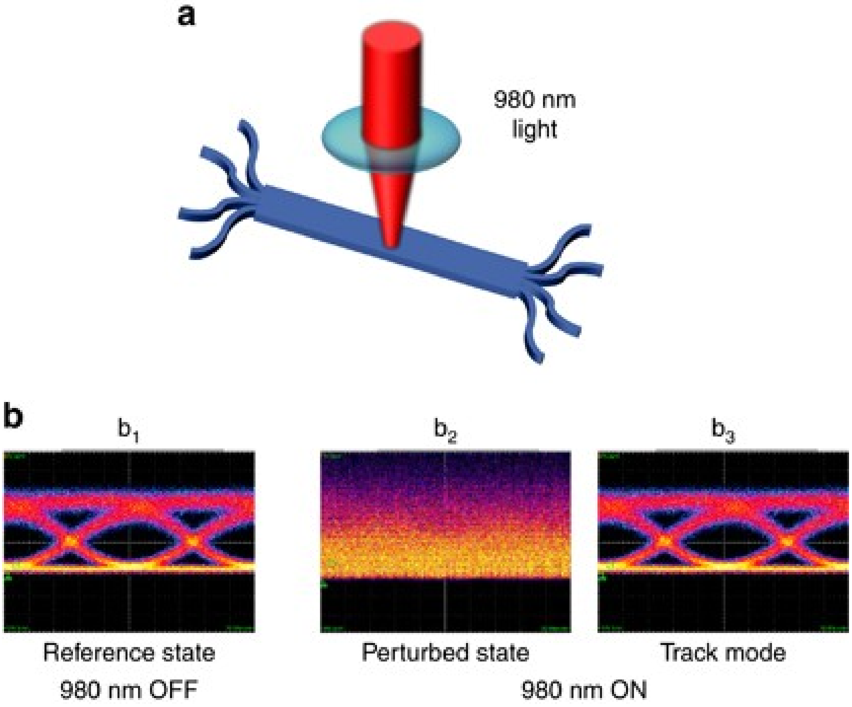

Figure 2.9: Reconstruction of modes scrambled by time-varying mixing. a) Shows the 980nm laser configuration and the four modes; b1) shows the reference state used to initially configure the mode unscrambler with the laser turned off; b2) and b3) show the same measurement performed as soon as the perturbing laser source was turned on and after the application of the self-configuring algorithm respectively. Figure taken from [8].

the quantum states; the *cluster model* [17], in which the state is first prepared into a highly entangled (cluster) state and then operations are performed on this new state.
The real problem of photons from the point of view of quantum algorithms is the difficulty in creating two-qubit gates. In linear optical quantum circuits, in fact, this is done probabilistically and the success of the two-qubit operation is announced by a heralding mechanism - typically, a heralding photon. In this context, Carolan et al. [11] have shown heralded two-qubit operations implemented on a six-mode UPP, where the detection of the heralding photons signal that the two-qubit operation has been performed successfully.

Artificial Neural Networks (ANN) have improved the efficacy of object detection and language processing [18] While the technology to provide this software with faster access to data has improved, the classical structure of transistors and memories still poses a limitation to computational speed. As Optical Neural Networks (ONN) have been proposed in the past [19], UPPs offer a solid platform on which to implement the linear transformations required by these ONNs while mantaining the necessary level of phase stability and programmability. Especially if paired with nonlinear optical components, UPPs can pave the way for artificial neural networks fully in the optical domain with high efficiency and low power cost. In particular, Shen and Harris et al. [7] have shown that an ANN can be achieved using a sequence of UPPs with a stage of nonlinear "optical activation functions" between them; these activation functions could be achieved using saturable absorbers [20]. This effectively reproduces the structure of a deep learning algorithm fully within the optical domain.

3 | Fabrication Platforms for Integrated Photonics

In this chapter we showcase the major material platforms on which UPPs have been demonstrated. The structure of the chapter is divided into two major groups: material platforms where UPPs have been obtained through planar fabrication methods (Section 3.1), and platforms where UPPs have been obtained through direct laser writing methods (Section 3.2). Within each section we offer a rundown of the materials with their characteristics, strengths and limitations, as well as state of the art for reconfigurable photonic devices with focus on UPPs.

3.1. Planar Fabrication Processes

By *planar fabrication processes* we mean the collection of techniques for the fabrication of two-dimensional structures. These processes exploit additive processes, such as layering of materials, as well as subtractive ones, such as lift-off and chemical etching, to produce a structured design. The most important technique, called *photolithography*, employs light to create a mask on the substrate surface to allow selective deposition and etching of materials. The image of the mask is projected onto a light-sensitive chemical (the *photoresist*) which impresses the design on the substrate; this mask will then be used to selectively act on the materials in further steps.

In this chapter we list some of the major material platforms, their major design strengths and drawbacks, with a focus on advancements in the design and operation of UPPs.

3.1.1. Silicon on Insulator

Silicon on Insulator (SOI) is a fabrication platform for integrated photonics based on silicon waveguides surrounded by silica; it is possible to produce devices exploiting the same lithographic processes already in use for other silicon-based technologies such as CMOS, allowing for the mass-production of integrated opto-electronic circuits. Nowadays

it is becoming a widespread technology for integrated photonics, especially for nonlinear optics, and more recently, lidar, mid-infrared sensors and quantum photonics circuits.
Because of the high refractive index difference between guiding medium and substrate, with respect to other technologies, the same level of bending losses can be achieved with a much smaller bending radius. This effectively allows for the fabrication of much more compact devices, in particular for SOI the bending radius of the waveguides can go as low as 1 μm [21]. Therefore, the platform offers very high integration density and can achieve a high degree of compactness and unprecedented levels of light confinement. Moreover, the choice of silicon as the guiding medium gives the technology access to a wide spectral window in the communication range as well as nonlinear optical effects, in particular in the range where both silicon and silicon dioxide are transparent (1.1–3.8 μm) [22].

SOI offers great advantages with respect to other platforms, first of which is the easy integration with the widely available CMOS foundries developed for the microelectronics industry; this greatly decreases production costs and makes the technology affordable for the purposes of mass-production of integrated photonic devices.
With the great advantage of compactness also comes a disadvantage: SOI integrated photonic circuits suffer heavily from fabrication tolerances. Even though the photolitographic techniques for the fabrication of SOI devices are improving light scattering at the sidewalls still represents the dominant cause of optical loss of waveguides in the SOI platform [23]. Despite this, SOI has been among the leading platforms for passive devices, sporting a wide selection of integrated components ranging from ring resonators, to filters, to switches, to interferometers [22].
For what concerns the stability of these passive devices, SOI shows a high thermo-optic coefficient. Because of this, SOI integrated components are highly susceptible to temperature variations. Work has been done on this front to obtain temperature-independent operation of the circuits [24].
Another drawback of this technology comes in the form of poor efficiency in fiber-to-chip coupling, as the waveguides produced with SOI are quite small: the spot size produced by a standard telecommunications fiber is approximately 630 times larger than the waveguide core. This complicates the assembling stage as the tolerance to fiber positioning becomes much lower. This is a problem from the point of view of the packaging of SOI devices; in recent years there has been a push for the mass-marketing of integrated photonics and therefore the ability to assemble SOI circuits together with standard communications equipment (such as fibers) has been a relevant issue.

Reconfigurability on this platform has been achieved both through thermo-optic effect [25] exploiting the high thermo-optic coefficient of silicon, but also through the plasma dispersion effect [26], which is the most widely used modulation technique for silicon-based technologies. As the name suggests, this approach involves modifying the density of free carriers present in the material through which the light propagates, causing a modulation of the refractive index as well as the absorption coefficient; this modification can be induced optically with an external laser source (*light-by-light* modulation [27]) or electrically by employing suitable semiconductor structures that manipulate the densities of electrons and holes in the material. The greatest engineering challenge in this direction has been to raise the modulation speed of the devices for applications in information processing and telecommunications [28]. A disadvantage with plasma dispersion phaseshifting is that the absorption depends on the amount of phase shift: changing θ not only applies a phase shift but it also increases absorption due to the higher population of free electrons in the conduction band. Thermo-optic effect phaseshifting, while bound to lower-speed applications, does not show phase-dependent absorption effects.

In the literature we find the state of the art for reconfigurable integrated optical circuits made with SOI technology. Harris and collaborators in 2017 [29] presented a 26-mode photonic device with a unique topology; 176 phase shifters were used to control this circuit. In terms of losses, each connection between the device and the optical fibers used to transport the light signal introduced 3.5 dB; this happened both at input and output. The total loss across the chip, connection losses included, was 8 dB. This is due to the aforementioned mismatch between the SOI and optical fiber technologies as well as the propagation losses of SOI itself.

This device has been primarily used to explore and study quantum random walks, the coherent analogue of random walks, and quantum transport simulations. The processor was fabricated in a CMOS-compatible silicon photonics SOI process and sported the highest beam splitter visibility recorded in literature at the time. The processor accepted only transverse-electric polarized light, requiring a bank of polarization rotators to couple to the chip modes (shown in Figure 3.1e on the left). Polarization rotator fibers have been connected to the photonic integrated circuit. The output of the UPP was then sent to an array of detectors and read out using a microcontroller.

It is difficult to gauge the performance of this device in terms of the aforementioned fidelity parameter as the device has not been used in the context of implementing a specific unitary matrix. Nevertheless, this device represents the state of the art in the fabrication and control of a complex mesh of MZIs in the SOI platform.

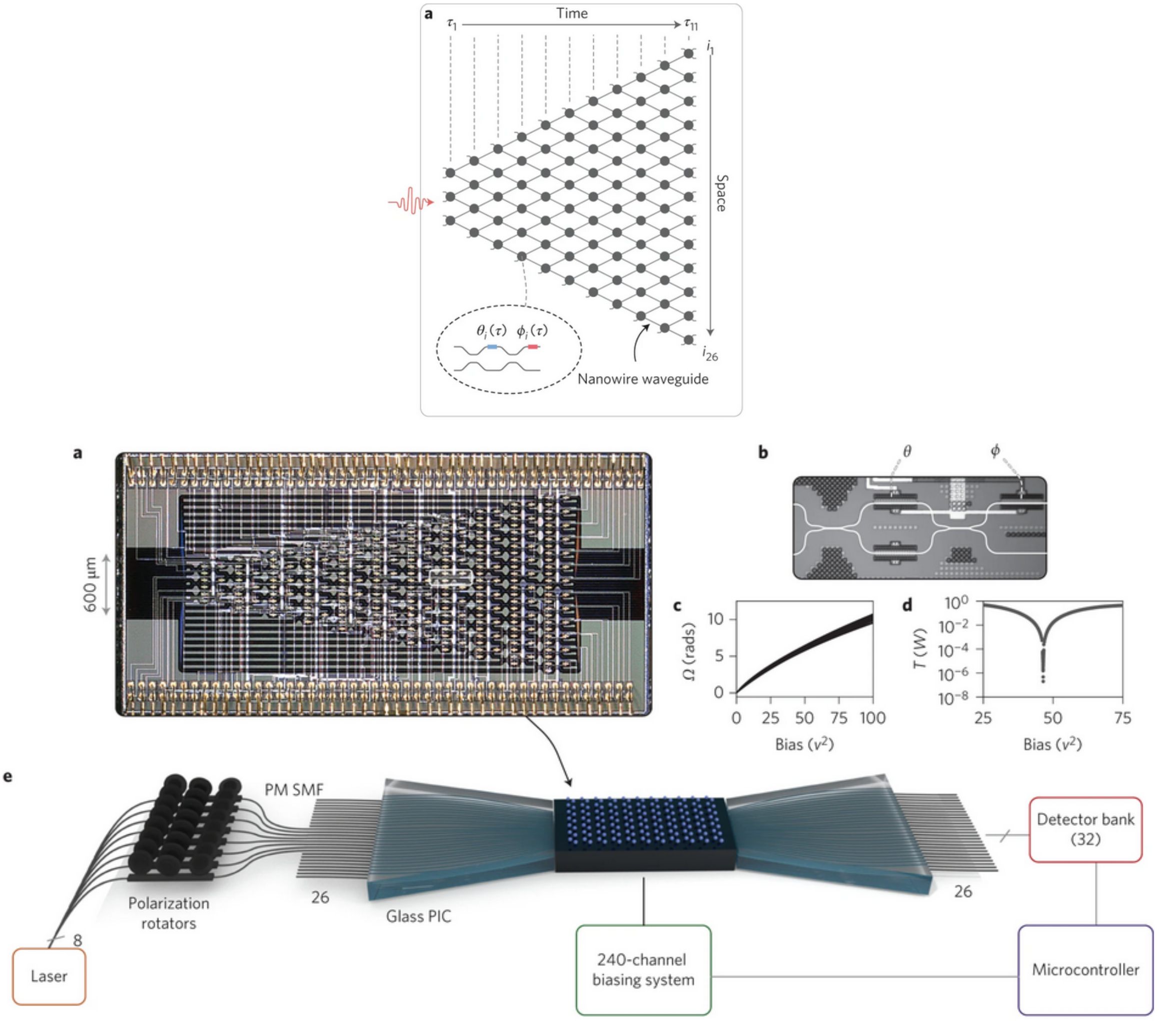
a
Time
τ_1
τ_{11}
i_1
Space
i_{26}
$\theta_i(\tau)$ $\phi_i(\tau)$
Nanowire waveguide
a
600 μm
b
θ
ϕ
c
Ω (rads)
10
5
0
0 25 50 75 100
Bias (v^2)
d
T (W)
10^0
10^{-2}
10^{-4}
10^{-6}
10^{-8}
25 50 75
Bias (v^2)
e
PM SMF
Polarization rotators
26
8
Laser
Glass PIC
26
Detector bank (32)
240-channel biasing system
Microcontroller

Figure 3.1: The scheme and physical realisation of the 26-mode UPP. Above, the schematic for the circuit. Below, the actual realisation; a) The whole chip seen from the top. b) Detail of the white inset of a). c) Phase versus voltage curve for all internal and external phase shifters on the chip. d) Transmission spectrum for an MZI with careful input polarization filtering. e) Setup of the experiment. Figures adapted from [29].

3.1.2. Silica on Silicon

Silica on Silicon (SOS) is one of the primary platforms for optical integrated circuits, being widely common still today and on which a quantum photonic circuit was first demonstrated [30].

SOS devices consist of a silicon wafer over which a layer of doped silica glass is deposited; subsequently, the glass is photolithographically exposed and etched to leave behind free-standing patterned waveguide structures corresponding to the final device. Finally, another silica glass layer is applied, encapsulating the patterned waveguide fully within the glass. The main material of the platform is therefore doped silica; Al_2O_3, N_2, GeO_2, As_2O_3, ZrO_2, P_2OS or TiO_2 can be used as dopants to raise the refractive index, while F or B_2O_3 can be used to lower it [31].

Like other photolithography-based platforms, SOS is compatible with CMOS technology both in the fabrication aspect and even in the integration with microelectronic devices [32] which implies very low production costs as one can leverage the already widely available CMOS techniques to produce SOS integrated components. However, the most striking advantage of SOS technology is the compatibility with the vastly available optical fiber technologies, as the silica core surrounded by silica cladding is analogous to the standard technology of optical fibers; in fact, the choice of materials make SOS transparent at spectral ranges that include the state of the art in fiber optics fabrication, single-photon generation and detection [33]. This offers great advantage in terms of low-cost packaging and mass-production, where different photonic chips can be easily connected together using optical fibers with small losses. To this end, alignment between optical fibers and input ports on the chip has been achieved using V-grooves directly built on the chip itself [34].

Due to the silica-within-silica structure of SOS devices, it follows that the refractive index change between core and cladding is low. This means that to keep the bending losses low, large bending radii (25 mm) are needed; this poses a limit to how compact SOS devices can be. On the flip side, they sport very low propagation losses (less than 0.1 dB/m), which makes SOS a suitable choice for passive integrated photonic circuits also for quantum applications.

Since it is amorphous, silica does not show electro-optic behaviour for the purposes of reconfigurability; it is also an insulator, which makes it impossible to achieve reconfigurability using plasma dispersion. Because of this, reconfigurability on this platform is generally only achieved through thermo-optical effects. In this regard, SOS has shown high stability in thermo-optical modulators [35] which makes this technology suitable for

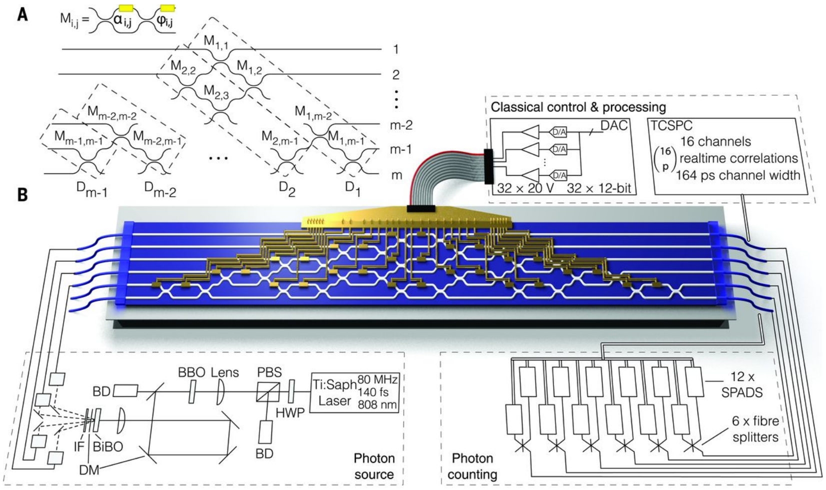
A
$M_{i,j}$ =
$\alpha_{i,j}$
$\varphi_{i,j}$
$M_{1,1}$
$M_{2,2}$
$M_{1,2}$
$M_{2,3}$
$M_{m-2,m-2}$
$M_{m-1,m-1}$
$M_{m-2,m-1}$
$M_{1,m-2}$
$M_{2,m-1}$
$M_{1,m-1}$
1
2
m-2
m-1
m
...
D_{m-1}
D_{m-2}
D_2
D_1
B
Classical control & processing
DAC
D/A
32 × 20 V
32 × 12-bit
TCSPC
16 channels
$\binom{16}{p}$ realtime correlations
164 ps channel width
BD
BBO
Lens
PBS
Ti:Saph Laser
80 MHz
140 fs
808 nm
HWP
IF
BiBO
DM
BD
Photon source
12 x SPADS
6 x fibre splitters
Photon counting

Figure 3.2: The UPP presented by Carolan. a) Decomposition of a fully parametrized unitary for an m-mode circuit to realize any LO operation. Subunitaries D_i consist of MZIs $M_{i,j}$ built from phase shifters (yellow) and beam splitters, to control photon amplitudes ($\alpha_{i,j}$) and phases ($\varphi_{i,j}$). b) Multiphoton ensembles are generated with a dedicated setup. Photons are collected into polarization-maintaining fibers and delivered to the UPP via a packaged V-groove fiber array. The processor is constructed over six modes as a cascade of 15 MZIs, controlled with 30 thermo-optic phase shifters, and actively cooled with a Peltier cooling unit. Photons are then out-coupled into a second packaged array and counted by using a 12-channel Time-Correlated Single-Photon Counting (TCSPC) module.

the creation of UPPs with thermically reconfigured MZIs. The main problem with this thermo-optical reconfigurability is the lack of high-speed modulation, as well as posing a limit to the integration density due to thermal cross-talks.

Carolan and his collaborators in 2015 [11] have demonstrated a 6-mode UPP built using SOS technology with a Reck topology. They showcased its performance across experiments of boson sampling as well as photon indistinguishability with remarkable results; the device comprises 15 MZIs built with SOS and reconfigured using 30 thermo-optic phase shifters, each controlled electronically.

Boson sampling is a mathematical proof (using plausible conjectures) that a many-photon state, when acted on by a large UPP circuit set to implement a Haar-random unitary, will give rise to a probability distribution that cannot be efficiently sampled by a classical algorithm. The classical intractability arises because the probability amplitude for each correlated photon detection event is given by a classically hard function, known as the "permanent", of the submatrix that describes a particular route of photons through the circuit. Experimentally, each detection event represents a sample drawn from that classically forbidden probability distribution.

The device was programmed to implement 100 different boson sampling routines on 3 photons, exploring most of the available space of configurations of the chip, obtaining an average fidelity of 0.95.

3.1.3. Silicon Nitride

Another platform for Integrated Photonics comes in the form of *Silicon Nitride* (SiN). The material structure of SiN comprises a silicon nitride waveguide (Si_3N_4), around which is deposited silicon dioxide (SiO_2) as cladding. These processes are, like other photolithographic platforms, fully compatible with CMOS and wafer-scale foundry techniques.

This material is particularly attractive for the purposes of quantum optics applications given its large transparency spectrum, ranging from 440 nm to 2500 nm. This means that the platform can also be used with the most common quantum dot technologies for single-photon sources. Early motivation to investigate $Si_3\,N_4$ photonic circuits was a platform that resided on a silicon substrate, utilized compatible silicon processing technologies, and addressed applications at wavelengths where silicon is absorbing; nowadays, the technology is used to compliment the capabilities of other platforms such as SOI and SOS. In recent years there has been a strong push towards ultra-low-loss SiN waveguides, and state-of-the-art straight waveguides can reach losses as low as 0.3 dB/m even though they trade these low losses with high bending radii [36].
In general, the waveguide loss and minimum bend radius are design tradeoffs based on desired performance and vary for each integration platform. SiN comes in as a middle ground between the small bend radius of SOI and the low waveguide loss of SOS, with the possibility to design the shape and size of the guiding structures if the performance goal is closer to either of the two extremes. In particular, the technology uses core thickness, waveguide width, and waveguide bend radius as design space; several different waveguide designs are also available, making SiN a flexible platform.
By virtue of this flexibility, SiN also offers excellent compatibility with other fabrication platforms, especially SOI, as well as allowing hybrid integration of Si_3N_4 and other materials such as $LiNbO_3$ [37].

Differently from silicon-based waveguides like SOI, Si_3N_4 does not allow reconfigurability through plasma dispersion effect. In order to achieve a reconfigurable device, then, one can exploit the thermo-optic properties of Si_3N_4 [38]; in recent years work has been done towards the integration of $LiNbO_3$ and Si_3N_4 in the SiN platform to achieve high-speed electro-optic modulators [39].

The state of the art in SiN for universal photonic processors has been presented by Ta-

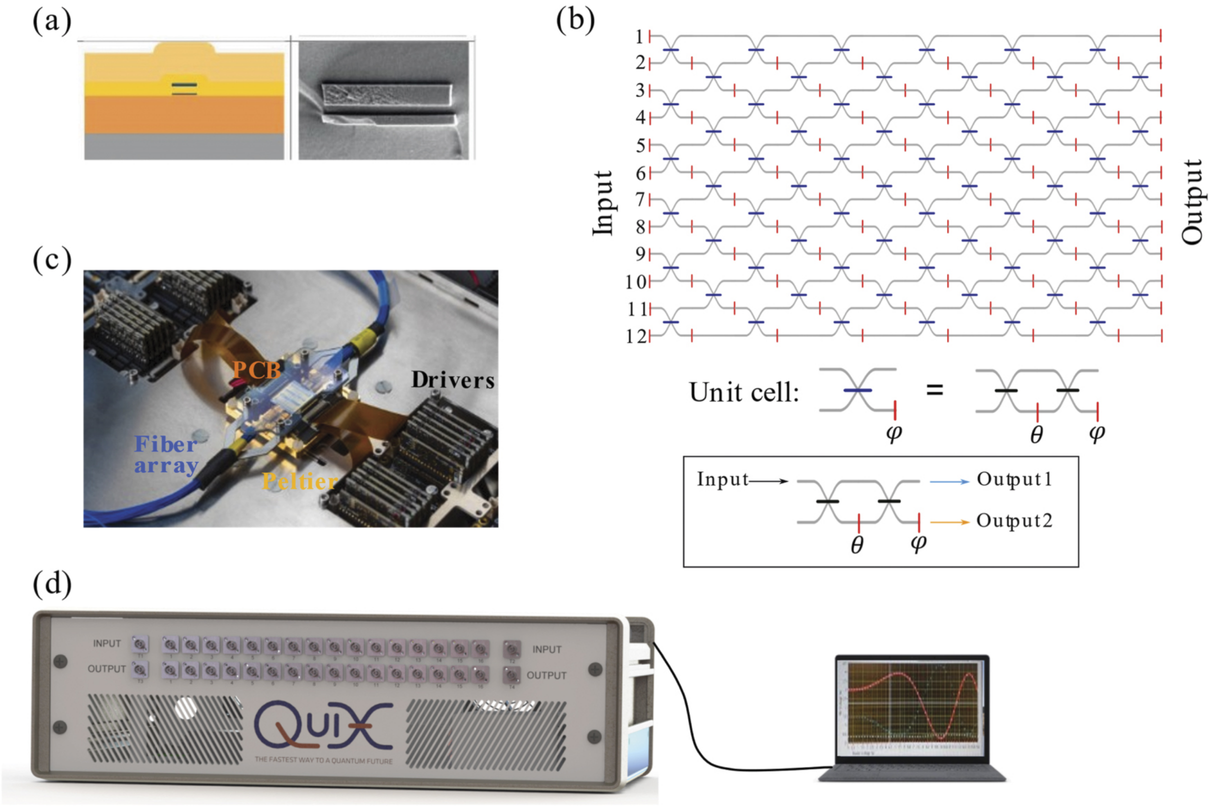
(a)
(b)
1
2
3
4
5
6
7
8
9
10
11
12
Input
Output
Unit cell:
=
φ
θ
φ
Input
Output1
Output2
θ
φ
(c)
PCB
Drivers
Fiber array
Peltier
(d)
INPUT
OUTPUT
INPUT
OUTPUT
QuiX
THE FASTEST WAY TO A QUANTUM FUTURE

Figure 3.3: Overview of the QuiX photonic processor. a) Schematic and SEM picture of the cross-section used for the waveguides. b) Functional design of the 12-modes photonic processor. The blue line represents a TBS that is implemented as an MZI with two 50:50 directional couplers (black lines) and a thermo-optic PS in red. c) Picture of the photonic assembly of the 12-modes processor as mounted inside the control box. d) Schematic for the QuiX control system. Figure from [10].

ballione and collaborators in 2021 [10]. This is a 12-mode UPP fabricated with TripleX technology [40]: the platform achieves propagation losses of 0.1 dB/cm with a bend radius of 100 μm; the chip is designed to work with laser sources at 1550 nm. An overview of the presented device is shown in Figure 3.3.

The reconfiguration of the device is achieved, of course, through thermo-optic effect; the heat is applied to the waveguides by a series of microheating resistances placed on the chip and controlled electrically with a dedicated control box. The whole chip has also been packaged with fiber arrays at both input and output with 4.2 dB total insertion loss on average.

For this chip, the fidelity parameter (Equation 2.21) has been calculated for various different classes of unitary matrices separately. To keep the comparison consistent with the results from Chapter (chapter), we report here that the average performance of this

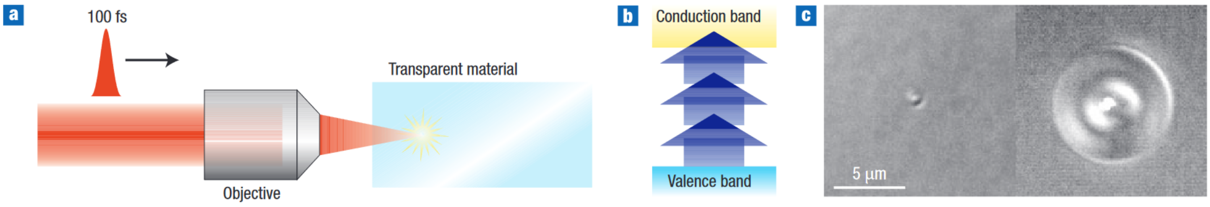

Figure 3.4: Femtosecond Laser Micromachining process. a) Schematic of the laser incident on a transparent material. b) Diagram of the excitation of electrons to the conduction band. c) Microscope images showing the large variation in the feature characteristics depending on the experimental conditions. Left: single 10-nJ pulse and right: 25,000 5-nJ pulses at a frequency of 25 MHz (both with the same focal spot). Figure from [41].

chip on the group of switching matrices was 0.953 while the performance on the group of random Haar matrices was 0.904.

3.2. Direct Laser Writing

With *direct laser writing* we refer to all the fabrication platforms that employ some localised modification of a material induced by absorption of laser light and the subsequent avalanche breakdown, with the aim to directly impress some three-dimensional structured design onto the material. In this landscape the technology we devolve most of our attention to will be Femtosecond Laser Micromachining (FLM) primarily because the devices used in the following chapters of this thesis have been fabricated using this platform.

In this section we also go further into the details of thermo-optic phase shifting and the design of microheaters in the context of FLM.

3.2.1. Principles of FLM Physics

Femtosecond Laser Micromachining (FLM) is a versatile fabrication platform for the direct, localised and deterministic modification of the refractive index of a material substrate. This technique can be used to machine materials down to the micrometer scale by inducing an avalanche breakdown within the material through nonlinear absorption of light [41].

The technique has been used to machine optical devices within a silica substrate, translating a sample under a focused laser beam to locally alter the refractive index of the substrate and thus achieving the direct writing of an optical waveguide [42]. The main advantage of FLM over planar processes is that it is a single-step, maskless process that

allows for both rapid prototyping of optical integrated circuits but also more complex configurations for the same circuits; this includes 3D configurations, as the focus is the only region affected by nonlinear absorption.
The same technique also has other relevant applications, in that it can be used also to fabricate microfluidic channels and to micromachine metals.

The main mechanism by which FLM acts is the nonlinear absorption between the material and an incoming train of femtosecond laser pulses with extremely high intensity (about 10 TW/cm^2). The high-intensity short pulses induce a free electron plasma in the material by nonlinear absorption, which then transfers the energy to the material in a few picoseconds, permanently modifying its properties [43].
We now briefly discuss the processes by which FLM operates. It is necessary to avoid linear absorption in the material; this is done simply by choosing a photon energy much smaller than the material band gap. Once this is achieved, the three main light-matter interactions going on within the material are: *multiphoton absorption*, *quantum tunneling* and *avalanche ionisation.*
Multiphoton absorption is the promotion of an electron to a higher energy band by means of absorption of two or more incident photons. Quantum tunneling occurs as the high electric field strength may deform the energy bands to the point where, at the same energy level, the difference in energy gap between the conduction and valence bands becomes so small that an electron's wavefunction may have a substantial component in the conduction band. In avalanche ionisation the electrons in the conduction band that absorb photons may climb up the band, but then they relax back down to the bottom releasing their energy; this energy, if higher than the band gap, may be picked up by an electron in the valence band which immediately gets promoted to the conduction band. This process can then begin anew, increasing exponentially from this first seed and leading to an avalanche effect. Of the three processes, avalanche ionisation is the most common effect as the photon energy does not need to come from multiple incident photons simultaneusly [43].

The main advantage of using short pulses in FLM is that long pulses do not reach the intensities needed to create the electron seed that induces avalanche ionisation by themselves. This seed for longer pulses can generally be obtained only with "external forces", be it a material defect or an impurity or even thermally excited electrons; this leads to an avalanche breakdown that is randomly positioned. Short pulses, on the other hand, achieve this process deterministically and hence are much more suited for precise micromachining.
The transfer of energy from the free electron gas created by these processes to the lattice then permanently deforms it, and depending on the photon energy this deformation may

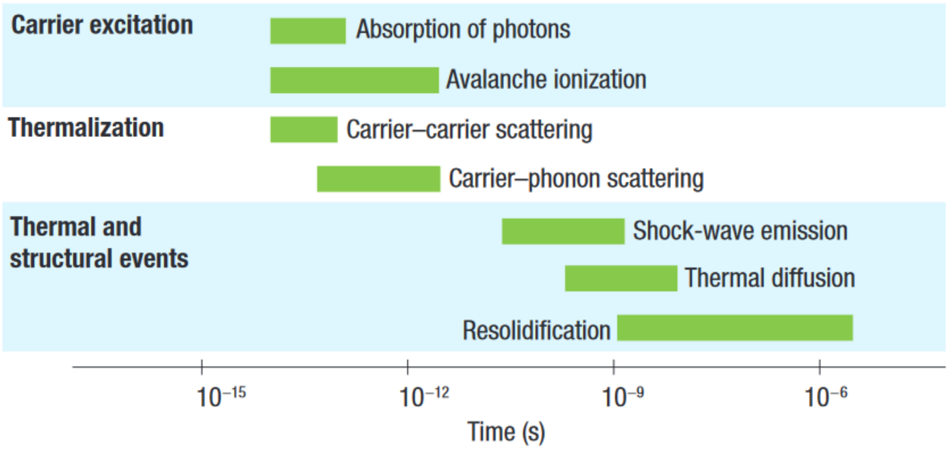

Figure 3.5: Timescale of the processes the material goes through after the interaction with a femtosecond laser pulse. The green bars represent the typical timescale; notice that while the interaction happens in a few femtoseconds, the "aftermath" of the interaction within the material may last for several microseconds. Figure from [41].

result in three possible outcomes: for low-energy pulses, a slight isotropic refractive index change of the material is induced perfect for waveguide direct writing; for intermediate energies, the refractive index change also takes on birefringent qualities; for high-energy pulses, the processes induce such a high pressure that they cause micro-cavitations in the material, effectively breaking it down leaving a void behind [44].

3.2.2. FLM Integrated Photonic Circuits

In waveguides written using FLM, the refractive index contrast is very low (10^{-3}-10^{-4}), which allows great compatibility with optical fiber technology and providing low coupling losses (2.5 dB) [45]. The most employed substrates, especially for integrated quantum photonics applications, are pure fused silica and commercial borosilicate glasses, e.g. Corning EagleXG and Eagle2000 or Schott AF32. Single mode waveguides have been fabricated in these materials covering the whole visible and near infrared spectrum of light, from 400 nm up to 1550 nm, demonstrating propagation losses in the range 0.1–1 dB/cm and negligible bending losses for radii above 30 mm [46].

While all FLM waveguides impress birefringent qualities in the substrate to some degree (10^{-4}-10^{-5} [47]), which can be used for polarisation-sensitive applications such as the fabrication of integrated waveplates [47], it has been shown that thermal annealing after the fabrication process can be used to quench the birefringence of written waveguides and thus obtain polarisation-insensitive integrated devices [48].

Another main advantage of FLM for integrated photonics is the ability to write on different material structures beyond just glasses, for example crystals [49]. In the landscape of integrated photonics this is invaluable, as the recent trend has been to produce each component of an optical setup in the material platform where it performs best, and then connect all the components together for packaging. FLM flips the usual way of designing integrated devices, as instead of finding the right design to implement a functionality on some material platform, it becomes possible to find the best material for a given functionality and write the component directly on it.

Passive circuits are surely within FLM's possibilities. In fact, soon after the first integrated photonic circuit was demonstrated with SOS [30], the coherent light interference effects necessary to create an integrated photonic circuit have been demonstrated on FLM too [50].
After this seminal demonstration several other integrated photonic devices have been fabricated using FLM, in particular for the quantum state tomography of single and multiphoton states involving several optical modes [51].
FLM has also been instrumental in the earliest demonstrations of boson sampling experiments [52].

For what concerns UPPs, the flexibility in the design process and the unique three-dimensionality of FLM allows for novel and interesting ways to design the complex networks required by these devices. First, phase shifts can be adjusted by modifying the S-bend of the directional couplers in the MZIs. Second, the transmission and reflection of each coupler can be manipulated by raising one of the waveguides out of the plane; this increases the pitch between waveguides in the middle section of the directional coupler without changing its length.
To date, active phase control in FLM waveguide circuits has been reported by exploiting the electro-optic [], elasto-optic [], or thermo-optic effect []. Of these, by far the easiest from a fabrication point of view is the thermo-optic effect, as phase shifters using this effect only require the fabrication of microheaters along the waveguides. The specifics of thermal phase shifting in FLM devices are detailed in the next section.

3.2.3. Thermal Phase Shifting in FLM Integrated Photonic Circuits

In the past years the research on Femtosecond Laser Micromachining has secured many achievements especially in the field of thermal phase shifting for FLM waveguides, thanks to the work of Ceccarelli and others [53]. The goal is to obtain high-performance low-power reconfigurable photonic devices, and FLM is the right platform to fabricate not only the optical components needed but also the structures that can be used to achieve this reconfigurability.

The main process by which reconfigurability is obtained in FLM waveguides is the thermo-optic effect. This is the dependence of a material's refractive index on the temperature, which stems from the statistical physics of the underlying atomic lattice achieving slightly different densities at different temperatures. Typically it is modeled as

$$n(T) = n_0 + n_1(T - T_0) \tag{3.1}$$

where $n_1 = \frac{\partial n}{\partial T}$ and n_0 is the refractive index at the reference temperature T_0. For the purposes of thermo-optic reconfiguration, the FLM platform has at its disposal the use of resistive microheaters to locally alter the temperature of the material; by the Joule effect, a current passing through a resistor will dissipate power depending on its resistivity and the square of the current. The main advantage of thermo-optic modulators (over, for example, electro-optic ones) is that they do not induce phase-dependent losses which is quite important in quantum photonics applications; unfortunately, they lose on the ground of bandwidth and speed as they are much slower than their electro-optic counterparts.

The design of the microheater is quite important for the efficient reconfiguration of the photonic device. Among the latest platforms available for the fabrication of these elements there is the sputtered gold on chrome film [54]: it consists of a chrome film deposited over the FLM substrate, on top of which a 100 nm thick layer of gold is sputtered. From the definition of resistance, we have

$$R = \rho \frac{L}{WH}. \tag{3.2}$$

We may define the *sheet resistance* $R_{sh} = \rho/H$ of the material, which in the case of a layer of 100 nm gold on 2 nm chrome is 0.6 $\Omega/\square$ [54]. Then the performance of the microheater depends mainly on the geometry of the deposited layer; the design employed in FLM waveguides consists of wide and short contacts (low *form factor* L/W) while the heating body is long and thin (high form factor). This design minimises the resistance of the whole microheater and focuses the power dissipation on the region where it is needed the most.

The advantage of using the FLM platform with this technology is that the same setup can be used to ablate the metal film. Thus, using the same laser setup it is possible to write both waveguides and the microheaters needed to control them.

As shown in Figure 3.6 the temperature profile induced in the substrate by a microheating

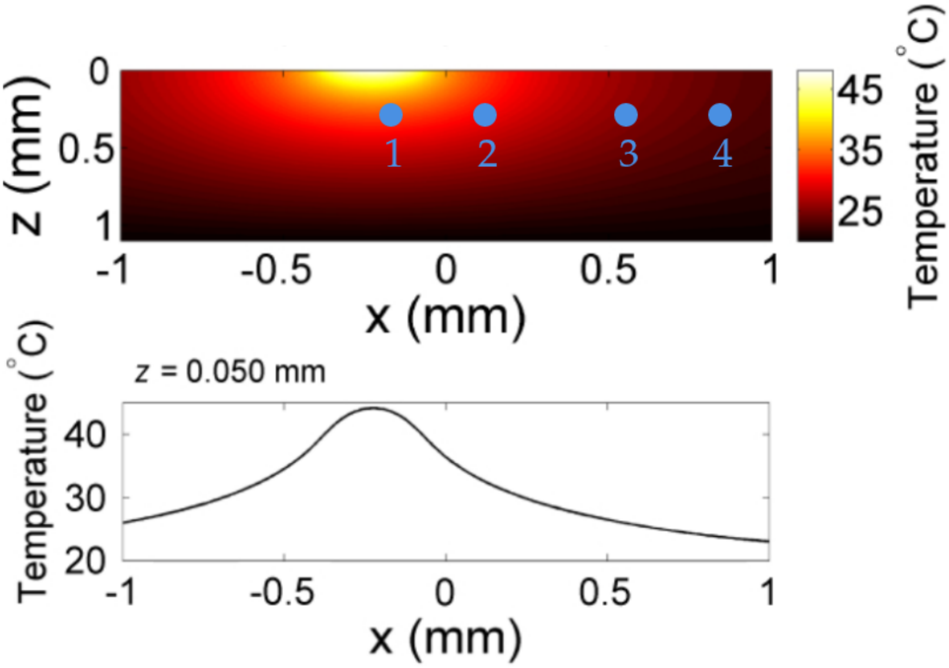

Figure 3.6: The temperature profile induced by a resistive microheater. 1-4 are waveguides (size not to scale); 1-2 may belong to the reconfigurable MZI of the microheater, 3-4 may belong to a different one. The temperature profile clearly extends beyond just waveguide 1, inducing thermal cross-talk. Figure adapted from [55].

device is quite extended spatially and may influence multiple waveguides. In general, for a length L of waveguide the phase shift induced on an optical signal passing through is

$$\varphi = \frac{2\pi L n(T)}{\lambda} \tag{3.3}$$

where L is the length of the waveguide we are considering, $n(T)$ is the refractive index as a function of temperature T, and λ is the wavelength of the signal. n has a spatial dependence that matches the pattern of Figure 3.6. In this example, we may imagine that the first two waveguides belong to a reconfigurable MZI while the other two belong to a different MZI. The refractive index change pattern extends beyond waveguide 1, the one below the microheater, reaching waveguide 2 as well as the other MZI.

This induces what is known as *thermal cross-talk*, in two different flavors: first, there is a thermal cross-talk between one MZI and a neighboring one, where modulating one MZI inevitably modulates the other; second, there is a thermal cross-talk within the same MZI, where both waveguides acquire a refractive index change. We now give a description of thermal phase shifting in this picture.

The induced phase shifts on two adjacent waveguides can be determined as follows:

$$\varphi_1 = \frac{2\pi L}{\lambda}(n_c + T_1 n_1), \quad \varphi_2 = \frac{2\pi L}{\lambda}(n_c + T_2 n_1). \tag{3.4}$$

Here T_1 and T_2 are the temperatures in Kelvin of the first and second waveguides, taking as first the one directly under the microheater as in Figure 3.6. What matters for the purposes of interference within an MZI is only the phase difference between the waveguides. Hence:

$$\Delta\varphi = \varphi_1 - \varphi_2 = \frac{2\pi L n_1}{\lambda}(T_1 - T_2). \tag{3.5}$$

It is evident here that the amount of phase shift depends on the temperature difference $T_1 - T_2$. This temperature difference depends on the power dissipated on the microheater, and this fact is exploited throughout our work to operate and calibrate the devices.
It will be important to remember that there is also a *common mode phase shift* induced on the waveguides by cross-talk of the second kind, calculated as the amount of phase shift that both waveguides undergo:

$$\Delta\varphi_{cm} = \frac{2\pi L}{\lambda}(n_c + n_1 T_2). \tag{3.6}$$

This amounts to a global phase, which does not matter in the operation of an isolated MZI. However, within a network, this common mode phase actually does matter; part of this work is devoted to understanding the effect that this common mode phase has on the network as well as finding means to compensate for it.

Thermal cross-talk is a serious threat to the performance of reconfigurable photonic integrated devices. Large part of this work is devoted to untangling the effect of thermal cross-talk of both kinds for the purposes of correctly operating UPPs.

3.2.4. Thermal Isolation Structures

While methods exist to work around the thermal cross-talk (as explained in Chapter 5) it is quite important to try and reduce the effects of this phenomenon with a physical intervention on the chip itself. To this end, in the past few years research has moved towards employing grooves on the glass, dubbed *trenches* [55].
For FLM devices several different kinds of trenches have been proposed, not least of which are deep trenches and bridge waveguides (Figure 3.8). It is important to remark that thanks to the FLM platform these trenches too can be micromachined direcly into the glass using a femtosecond pulse laser, yet again solidifying the technique as an all-in-one tool for the direct writing of integrated photonic devices.

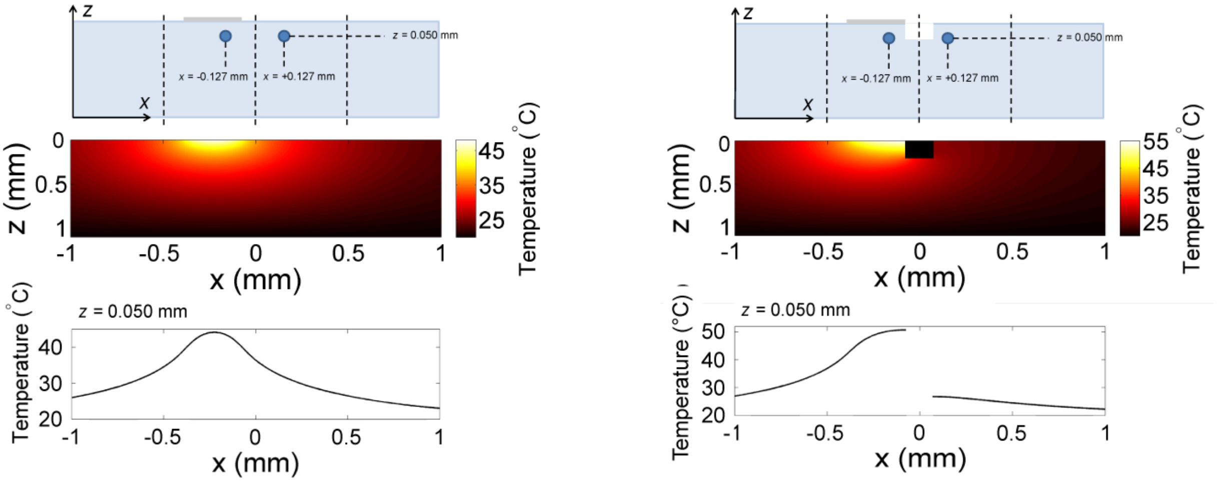

(a) (b)

Figure 3.7: The effect of adding a trench in an FLM device. a) Shows the device without a trench, with the waveguide structure detailed at the top. b) Shows the device with a trench; comparing this with a) the reach of the temperature profile is clearly reduced as highlighted below. Figure from [55].

Thermal phase shifters in FLM devices suffer from high power dissipation, as the power necessary to induce a 2π shift of the phase can reach hundreds of mW [56]; this, coupled with the fact that phase shifters scale up with the number N of modes like a quadratic function, means that the power needed for larger and larger chips becomes simply too big to handle if one still wants to keep the compactness. In fact with this level of power dissipation an optical chip can handle no more than a dozen phase shifters before needing active cooling, which would take substantial space in any setup. The quest for low-power reconfigurable devices is thus still an urgent engineering challenge.
In this regard, trenches offer lower power needed to achieve a 2π phase shift. Especially for deep and bridge trenches, the temperature change induced by the power is concentrated in a smaller area compared to the case with no trenches at all, hence much less power is needed to achieve the same temperature change in the region where it matters most (the waveguide). With 300 μm deep trenches, an integrated photonic device where the waveguides are located 127 μm away from one another will only need 57 mW of power to achieve a full 2π shift; without trenches, the same device needs 611 mW [54].

Apart from reducing power dissipation on the individual MZI, trenches are a viable solution to reduce the amount of cross-talk of the first and second kind as described in the previous section. This is because they simply remove the material that could transfer the heat from one waveguide to the next; if the chip is operated in air, heat transfer is then primarily due to the air itself. For this reason, thermal cross-talk is significantly reduced when a chip with built-in trenches is operated in vacuum [54]. Part of this work is devoted to measuring this effect for devices featuring deep trenches.

In the landscape of reconfigurable devices it is worth mentioning how choosing to operate with thermo-optic phase shifters affects a device's temporal response. First, we have mentioned that thermo-optic phase shifters are among the slowest phase-shifting mechanisms, thus being mostly bound to low-frequency applications.
To gauge the dynamic response of thermal phase shifters, then, one can measure the time constant of their response to a step function as the *switching time*. For non-isolated waveguides, this switching time was found to be 12 ms. Trenches in this respect do not give a performance boost, in that the switching time for deep and bridge trenches was measured to be in the order of 50 ms [54]. However, it is also important to note that this needs to be compared with a substantial decrease of the power needed to achieve the same phase shift, as mentioned earlier. In fact, to properly compare the performance of trenches over no isolation structures, the figure of merit $P_{2\pi}\tau/\lambda$ may be introduced, where $P_{2\pi}$ is the power needed to achieve a full 2π shift, τ is the shifting time, λ is the optical signal's wavelength. The smaller this figure of merit, the better the performance.
The experiments show that even though the time constant increases, the large decrease of the figure of merit are a testament of the better overall performance of trenches over non-isolated waveguides.

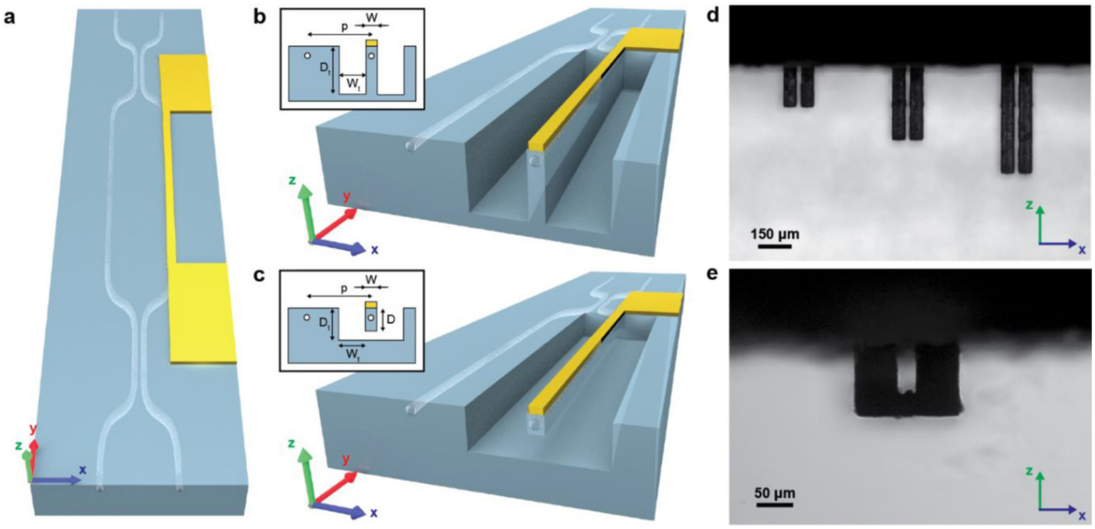

Figure 3.8: The structure of the reconfigurable MZIs in state of the art FLM UPPs. a) Basis structure of the device with no isolation structures. b) Cross section of the device with deep isolation trenches. c) Cross section of the device with the bridge waveguide. d) Photomicrograph of the isolation trenches (D_t = 150, 300, 450 μm) seen through the side of the substrate. e) Photomicrograph of the bridge waveguide seen through the side of the substrate. Figure from [54].

4 | Materials and Methods

In this section we describe the integrated 6-mode UPPs and the experimental setup used for calibrating their operation.

4.1. 6-Mode UPPs

In this section we describe the two 6-mode UPPs employed in this work. Both devices share the same topology and electrical connections, making them the same for the purposes of their calibration and operation. We shall refer to these devices as A and B respectively. Figure 4.1 shows pictures of device A connected to the Qontrol interposer board through cables and mounted on the four-axis manipulator.

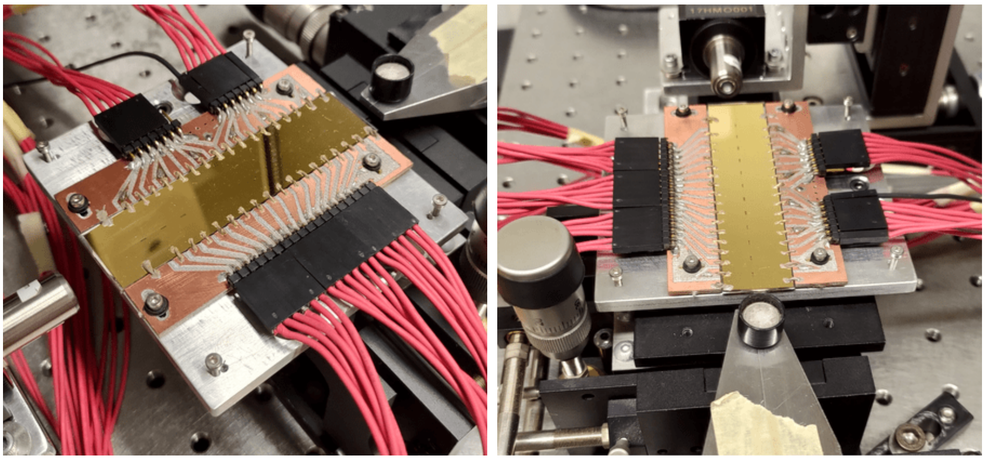

Figure 4.1: The UPP device labeled A. The circuit is connected to the interposer board with the red cables with the pins provided by the printed circuit boards. The black cable instead connects the ground.

The topology of the optical circuit is displayed in Figure 4.2, while the schematic of the circuit from the electrical point of view is shown in Figure 4.3. In particular, each device consists in a network of 15 MZIs arranged according to the Clements configuration (Section 2.2.4), which implies six coloumns of MZIs where each coloumn features sets of 3 or 2 (alternating) devices. Each MZI features two resistive microheaters deposited on

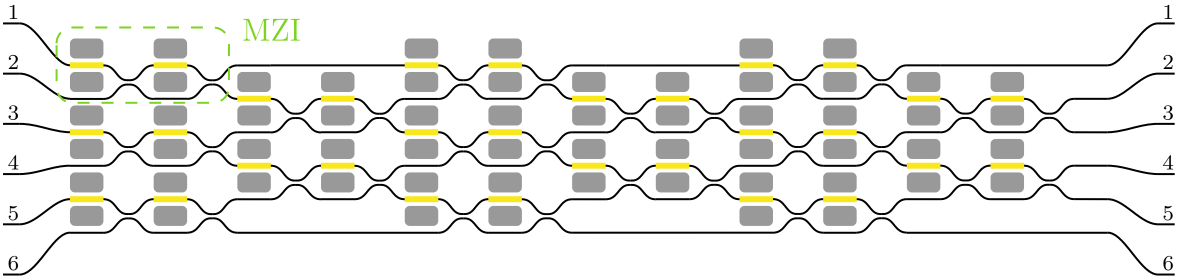

Figure 4.2: The scheme for the UPPs on which all experiments have been performed. The thin dark lines correspond to FLM waveguides; the yellow thicker lines correspond each to a microheater; the distance between straight waveguides is 80 nm while the distance between two ports is 127 nm. Around each microheater is a pair of deep trenches separating each waveguide with the next waveguide over. The group of 2 horizontally aligned directional couplers with microheaters constitutes an MZI of the network.

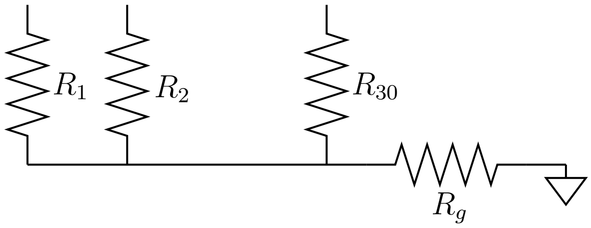

Figure 4.3: The electrical scheme of the UPP in the ideal case. There are 30 resistive microheaters, with resistance values R_i ($1 \leq i \leq 30$), all connected to the same ground node. In reality, between the common node of the microheaters and the ground a small resistor should be considered, with a ground resistance R_g. The electrical control can provide up to 24 mA or 5 V to each resistor separately.

the chip surface, to control its operation.
The circuits were fabricated using FLM on Corning EAGLE XG alumino-borosilicate glass at Politecnico di Milano. The length of the whole borosilicate glass wafer is 8.5 cm, with 2 cm width and 1.1 mm thickness. The waveguides and the directional couplers are optimised for a wavelength of 785 nm. The network features six input ports (as a convention, we take the input to be on the left even though the device is entirely reciprocal) and six output ports. The pitch between ports is 127 μm, however this is not the same as the inter-waveguide distance inside the network which is instead equal to 80 μm. Around each microheater there is a pair of 300 μm deep trenches for thermal isolation, for a total of 60 trenches. The trenches, too, were fabricated with FLM.
To connect the microheaters using pins, a pair of printed circuit boards (PCBs) were added; the PCBs have one ground pin each, however the two grounds are also connected together, hence they constitute a single ground node. One PCB features 18 pins, including the ground one, connecting 17 microheaters; the other features two groups of 7 pins including the ground one, for a total of 13 microheaters connected to the pins.
Finally, an array of optical fibers (780HP single-mode) was permanently glued at the input ports of device B. For this reason, while device A needs the fiber-butt approach to couple light into the input ports, device B can receive light from the laser source using the optical fibers instead.

4.2. Classical Light Coupling

The most important step in the calibration of any integrated photonic device is to take a light signal and run it through the device in order to determine its optical properties. In this work, the light signal was provided by two laser sources (785 nm, 793 nm), and they have been coupled into the input ports of the device using the fiber-butt approach.

In the fiber-butt approach, the fiber end is aligned to the chosen input port with precision, and put almost in contact to it. Before using the fiber this way it is necessary to cleave, peel and clean one end of the fiber. The other end of the fiber receives laser right by means of an objective focusing the beam into it. To couple both light signals, a 780HP single-mode fiber was used.
The focusing from the laser source into the single-mode fiber was performed with a lens of NA equal to 0.25 and coating B. This lens was mounted on a three-axis positioning system (Melles Griot NanoMAX).
Stable and precise positioning systems are needed to guarantee the alignment of the lens or fiber. For the purposes of this work, the fiber was mounted on the three-axis position-

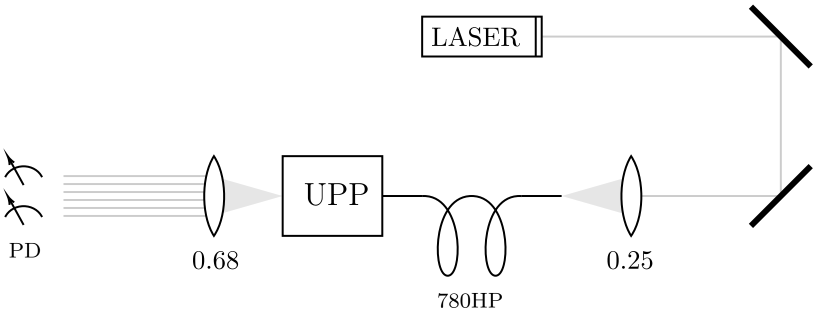

Figure 4.4: The optical setup of the experiments. The laser sources (785 nm, 793 nm) are coupled into the single-mode fiber through a NA = 0.25 lens; the alignment is performed manually using a pair of mirrors, represented here by thick lines. After this stage, the fiber is aligned to an input port of the UPP; the light coming out of the UPP is then collected by another lens (NA = 0.68) in such a way that two output ports are focused on two different photodiodes (PD).

ing system while the chip itself was held on a four-axis manipulator (Thorlabs MBT 402). The latter has two translational degrees of freedom and two angular degrees of freedom to adjust for tilts. Finally, the light at the output of the device is collected with an aspheric lens (NA = 0.68 coating B) mounted on the automated stages described in Section 4.4. The optical power collected by the output aspheric lens was measured using up to two Ophir NovaII photodetectors connected with Ophir PD300R-IR photodiodes. These photodiodes were used to collect power from two different ports at the same time. Both photodiodes were used when performing normalised measurements, such as the cross-talk measurements described in Section 5.2.1; in other experiments, collecting power from two ports was not necessary and only one was actually used.

4.3. Electronics and Current Control

As explained by Ref. [53], controlling the device by applying specifically currents and not voltages is essential to a correct operation of the circuit. In fact, consider a set of resistors connected all at the same ground node; this represents the ideal configuration of microheaters within the UPP device (Figure 4.3). In practice, there is also a small parasitic resistance R_g between the shared node of all the resistors and the actual ground. By setting the voltage on any set of microheaters, then, the total current induced on the parasitic ground resistance will affect the voltage V_i across the i-th microheater as a voltage divider:

$$V_i = V_{set} - R_g \sum_j \frac{V_j}{R_j} \tag{4.1}$$

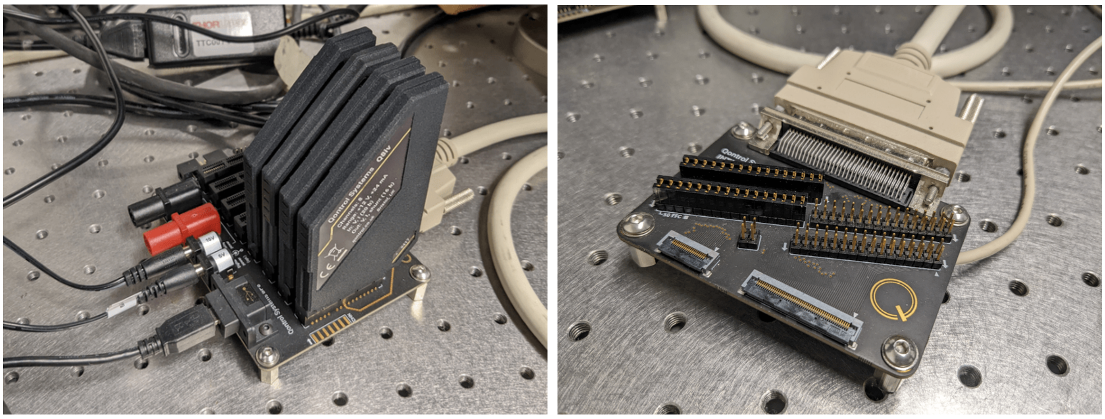

Figure 4.5: The Qontrol devices used for the current control. On the left, the main board with the four Q8iv microcontrollers mounted on top. On the right, the interposer board that allows easy connection between the channels and the actual circuit.

where V_{set} is the ideal set voltage on the microheater, R_g is the ground resistance, R_j the resistance of the j-th microheater and V_j the voltage across it. This means that the power dissipated by a microheater depends on the power dissipated on every other microheater simply due to *electrical cross-talk*, which makes the operation of the circuit very difficult. This effect is not present if one controls the circuit by setting the currents.

In order to control the currents applied to each of the 30 microheaters on the device, a Qontrol Q8iv Microcontroller setup has been used. Microcontrollers in the context of reconfigurable photonic integrated devices are extremely helpful to streamline the operation and calibration steps, as they provide the means to apply currents to many different microheaters independently at once.
On each channel, the Qontrol Q8iv can provide a current up to 24 mA and a voltage up to 12 V. These devices can be controlled using Python as an interface; the interface provides basic functionality to apply or measure currents and voltages of the channels.

The specific setup used for the calibration and control of the 6-mode UPP is shown in Figure 4.5 and consists of:

- Qontrol BP8 backplane, which is a circuit board that provides connectivity for both 5V and 15V power supplies as well as USB connectivity to control the Qontrol Q8iv.
- Qontrol INT8GGB interposer board, a printed circuit board with pins for easy access to the channels.
- Four Qontrol Q8iv.
- Electrical cables to connect the pins on the interposer board to the pins on the UPP.

4.4. Automated Stages

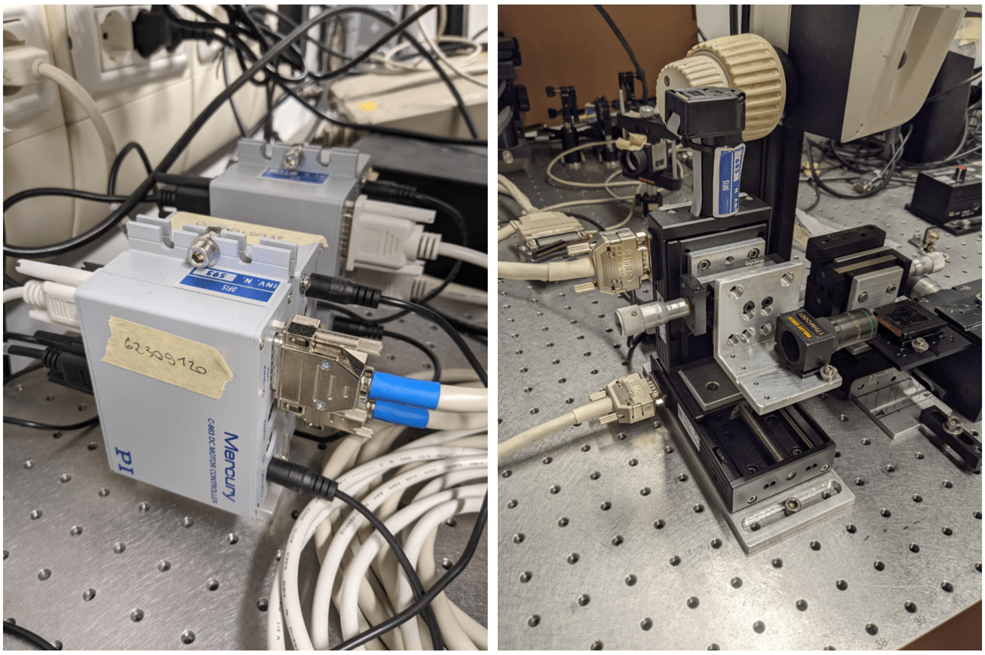

Figure 4.6: The automated stages used for the experiments. The Mercury Servo Controllers are shown on the left while the moving parts are shown on the right. The moving parts also have an extra manipulator (manual) used to adjust the position of the objective along the optical axis.

In order to move the objective lens between the output ports of the device a pair of motorised translation stages have been used, controlled by C-863 Mercury Servo Controller. These are servo controllers for the direct actuation of DC motors. In particular, for motion parallel to the plane of the optical bench, we used a 62309120 VT-linear stage; this stage has a range of 50 mm with a repeatability of the motion in both directions of ±10 μm. For motion perpendicular to the plane of the optical bench, we used a 62309110-0000 VT-80 stage; the range of this stage is 25 mm with a bidirectional repeatability of ±10 μm. A high repeatability was necessary for the purposes of reliably measuring the same output port on the UPP many times over after switching to different ports. The setup is shown in Figure 4.6.

In this way the collection of optical power at the output of every port has been automated, and it has made possible the measurement of many different configurations of the circuit for the purposes of fidelity estimation.

The automated stages come with proprietary software (PIMikromove) from the manufacturer which can be used to finely control the position of the stages one at a time, but for the purposes of automated measurements they have also been operated through a Python interface provided by the manufacturer.

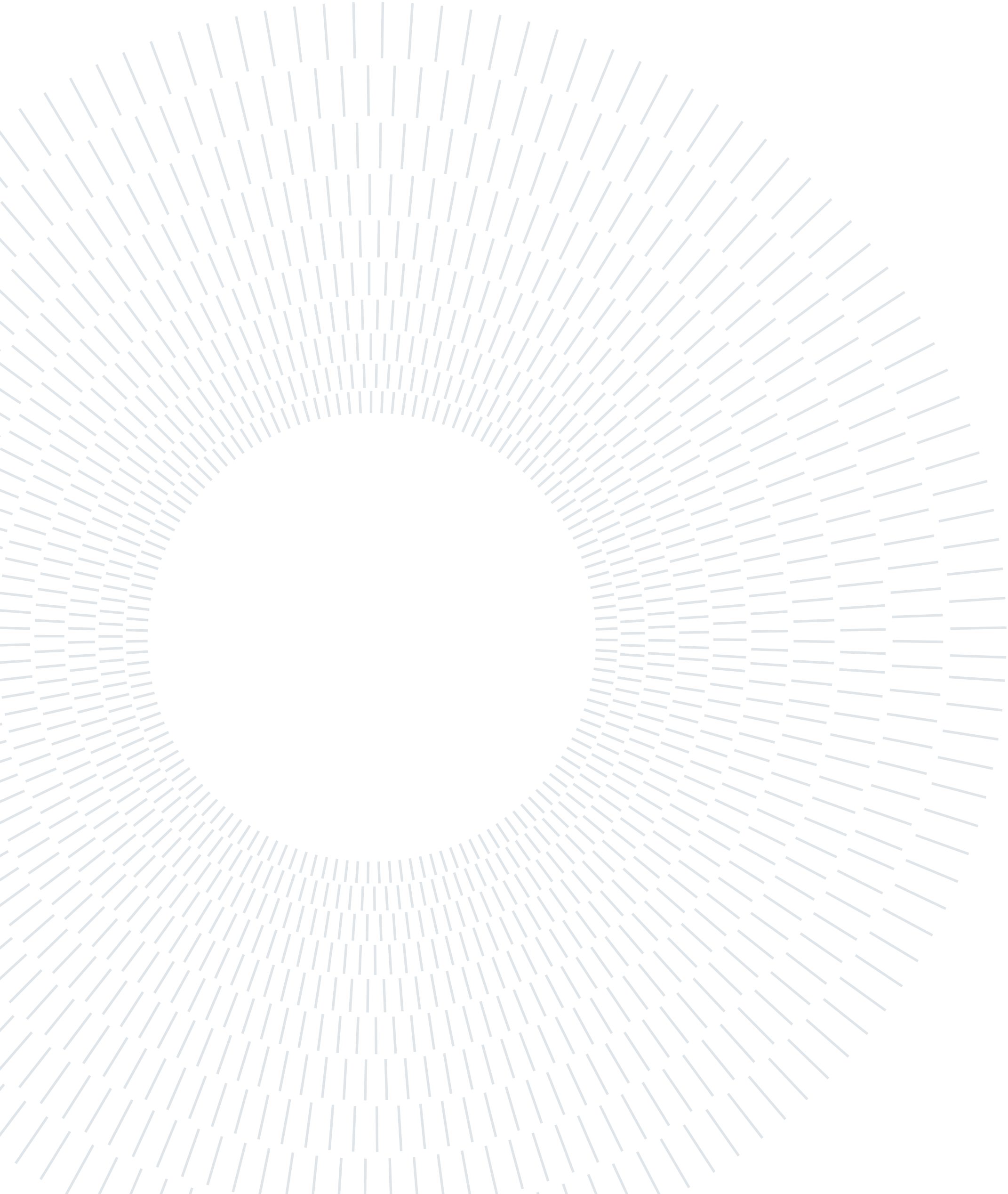

5 | Calibration of the 6-mode UPP

In this chapter and the next we present the bulk of the work performed on the 6-mode UPP. The device, as detailed in the previous chapter, consists of 15 reconfigurable MZIs each of which is controlled using two microheaters. The end goal is to understand how to control the 30 microheaters of the UPP in order to implement an arbitrary unitary transformation between the input and output states. Mathematically, this means finding the function that maps unitary matrices to sets of currents on the microheaters. This operation is nontrivial and is heavily influenced by the specific technology used to build the UPP.

Indeed, the fabrication process admits an error margin on the length of the straight waveguides from one directional coupler to the next, so every pair of waveguides connecting two couplers may have different optical lengths. Unfortunately, the difference in optical length between the couplers is exactly what determines the phases of each reconfigurable MZI. This implies that after the fabrication, without the application of any current, there is a random distribution of phases θ_0, ϕ_0 for each reconfigurable MZI in the network. We refer to these phases as *static phases*.

Moreover, we distinguish the phase shifters that straddle two close-by directional couplers (the ones that form the body of an MZI) from those that do not; the first kind are called *internal phase shifters*, and thus the phases they implement are called *internal phases*; the others are called *external phase shifters* and *external phases* respectively. Internal phase shifters therefore are those that induce changes in θ, while external phase shifters induce changes in ϕ. With reference to Figure 4.2, for the MZI circled in green the microheater on the left is the external one, while the microheater on the right is the internal one. In this chapter and the next we use a more compact diagram to represent MZI networks (Figure 5.1) where every crossing represents one MZI.

In order to operate this device, then, we first need to measure the values of θ_0 and ϕ_0 for each MZI in the network, as well as gain an understanding of how the power dissipated by a microheater alters the internal and external phases. Explaining how to do so is the aim of the current chapter.

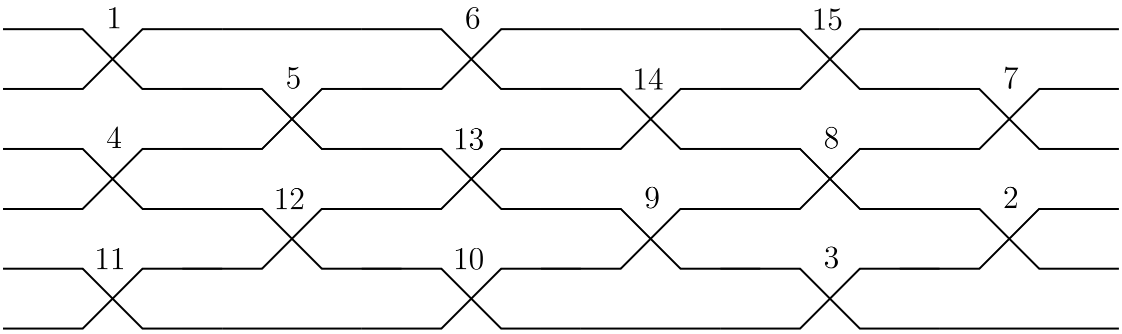

Figure 5.1: The compact version of the diagram of the 6-mode UPP. The MZIs are numbered according to the order in which Clements' algorithm solves their parameters (Section 2.2.4). With reference to Figure 4.2, a crossing in this diagram corresponds to an entire MZI including both microheaters. Then, MZI 1 in this diagram corresponds with the MZI circled in green in Figure 4.2.

5.1. Linear Model of Thermal Phase Shifting

The very first step in understanding the behaviour of the device is to find the relationship between the input electrical current and the amount of phase shift induced on the MZI by the resistive microheaters. As a first step, we begin from the internal phases.

According to the prior analysis, the internal phase shift of the MZI is given by

$$\theta = \theta_0 + \Delta\theta. \tag{5.1}$$

Here, θ_0 is the static phase, and $\Delta\theta$ is the *variable phase.* The variable phase depends on the physical quantity used to control the phase shifter; in our case, this physical quantity is the electrical current flowing through the resistive microheater.

As explained in Section 3.2.3, the electrical power dissipated by a phase shifter heats up the waveguides inducing a change in the refractive index. The differential change of refractive index is what determines the change $\Delta\theta$. We assume a model where the relationship between the differential temperature change and the dissipated power is linear; hence, from Equation 3.6, we obtain a linear relation between the variable phase and the power:

$$\Delta\theta = \frac{\alpha}{R_0} P. \tag{5.2}$$

We introduce the proportionality constant α, called *tuning coefficient.* R_0 is the resistance of the microheater, measured at low-voltage, P is the power dissipated on it. Then, by

Ohm's law and assuming the resistance of the microheater is constant, we have

$$\theta = \theta_0 + \alpha I^2. \tag{5.3}$$

Therefore, when the single MZI is actuated, its reflection and transmission will vary according to the following model as we know from Chapter 2:

$$\mathcal{T} = \cos^2\left(\frac{\theta_0 + \alpha I^2}{2}\right), \quad \mathcal{R} = \sin^2\left(\frac{\theta_0 + \alpha I^2}{2}\right). \tag{5.4}$$

The aim of this section is to understand how to exploit this behaviour to obtain the values of θ_0 and α.

First, whenever we have light at only one input of a reconfigurable MZI we can employ a simple procedure to extract $\mathcal{T}(\theta)$ and $\mathcal{R}(\theta)$. We set the current I^2 on the MZI to increase linearly with time; we refer to this function as a *current ramp*. Then, we measure the optical power at the *cross* output of the MZI and plot it against time. What we see is a sinusoidal plot, which we can now fit using a curve fitting algorithm or software. In particular, as Equation 5.4 shows, the fitting function must have the form

$$f(I^2) = A\cos^2\left(\frac{\theta_0 + \alpha I^2}{2}\right). \tag{5.5}$$

A is the total optical power output, and comes in as an extra curve fitting parameter. The resulting plot is not an exact sine or cosine function but it includes a nonlinear effect, which we describe how to adjust for in Section 5.1.1. Figure 5.2 shows the typical plot obtained at the end of this process, both before and after adjusting for the nonlinearity.

Once the curve fit has been completed and the data has been adjusted for nonlinearity, it is possible to extract the values of θ_0 and α through curve fitting. Moreover, the curve fit can find the values of current that set the MZI to the *reflection point* ($\theta = \pi$) or *transmission point* ($\theta = 0$); these currents are labeled as I_π and I_0 respectively.

5.1.1. Nonlinearity

The model we adopted in Equation 5.2 works across a wide range of values, as the experimental data confirm, however the relation between power and current in our device is not as simple. Knowing this relation is necessary in order to operate the device, since as explained in Section 4.3 we need to operate the device by setting the currents.

As Figure 5.3 shows, when plotted against the current squared we obtain a nonlinear

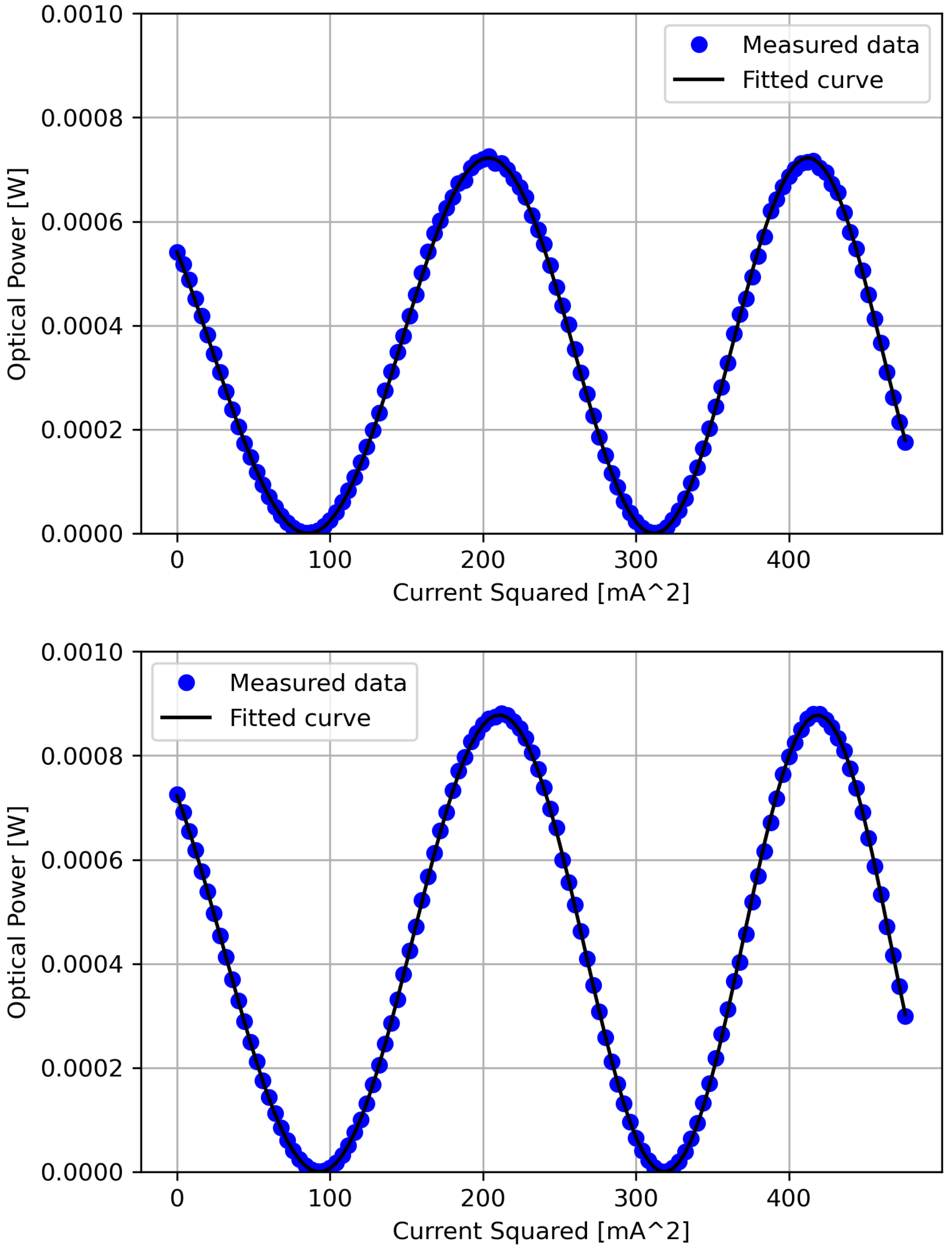

Figure 5.2: Two typical graphs obtained from a current ramp measurement. The blue dots correspond to the measured data, while the curve fit is shown in black. Minima and maxima correspond respectively to reflection points and transmission points.

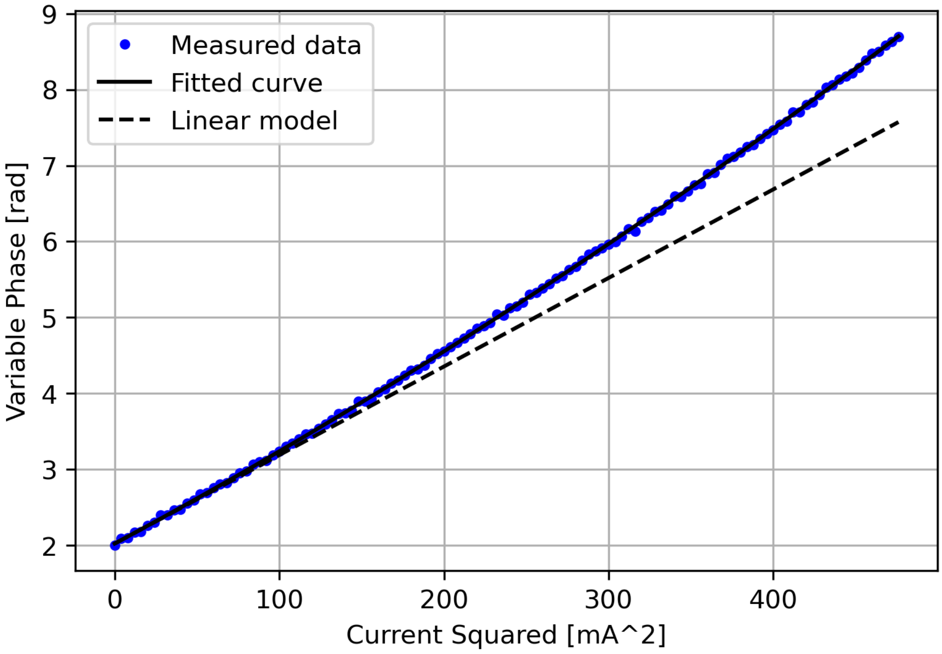

Figure 5.3: Dependence of $\Delta\theta$ on current squared. These results were extracted by inverting the transmission function of an internal phase of device B, obtaining the argument of the function. The data deviate substantially from linearity in I^2.

function for $\Delta\theta$. The general relation between power and current is given by Ohm's law:

$$P = RI^2. \tag{5.6}$$

Here R is the resistance of the device, I is the current; in general, R may depend on I too. This is because the resistivity of metals depends linearly on the temperature in our range of interest, which itself depends on the current, hence large currents induce a change in R. If R was constant, we would obtain a linear relation between I^2 and P; this is not the case, hence we need to include a second order term in I^2 in order to better describe the relation. In other words,

$$P = R_0 I^2 + \sigma I^4. \tag{5.7}$$

This implies that the variable phase is a fourth-order polynomial in the current:

$$\Delta\theta = \alpha I^2 + \alpha \frac{\sigma}{R_0} I^4. \tag{5.8}$$

Mathematically, Equation 5.7 can always be inverted to obtain I from P because σ is much smaller than R_0 in absolute terms. Therefore, for the purposes of this thesis, the nonlinear relation between power and current does not jeopardize the uniqueness of solutions to obtain a specific θ; in other words, there are not multiple values of the current that yield the same exact θ.

Despite this, the addition of an extra parameter further complicates the process of curve fitting and requires one to obtain samples with bigger resolution in order to find a good fit. The ratio σ/R_0 was measured to be of the order of 10^{-4} mA^{-2} for every microheater in the network.

We can therefore introduce an *adjusted current square* Q, defined as follows:

$$Q = I^2\left(1 + \frac{\sigma}{R_0}I^2\right). \tag{5.9}$$

Hence, the model for $\Delta\theta$ is linear in this new parameter, and we can write $\Delta\theta = \alpha Q$. It is important to remark that there is a level of nonlinearity hidden within Q every time we write it, so the conversion from Q to current is not as straightforward as a square root but requires inverting a quadratic function; this quadratic function depends on the microheater in question too, so we have to keep tabs on an extra parameter (the ratio σ/R_0) for each microheater.

5.2. Calibration of Internal Phases

So far we have understood how to obtain the relevant parameters of the relationship between power and phase shift for a single MZI, but the real challenge lies in decoupling the effect of every single MZI in the network from all others. In fact, the circuit is so interconnected that trying to apply the curve fitting algorithm as detailed above without any sort of preparation will surely be fruitless.

In particular, in order to use the curve fit target function correctly (Equation 5.5), it is necessary to route the optical signal entirely into one port of the MZI and then retrieve the optical power output from the correct ports. Failing to route the light into only one port, or measuring the output from the wrong port amount to obtaining the wrong value for the static phase.

In the literature we can find a method to sequentially calibrate each MZI for a Reck configuration [11]; we took it as a starting point in this work and developed a method for the case of the Clements configuration, which we now describe.

In what follows, inputs and outputs as well as MZIs are numbered according to Figure 5.4. We reference the steps of the procedure both in the case of the 6-mode UPP and a general N-mode one.

1. Align the laser light to the input port 1.

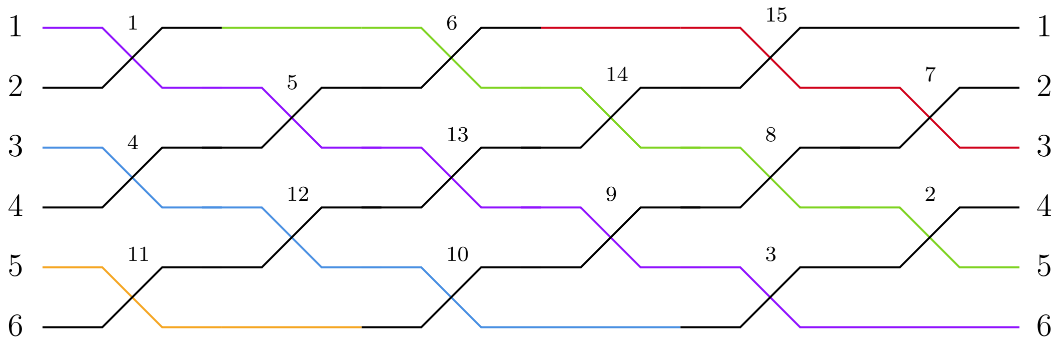

Figure 5.4: The compact version of the diagram of the 6-mode UPP with the diagonals highlighted. The MZIs are numbered according to the order in which Clements' algorithm solves their parameters (Section 2.2.4).

2. Consider the line of MZI that connects input port 1 with output port 6, coloured in purple in Figure 5.4. This is the *main diagonal*. Begin by sending a current ramp onto the first MZI along this diagonal (MZI 1), measuring output port 6 with one power meter. In an N-mode device, the output port would be N instead.
3. When the curve fit step is completed for MZI 1, set it to the trasmission point ($\theta = 0$). Continue by sending a current ramp onto the second MZI along the main diagonal (MZI 5), always measuring the same output port.
4. Repeat the process above for every single MZI on the main diagonal (1, 5, 13, 9, 3 in Figure 5.4), setting the previous to the transmission point and measuring the next.
5. When all the MZIs on the main diagonal have been calibrated, set MZI 1 to the reflection point ($\theta = \pi$). Now, all the optical power is redirected to MZI 6.
6. Consider the line of MZI that connects this device with output port $N - 1$. This is another diagonal, but it sits above the main diagonal. We call this the *first upper diagonal*, coloured in green in Figure 5.4. Likewise, the diagonals that sit above this will be the second upper, third upper, and so on. Begin by sending a current ramp onto the first MZI along the first upper diagonal, measuring the output port 5 with the power meter. In an N-mode device, the output port would be $N - 1$ instead.
7. Repeat the process of setting to transmission every MZI along the first upper diagonal (6, 14, 8, 2) and measuring the next keeping the same output port.
8. Repeat the entire process of measuring diagonals for the second upper, third upper, and so on; the output port should be $N - 2i + 1$ for the i-th upper diagonal in an N-mode device. In the case of 6-mode, then, when measuring the second upper

diagonal the output port should be 3.

9. So far, this calibrates the top half of the circuit above the main diagonal. In order to calibrate the bottom half, it is sufficient to change the input port. Change the input port to 3, and then set the last MZI along the main diagonal (MZI 3) to the reflection point. From now on the output port of interest will be 6 (the N-th for the general device).
10. Calibrate the entire first lower diagonal - i.e. the optical path that connects input port 3 with output port 6 staying fully below the main diagonal, coloured in blue in Figure 5.4 - using the same method. At the end, set the last MZI to the reflection point (MZI 10).
11. Set the input to 5 calibrating each lower diagonal with the method explained above. For a general N-mode device, the process must be repeated for every other odd-numbered input (5, 7, 9 and so on).

By the end of this process, we obtain complete information about the internal phases and completely calibrate their behavior with respect to the current flowing through the microheaters. Tables 5.1 and 5.2 show the measured values of $\theta_0, \alpha, I_\pi, I_0$ for each MZI on the two 6-mode UPPs.

MZI	α $[\Omega/W]$	θ_0	I_π $[mA]$	I_0 $[mA]$
1	22.243	0.180	11.770	16.475
2	30.383	0.861	9.177	13.840
3	26.256	1.093	8.716	13.593
4	22.285	0.523	10.645	15.439
5	22.496	1.401	9.535	15.519
6	21.275	0.446	11.804	16.982
7	23.732	1.421	9.000	14.757
8	21.851	0.193	11.285	15.919
9	26.508	1.324	8.756	14.138
10	28.107	1.275	8.814	14.108
11	27.412	0.887	9.171	13.879
12	28.516	0.989	9.408	14.397
13	23.456	0.018	12.263	17.015
14	21.018	1.253	10.008	15.961
15	20.434	0.592	10.956	16.018

Table 5.1: The data measured for device A using the procedure detailed in this section. The numbering of the MZIs follows Figure 5.1.

MZI	α $[\Omega/W]$	θ_0	I_π $[mA]$	I_0 $[mA]$
1	20.225	0.178	12.376	17.304
2	26.118	0.869	9.643	14.514
3	26.175	1.049	9.250	14.267
4	22.152	0.594	11.246	16.345
5	18.459	1.382	9.914	16.077
6	18.511	0.449	12.264	17.593
7	20.601	1.428	9.453	15.455
8	22.266	0.214	11.930	16.729
9	23.024	1.360	9.008	14.582
10	23.292	1.276	9.161	14.628
11	25.876	0.905	9.606	14.545
12	23.415	0.955	9.787	14.912
13	19.828	0.042	12.833	17.709
14	18.277	1.300	10.287	16.435
15	20.417	0.625	11.461	16.712

Table 5.2: The data measured for device B using the procedure detailed in this section. The numbering of the MZIs follows Figure 5.1.

5.2.1. Cross-Talk

In a general operation of the circuit, it is necessary to actuate multiple adjacent MZIs. As explained in Section 3.2.3, the reconfiguration of an MZI through the thermo-optic effect induces a phase shift not only on the MZI of interest but on all other neighboring MZIs. This means that the model of Equation 5.3 cannot be used as it doesn not take into account this cross-talk effect. In a more correct model, then, the value θ_i for the i-th MZI depends on every single MZI in the network:

$$\theta_i = \theta_{i0} + \sum_{j=0}^{N} \alpha_{ij} Q_j. \tag{5.10}$$

Therefore, the tuning coefficient α is now a *tuning matrix* with entries α_{ij}.
It is worth mentioning that a complete model would include the thermal cross-talk of all 30 phase shifters. The most complete cross-talk matrix should therefore have 30^2 nonzero entries. However, thanks to the wide gap (3mm) between neighboring columns on the chip no appreciable cross-talk could be measured for phase shifters on different columns. Because of this, most terms of the tuning matrix are null and therefore it becomes much more convenient to only think of the matrix in terms of the nonzero blocks.

The diagonal elements of the tuning matrix α_{ii} are just the values of α obtained at the end of the calibration process of Section 5.2. We now explain the method we developed

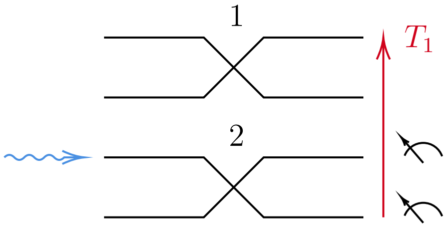

Figure 5.5: Schematic representation of the setup to measure the cross-talk. T_1 is the temperature profile induced by the microheater of MZI 1 and the arrow represents the direction of increasing temperature. In this example, the result of the curve fit would determine the element α_{21}.

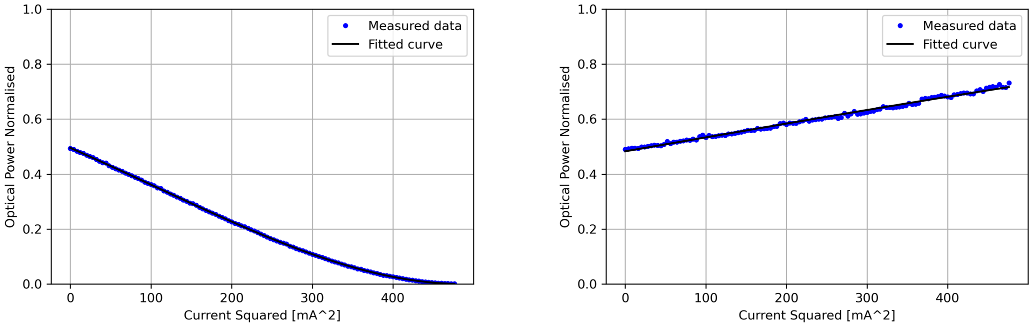

Figure 5.6: Typical graphs of cross-talk measurements. Both measurements have been performed on device B and represent different tuning coefficients. On the left, we are measuring the effect that an MZI has on the first neighbor located above it; the coefficient turns out to be negative, as evidenced by the negative derivative at zero of the sinusoid. On the right, we are measuring the effect that an MZI has on the second neighbor below; the coefficient is positive, but quite small, hence the graph looks more similar to a line than a sinusoid.

to measure the off-diagonal elements.

With reference to Figure 5.5, in order to measure the effect of the cross-talk on MZI 2 induced by MZI 1 we set up two power meters at both outputs of MZI 2. This will allow us to normalise the power output, which is a crucial step in curve fitting as we will explain later. We redirect the laser light onto the first input of MZI 2, as the Figure shows. Then, we set MZI 2 to $\theta_2 = \pi/2$; this configuration evenly splits the input power, and corresponds to the point of the transmission (Equations 5.4) where the derivative achieves its maximum value - i.e. we are most sensitive for changes in θ_2. Moreover, we turn off all other MZIs that may have an effect on MZI 2.

This setup implies that Equation 5.10 reduces down to

$$\theta_2 = \frac{\pi}{2} + \alpha_{21} Q_1. \tag{5.11}$$

We measure the power output while sending a current ramp to MZI 1. The typical graphs for the measured power output in this process are shown in Figure 5.6. We then fit the data using the target function

$$f(Q_2) = \sin^2\left(\frac{\pi}{4} + \frac{\alpha_{12}}{2} Q_2\right). \tag{5.12}$$

Normalising the power was necessary, since α_{21} could be so small that the data essentially become just a linear graph. Fitting a line with a sinusoidal function can be quite hard with no prior knowledge of the amplitude, and will result in a poor accuracy of the fitted parameters. Normalising ensures that the amplitude of the target sinusoid can be assumed equal to 1 or close to 1.

Using this method we can measure the whole matrix α_{ij}. We now report the blocks for each column of MZIs for each device, where $\boldsymbol{\alpha}_i$ is the block corresponding to the i-th column on MZIs with reference to Figure 5.1. For device A:

$$\begin{aligned}
\boldsymbol{\alpha}_2 &= \begin{bmatrix} 22.243 & -6.474 & -1.079 \\ 2.651 & 22.285 & -5.506 \\ 1.017 & 3.590 & 27.412 \end{bmatrix} \frac{\Omega}{W} & \boldsymbol{\alpha}_4 &= \begin{bmatrix} 22.496 & -6.133 \\ 3.492 & 28.516 \end{bmatrix} \frac{\Omega}{W} \\
\boldsymbol{\alpha}_6 &= \begin{bmatrix} 21.904 & -6.514 & -1.117 \\ 2.474 & 23.643 & -5.757 \\ 1.001 & 3.656 & 28.347 \end{bmatrix} \frac{\Omega}{W} & \boldsymbol{\alpha}_8 &= \begin{bmatrix} 21.018 & -5.444 \\ 3.253 & 26.508 \end{bmatrix} \frac{\Omega}{W} \\
\boldsymbol{\alpha}_{10} &= \begin{bmatrix} 20.434 & -6.082 & -1.031 \\ 2.320 & 21.851 & -5.299 \\ 0.984 & 3.529 & 26.256 \end{bmatrix} \frac{\Omega}{W} & \boldsymbol{\alpha}_{12} &= \begin{bmatrix} 23.732 & -6.316 \\ 3.619 & 30.383 \end{bmatrix} \frac{\Omega}{W}.
\end{aligned} \tag{5.13}$$

For device B:

$$\begin{aligned}
\boldsymbol{\alpha}_2 &= \begin{bmatrix} 20.225 & -6.134 & -0.999 \\ 2.410 & 22.152 & -5.506 \\ 0.912 & 3.478 & 25.876 \end{bmatrix} \frac{\Omega}{W} & \boldsymbol{\alpha}_4 &= \begin{bmatrix} 18.459 & -5.077 \\ 2.873 & 23.415 \end{bmatrix} \frac{\Omega}{W} \\
\boldsymbol{\alpha}_6 &= \begin{bmatrix} 18.511 & -5.560 & -0.892 \\ 2.171 & 19.828 & -4.648 \\ 0.866 & 3.216 & 23.292 \end{bmatrix} \frac{\Omega}{W} & \boldsymbol{\alpha}_8 &= \begin{bmatrix} 18.277 & -4.962 \\ 2.821 & 23.024 \end{bmatrix} \frac{\Omega}{W} \\
\boldsymbol{\alpha}_{10} &= \begin{bmatrix} 20.417 & -6.210 & -1.031 \\ 2.375 & 22.266 & -5.236 \\ 0.949 & 3.534 & 26.175 \end{bmatrix} \frac{\Omega}{W} & \boldsymbol{\alpha}_{12} &= \begin{bmatrix} 20.601 & -5.497 \\ 3.127 & 26.118 \end{bmatrix} \frac{\Omega}{W}.
\end{aligned} \tag{5.14}$$

As can be seen from the measured values, the elements farther away from the diagonal are cut down by a multiplicative factor ranging from 20% to 30%. This means that for large blocks it is not necessary to measure all the elements of the matrix, as eventually the value becomes negligible: keeping this factor in mind, the cross-talk of the fourth nearest neighbor would be less than 1%. Therefore, the cross-talk measurement process is also scalable since the number of measurements is $O(N)$ with N number of modes.

Moreover, the elements above the diagonal always show a negative sign; this is exemplified in Figures 3.7 and 5.7: while the microheater induces a *positive* change in θ by heating up the top waveguide more than the bottom waveguide, the cross-talk due to an MZI *from below* must heat the bottom waveguide more than the top one, reversing the phase-shift difference. Hence, the tuning coefficient from MZIs physically located below is negative. It is crucial to make sure that the input laser light can always reach the first input of the designated MZI 2. If this MZI is deep inside the network, for example if it belongs to the

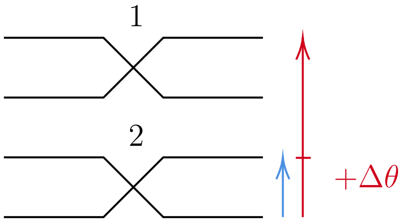

Figure 5.7: The explanation for the negative cross-talk coefficients. On the right, MZI 1 is inducing cross-talk on MZI 2; on the left, the situation is reversed. The blue (shorter) arrows represent the temperature gradient that increases $\Delta\theta$ according to Equations 3.6 and 5.2; the red (longer) arrows represent the gradient of temperature induced by the microheater. Since the cross-talk induced by the heater from below acts against the temperature gradient of increasing $\Delta\theta$, the resulting cross-talk coefficient α_{12} is negative.

first column on the right, this may not be possible without a proper setup. Thankfully, the information retrieved at the previous step - complete information about I_0 and I_π - allows us to set any MZI in the network to reflection or transmission, which means that it is always possible to route the laser light with minimal losses (up to errors in the measurement of I_0 and I_π) into any port of any MZI. In this way, we can always make sure that the laser light is entirely routed in only one port of the MZI of interest.

5.3. Calibration of External Phases

Manipulating an external phase ϕ can only induce a simple phase shift, thus external phases cannot be calibrated with a direct approach as we have done for the internal phases since we exclusively measure the optical power output of the device. It is therefore necessary to estimate the effect of an external phase by measuring some interference effect.

To measure a chosen external phase ϕ_i we then create a "virtual" MZI around it, as shown in Figure 5.8; we refer to this as an *interferometric loop*. We take the two MZIs nearest (horizontally) to the external phase of interest and set their θ to $\pi/2$. In this way, power is evenly split between the outputs; the matrix that describes the two MZIs then becomes

$$M = \frac{e^{i\frac{3\pi}{4}}}{\sqrt{2}} \begin{bmatrix} 1 & 1 \\ 1 & -1 \end{bmatrix}. \tag{5.15}$$

All the other MZIs are instead set to their reflection point ($\theta = \pi$). From a matrix multiplication of all the involved devices we can calculate the matrix that describes this

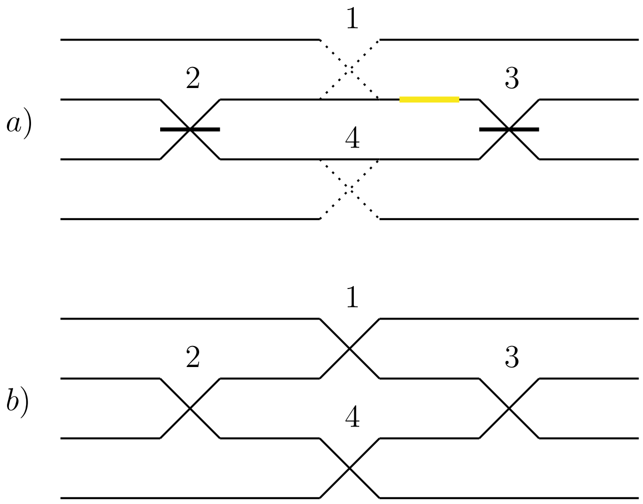

Figure 5.8: The "virtual" MZI created using an arrangement of four MZIs. a) The arrangement. The dotted crossings represent MZIs that have been set to the reflection point, effectively creating a bridge to the next straight waveguide. The crossings with a thick bar represent MZIs that have been set to the $\theta = \pi/2$ point. The thick yellow line represents the microheater of MZI 3, which is the microheater that determines the parameter ϕ of Equation 5.16. b) The topology of the arrangement shown without any features.

configuration:

$$V = e^{i\frac{\phi}{2}} \begin{bmatrix} -i\cos\left(\frac{\phi}{2}\right) & \sin\left(\frac{\phi}{2}\right) \\ \sin\left(\frac{\phi}{2}\right) & -i\cos\left(\frac{\phi}{2}\right) \end{bmatrix}. \tag{5.16}$$

We can treat this interferometric loop as an actual MZI within the circuit. Again we adopt an affine linear model for ϕ like Equation 5.3; hence, from the matrix representation and this model we obtain the transmission and reflection functions

$$\mathcal{T} = \sin^2\left(\frac{\phi_0 + \alpha Q}{2}\right), \quad \mathcal{R} = \cos^2\left(\frac{\phi_0 + \alpha Q}{2}\right). \tag{5.17}$$

Which we may calibrate the same way we have done in the previous section: we send a current ramp to the phase under scrutiny ϕ and fit the curve using the appropriate target function

$$f(Q) = A\sin^2\left(\frac{\phi_0 + \alpha Q}{2}\right).$$

We remark that it is necessary to route the light into the top input port of the virtual MZI (in the case such MZI is located deep inside the network) as well as correctly drive the output of the MZI all the way to the output ports. Therefore, by this point it is necessary to know how to set multiple adjacent MZIs to their reflection or transmission

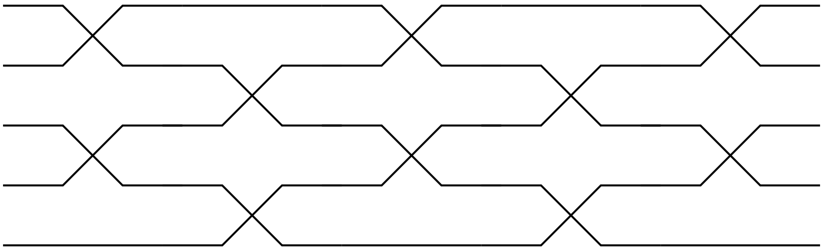

Figure 5.9: A 5-by-5 network bare of any labels. Every crossing corresponds to an MZI.

points. This amounts to solving the cross-talk problem detailed in Section 5.2.1, which we explain how to do in the next Chapter.

5.3.1. Measurable Static Phases and Equivalent Circuits

The algorithm just outlined for the calibration of the external phases has a limit in that it cannot be used to obtain the static phase ϕ_0 for every MZI in the network. In fact, with reference to Figure 5.1, there is no way to close an interferometric loop around the external phases $\phi_1, \phi_4, \phi_{11}, \phi_5$, and ϕ_{12} the same way we have done so far. The first three phases are the least of our concern; since we operate with one input at a time, they act as global phases and thus all of our results are completely invariant with respect to them. These phases would only matter if we were to enter the device with a pair of coherent light signals at two different inputs.

ϕ_5, and ϕ_{12}, however, present an actual problem. First and foremost, we need to find a different way to measure α for these specific phases; fortunately, closing an interferometric loop around them by using MZI 1, MZI 6 (for ϕ_5) and MZI 4, MZI 13 (for ϕ_{12}) is sufficient to determine α. Using these interferometric loops, however, we cannot retrieve the value of the static external phase of MZI 5 and 12, since these values are tied to the loop.

This could seem to be problem, however we now show that it is possible to assume $\phi_{0,5} = \phi_{0,12} = 0$ and carry on without impacting our future calculations.

Consider the 5-mode UPP network of Figure 5.9. As shown at the top of Figure 5.10, we can consider adding the same phase shift at the input of an MZI in the network. Since it amounts to multiplying the input state of the MZI by a global phase, we obtain that the output state is multiplied by the same global phase; if we now remove this global phase at the output of the MZI, then, the circuit becomes equivalent to the one in Figure 5.9.

This may seem uninteresting at first, however this equivalence can be exploited to achieve interesting results. In fact, it is easy to see that the same can be done with multiple MZIs: by enclosing more than one MZI we can obtain many different equivalent circuits

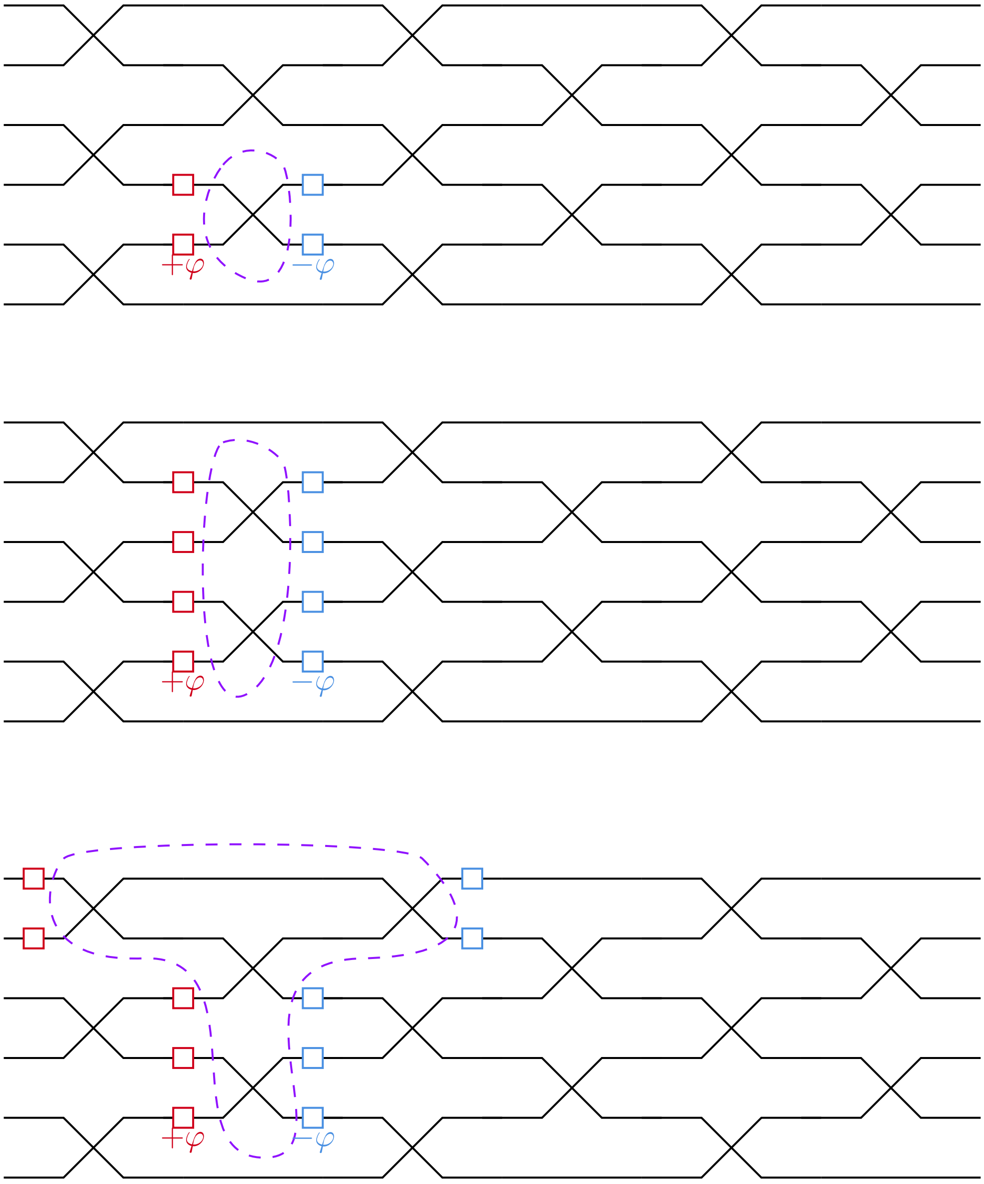

Figure 5.10: Construction of equivalent circuits. In the three figures, the red squares (always on the left) signify the addition of a phase φ on that waveguide, while the blue squares (always on the right) signify the subtraction by a phase φ. The dashed shape can enclose any number of MZIs. In this Figure we report three examples of circuits equivalent to the 6-mode UPP.

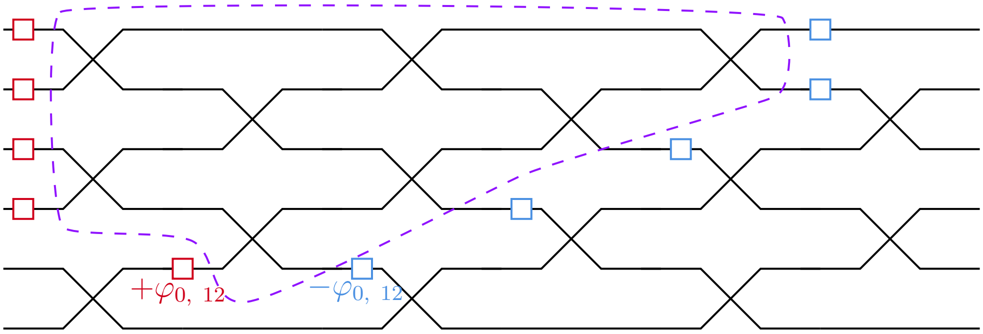

Figure 5.11: A convenient equivalent circuit for the 6-mode UPP. We choose to add the unknown static phase on one side, and on the other side we interpret all results as having already subtracted this phase every time we calculate the static phase belonging to different loops.

as shown in Figure 5.10. Most importantly, for the purposes of our work, it is not possible to measure the phase of the field at the output of the UPP; this means that if in this way we were to add or subtract phases directly at the input or output ports of the device, those phases effectively would cease to have any effect.

This means that it is possible to manipulate the phases in the circuit to our convenience in some cases even if they are unknown. For example, the circuit shown in Figure 5.11 is equivalent to the basic, bare 6-mode UPP. However, even if $\phi_{0,12}$ was unknown in the basic circuit, in the equivalent circuit the phase difference between the two arms of MZI 12 is equal to zero.

This comes at the downside of having to subtract this unknown phase $\phi_{0,12}$ in other places in the network. Fortunately, this is not an issue: the static phases for all the MZIs in front of MZI 12 have already been measured; therefore, when we consider the equivalent circuit, we can interpret those measurements as giving us not the static phases proper, but simply the static phases *subtracted by* $\phi_{0,12}$.

Remarkably, then, this changes nothing about how the circuit operates: all we have to do is reinterpret the data collected so far as being given by an equivalent albeit slightly different circuit. This can be done for both MZI 5 and MZI 12, hence they may both be assumed to be zero under the conditions above.

5.3.2. Cross-Talk of External Phases

In a similar vein with respect to Section 5.2.1, the external phases show the effects of thermal cross-talk in the exact same way as the internal phases do. As before, then, the

MZI	α $[\Omega/mW]$	ϕ_0	I_π $[mA]$	I_0 $[mA]$
2	27.741	1.436	7.760	12.850
3	27.048	4.122	13.470	8.781
5	29.681	0	12.976	6.238
6	21.904	0.837	8.683	13.107
7	21.548	3.746	14.769	10.122
8	22.421	2.521	5.184	12.445
9	26.516	1.163	8.525	13.457
10	28.347	3.821	13.508	9.149
12	22.856	0	13.108	5.817
13	23.643	3.632	15.357	10.633
14	19.931	4.232	14.878	9.583
15	20.969	4.065	15.564	10.301

Table 5.3: The data measured for device A using the procedure detailed in this section, for external phase shifters only. The numbering of the MZIs follows Figure 5.1. The values I_π and I_0 in this context are the currents needed to set the interfermetric loop centered around the microheater to reflection and transmission respectively.

"true" model becomes:

$$\phi_i = \phi_{i0} + \sum_{j=0}^{N} \alpha_{ij} Q_j. \tag{5.18}$$

The measurement of the off-diagonal coefficients of the matrix is done similarly. We first construct the virtual MZI around the external phase of interest (i.e. setting the two horizontal neighboring internal phases to $\theta = \pi/2$ and the vertical neighboring internal phases to the reflection point), then we set $\phi = \pi/2$. This has the effect of splitting the power evenly on the two outputs of the virtual MZI, on which we can now make a normalised measurement.

We send a current ramp on one other external phase and perform the normalised measurement, fitting the curve with the same exact method described in Section 5.2.1. This allows us to retrieve the entire matrix, and again thanks to the design of the circuit we may assume the matrix is block diagonal; we report each block here.

$$\boldsymbol{\alpha}_3 = \begin{bmatrix} 29.681 & -2.600 \\ 6.427 & 22.856 \end{bmatrix} \frac{\Omega}{W} \qquad \boldsymbol{\alpha}_5 = \begin{bmatrix} 21.904 & -6.514 & -1.117 \\ 2.474 & 23.643 & -5.757 \\ 1.001 & 3.656 & 28.347 \end{bmatrix} \frac{\Omega}{W}$$

$$\boldsymbol{\alpha}_7 = \begin{bmatrix} 19.931 & -5.675 \\ 2.968 & 26.516 \end{bmatrix} \frac{\Omega}{W} \qquad \boldsymbol{\alpha}_9 = \begin{bmatrix} 20.969 & -6.388 & -1.088 \\ 2.376 & 22.421 & -5.502 \\ 0.940 & 3.450 & 27.048 \end{bmatrix} \frac{\Omega}{W} \tag{5.19}$$

$$\boldsymbol{\alpha}_{11} = \begin{bmatrix} 21.548 & -5.888 \\ 3.178 & 27.741 \end{bmatrix} \frac{\Omega}{W}.$$

Cross-talk experiments on the external phases were only performed on device A. Note that the numbers are very similar with respect to the internal phases case; this is ideal, since it is evidence that the numbers do not depend on whether we are measuring internal or external phases and on which device we are doing so, but they only depend on the thermal cross-talk problem at hand.

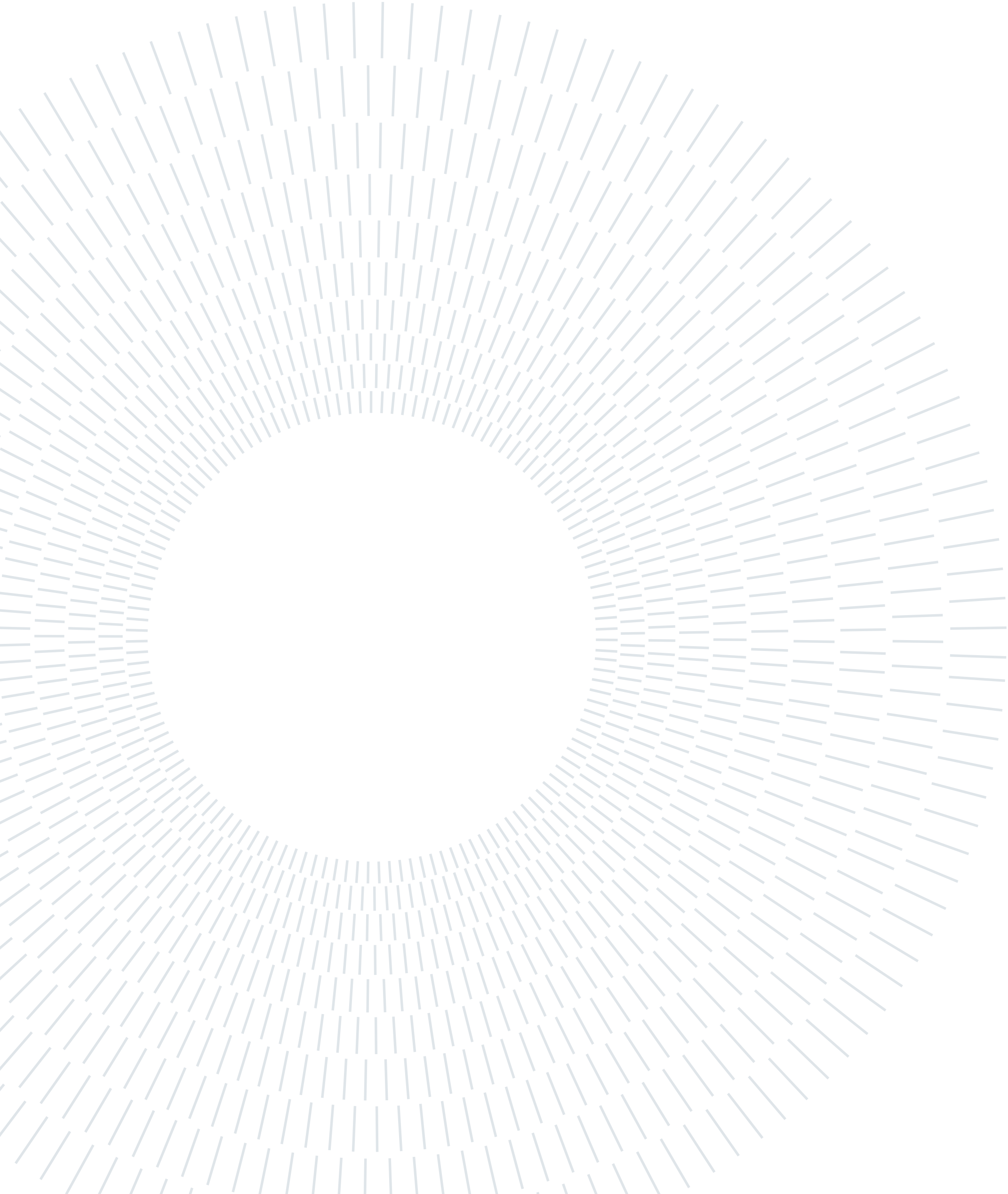

6 Operation of the 6-mode UPP

6.1. Operating the Device without Clements' Algorithm

So far we have discussed how to calibrate the behavior of each phase shifter in the network of a general N-mode UPP. We have included details on the assumptions used, and on the techniques employed to take into account nonlinearity and non-measurable static phases. At this point, it is indeed already possible to operate an UPP. In fact, at the end of the process detailed in the previous chapter, the relation that binds the phases and the currents on the microheaters is known. Therefore, it is already possible to use the UPP for various applications, for example *routing*: taking an input signal and routing it to any of the output ports. This operation can be done by inspecting the network visually and by determining which MZIs need to be put to the reflection or transmission points to route the input signal to the correct output port. In other words, we determine the full vector of $(\boldsymbol{\theta}, \boldsymbol{\phi}) = \boldsymbol{\varphi}$, where $\boldsymbol{\theta}$ and $\boldsymbol{\phi}$ are the arrays of internal and external phases for each of the MZIs in the network respectively.

On the contrary, in case one aims to implement a specific unitary matrix U, an extra step is necessary. In fact, a procedure is required to obtain the vector $\boldsymbol{\varphi}$ starting from the target unitary matrix U; this procedure is precisely Clements' algorithm as described in Section 2.2.4. In short, Clements' algorithm decomposes the target unitary U into a multiplication of elementary matrices, each of which corresponds to an MZI of the network of the UPP. From this we can extract the internal and external phases that the MZIs need to have in order to implement the target unitary.

At the end of either process, be it Clements' algorithm or inspection, the result is the vector $\boldsymbol{\varphi}$; in the next section we explain how to use this vector to retrieve the currents for each microheater.

6.1.1. Existence of Solutions

Finding the set of currents I_j that implements the desired unitary matrix once the full vector $\boldsymbol{\varphi}$ has been calculated is only a matter of applying Equations 5.10 and 5.7. In terms of the vector $\boldsymbol{\varphi}$ and the vector of adjusted current squares $\mathbf{Q}$, we can write

$$\boldsymbol{\varphi} = \boldsymbol{\alpha}\mathbf{Q} + \boldsymbol{\varphi}_0 \tag{6.1}$$

where $\boldsymbol{\varphi}_0$ represents the array of all static phases, $\boldsymbol{\alpha}$ is the tuning matrix. Finding the unknown $\mathbf{Q}$, however, is not as simple as inverting the linear relation between phase and power.

In fact, while inverting a matrix is quite easy from a computational point of view, there is no guarantee that the vector resulting from

$$\mathbf{Q} = (\boldsymbol{\alpha})^{-1}(\boldsymbol{\varphi} - \boldsymbol{\varphi}_0). \tag{6.2}$$

actually has all positive entries. Indeed, in order for our solution to be physically meaningful, there cannot be negative square currents, lest such currents would be imaginary. Hence, the problem becomes:

$$\begin{aligned} &\text{solve} \quad \boldsymbol{\alpha}\mathbf{Q} = \boldsymbol{\varphi} - \boldsymbol{\varphi}_0 \\ &\text{subject to} \quad Q_i \geq 0 \quad \forall i. \end{aligned} \tag{6.3}$$

A basic result in linear algebra says that if the rank of the matrix $\boldsymbol{\alpha}$ is full, then the solution given by Equation (6.2) is unique. This means that for some $\boldsymbol{\varphi}$ there may not be any solution for the system (6.3), as there is no guarantee that the resulting entries of the vector $\mathbf{Q}$ are all nonnegative. However, we can leverage the fact that for us

$$\theta \mapsto \theta + 2\pi, \quad \phi \mapsto \phi + 2\pi \tag{6.4}$$

is actually a symmetry transformation, since the behavior of an MZI is periodic (Equation 2.18). In this way, we may adjust the vector φ by adding or removing multiples of 2π in such a way that we can ensure the existence of solutions.

In theory, with this setup there would be infinitely many solutions. However, since we also want to minimise energy costs for the operation of UPPs, it is appropriate to look for the minimum-total-power solution of the system. Therefore, since every element Q_i of the current squares vector is connected to the power dissipated on the i-th microheater, the problem becomes the following:

$$\begin{aligned}
&\text{minimize} \quad \sum_i Q_i \\
&\text{subject to} \quad Q_i \geq 0 \quad \forall i \quad \text{and} \quad \boldsymbol{\alpha}\mathbf{Q} + 2\pi\mathbf{n} = \boldsymbol{\varphi} - \boldsymbol{\varphi}_0.
\end{aligned} \tag{6.5}$$

Where **n** is now a vector of integers of the appropriate dimensions. The problem now mixes integer variables and real variables, making it a *Mixed Integer Linear Programming* (MILP) problem. Finding the solution to this problem requires substantially more computational power since MILP is an NP-hard problem [57]. In this work, we chose to solve it using the GEKKO solver library for Python.

After this step, we can proceed to the inversion of Equation 5.7 in order to find the correct set of currents that implement the required unitary matrix.

6.2. Results of the Experiments

In this section we discuss the results obtained by applying the theory up to this point to implement specific unitary matrices. In particular, the experiments have been performed on two chips - named A and B respectively - whose calibration has been performed using laser sources at 793nm and 785nm respectively.

The results are organised into two large groups. *Switching matrices* are unitary matrices whose entries are either 0 or 1; they have been chosen as a good subset of unitary matrices to pay attention to as they are the only subset that can be explored entirely by manipulating the internal phases alone. Thus, they offer a good benchmark to understand if the calibration and operation of the internal phases has been done correctly. The set of all switching matrices is the set of all those matrices obtained by permuting rows or coloumns of the identity I. *Random Haar matrices* are general unitary matrices, whose entries may be any complex number inside the unit circle in $\mathbb{C}$; the probability distribution associated to random Haar matrices is uniform over $U(N)$, hence picking a Haar matrix means sampling from the whole space of unitary matrices uniformly at random. Since these matrices use both external and internal phases, they offer the ultimate benchmark for the operation of an UPP.

The measurements have been performed as follows: we pick a set of unitary matrices $\mathbf{U}^{(n)}$, and we store on a file the currents obtained by running Clements' algorithm. Then, we couple the light from the laser source (Section 4.2) into the first input; we apply the currents corresponding to the first matrix $\mathbf{U}^{(1)}$, and using the automated stages (Section 4.4) we move the output objective and make a normalised measurement of the light from each output. This allows us to measure the value of $\left|\mathbf{U}_{i1}^{(1)}\right|$ for all i. Then, the currents for the next matrix are loaded and applied, without changing the input, until all matrices in the set have been applied once.

By the end of this step, we have measured $\left|\mathbf{U}_{i1}^{(n)}\right|$ for all n and i. Then, we manually change the input and repeat the process, for example changing it to the second input port; this will measure $\left|\mathbf{U}_{i2}^{(n)}\right|$ for all n and i. Repeating for every input will yield a complete measurement of every matrix in the set.

When this process is done, the performance of the UPP is calculated by evaluating the *fidelity* as defined in 2.21:

$$\bar{\mathcal{F}}(\mathbf{U}, \mathbf{U}_T) = \frac{1}{N} \operatorname{Tr}\left\{|\mathbf{U}^\dagger||\mathbf{U}_T|\right\}.$$

where $\mathbf{U}$ is the measured matrix and $\mathbf{U}_T$ is the target matrix. We take the absolute value of each entry of the matrices and calculate their dot product. Hence, this fidelity is a measure of how similar two matrices are, where a value of 1 means the two matrices are identical up to a phase term for every entry.

6.2.1. Switching Matrices

For both devices, 21 matrices have been chosen as a test. These are split into three categories: *Pauli X matrices*, *Port Switching* matrices and *Random Switching* matrices. The Pauli X matrices are:

$$\text{Pauli} = \{I, X, X^2, X^3, X^4, X^5\} \quad \text{with}$$

$$\begin{gathered} I = \begin{bmatrix} 1 & 0 & 0 & 0 & 0 & 0 \\ 0 & 1 & 0 & 0 & 0 & 0 \\ 0 & 0 & 1 & 0 & 0 & 0 \\ 0 & 0 & 0 & 1 & 0 & 0 \\ 0 & 0 & 0 & 0 & 1 & 0 \\ 0 & 0 & 0 & 0 & 0 & 1 \end{bmatrix} \\ X = \begin{bmatrix} 0 & 0 & 0 & 0 & 0 & 1 \\ 1 & 0 & 0 & 0 & 0 & 0 \\ 0 & 1 & 0 & 0 & 0 & 0 \\ 0 & 0 & 1 & 0 & 0 & 0 \\ 0 & 0 & 0 & 1 & 0 & 0 \\ 0 & 0 & 0 & 0 & 1 & 0 \end{bmatrix}. \end{gathered} \tag{6.6}$$

The chosen Port Switching matrices are six matrices that swap the second input port with one of the other five output ports. Finally, the Random Switching matrices are 10 matrices uniformly sampled from the set of all possible switching matrices - making sure that we do not sample from those that also belong to the Pauli and Port Switching sets already, so all 21 matrices are different.

In Figure 6.1 we showcase some results. The graphs are a visual representation of the matrix entries; the entries with the highest values indeed correspond to entries that have a 1 on the target matrices. For the entries that have a 0 on the target matrices we find a nonzero value on the measured entries; on average their value is about 10^{-2}. The fact that we have a nonzero measured value on entries that we expect to be zero is to be traced back to background noise as well as imperfections in the implementation of the matrices. In Table 6.1 we report the average fidelity for each matrix set. The averages are all above 99%, which is higher in each category taken separately than the state-of-the-art in FLM-written UPPs [10].

Matrix Set	$\overline{\mathcal{F}_A}$	$\overline{\mathcal{F}_B}$
Pauli	0.99538 ± 0.00196	0.99669 ± 0.00053
Port Switching	0.99709 ± 0.00066	0.99695 ± 0.00050
Random	0.99363 ± 0.00101	0.99673 ± 0.00051
Total	0.99537 ± 0.00077	0.99679 ± 0.00030

Table 6.1: The fidelities measured on the three different sets of switching matrices. The data reported here is given by the average fidelity of the set plus or minus the standard deviation over the set.

6.2.2. Random Haar Matrices

Random Haar matrices were implemented and measured only using device A. In total, we implemented 57 Haar matrices. The average fidelity on this random set was 0.89076 ± 0.04660. The distribution (shown in Figure 6.2) is uniform across the range $[0.84, 0.96]$, with a few matrices giving an even lower fidelity. However, by inspecting the matrix elements, as evidenced in Figure 6.3, it is possible to see that there is little correlation between the elements of the target matrix and the elements of the measured matrix even in the case of high fidelity. This is the telltale sign that even if fidelities can reach values as high as 0.95, they still do not represent a truly well-implemented matrix as an obvious divergence can be seen. No matrix element in particular seemed to be majorly responsible for this divergence, rather the error between the target matrix and the measured matrix was evenly distributed on all 36 entries.

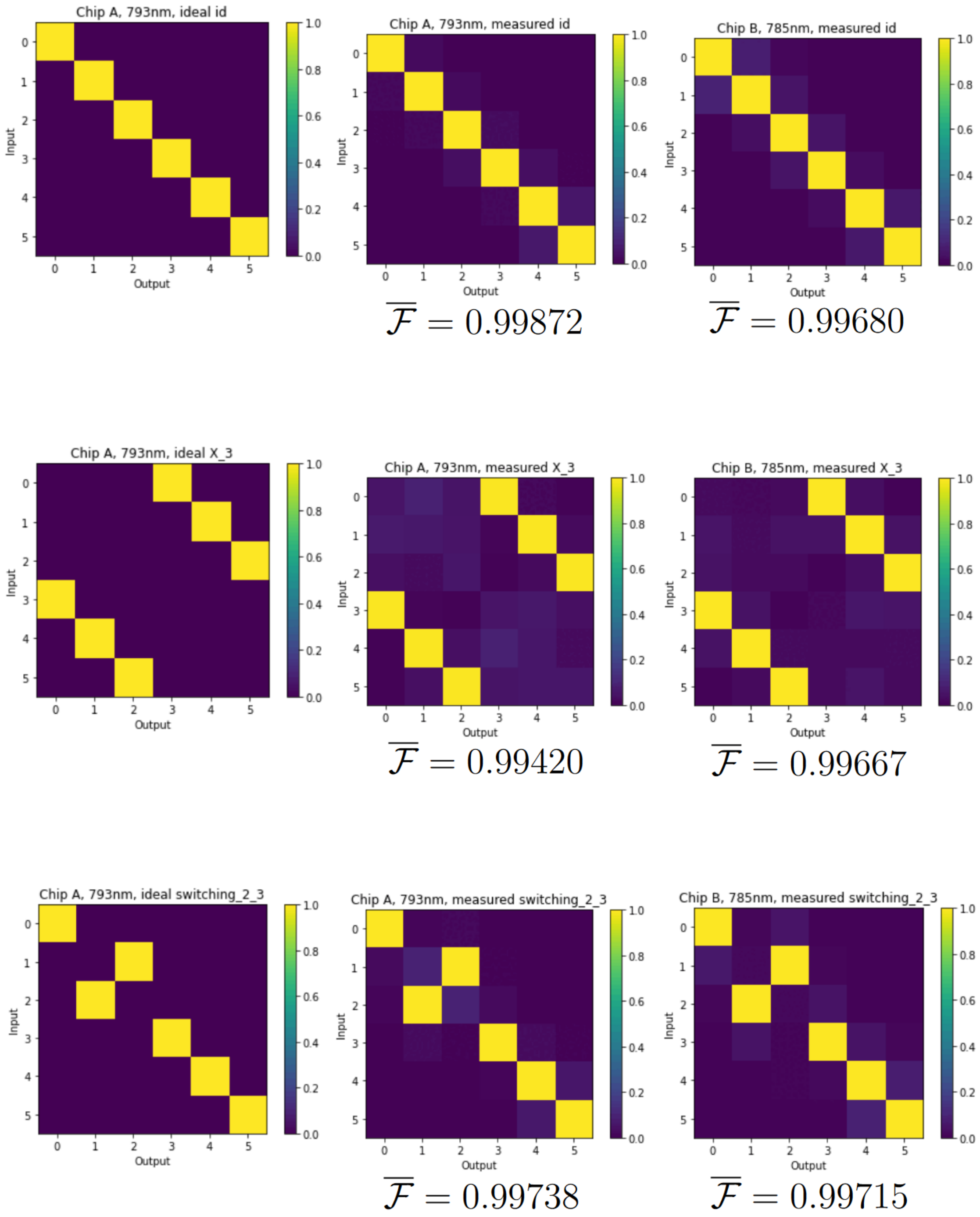

Figure 6.1: Three examples taken from the results of the Switching set; the first coloumn shows the ideal target matrix, the second and third show the measurements on device A and B respectively. The first matrix is the identity, the second matrix is the Pauli X^3, the third matrix swaps inputs 2 and 3. In these graphs the numbering of the inputs and outputs is initialised to 0 rather than 1.

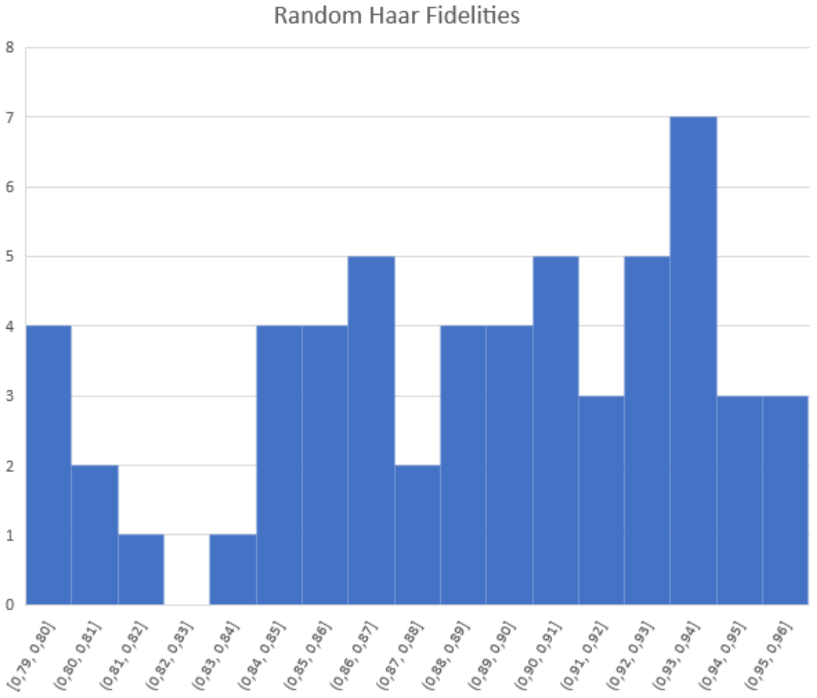

Figure 6.2: The histogram of the fidelities obtained from the 57 measurements. The distribution is roughly uniform across a large range centered around the mean, with a small set of matrices responsible for dragging the average down even further.

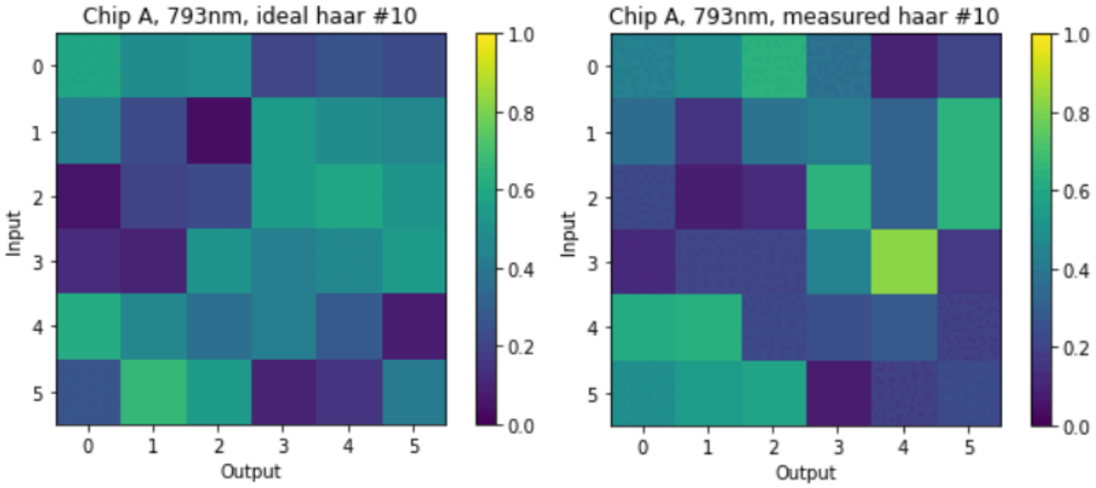

Figure 6.3: An example of Haar random matrix obtained with device A; the target matrix is on the left, while the measured matrix is on the right. This matrix was implemented with a fidelity of 0.953. The measured matrix and the target matrix are clearly different.

Comparing this with the performance on the Switching set gives hope that the chip has the potential to achieve comparable fidelities to that set, all that matters is to find a better way to operate it. Moreover, the sharp drop in fidelity when dealing with Random Haar matrices, which differ by switching matrices primarily because they employ external phases in addition to internal ones, suggests that the main cause of poor performance is to be traced back to poor control of the external phases. Thus, we had to develop a way to control the external phases better by going back to the assumptions used by Clements' algorithm and improving on it.

6.3. Common Mode Phase

One problem behind the poor performance of the random Haar matrices can be traced back to the very model that has been used to decompose the original unitary matrix in Clements' algorithm. In fact, while the model used in Clements algorithm is

$$A(\theta,\phi) = \begin{bmatrix} e^{i\phi}\cos\theta & -\sin\theta \\ e^{i\phi}\sin\theta & \cos\theta \end{bmatrix}$$

the model we derived in Chapter 2 of an MZI is

$$M(\theta,\phi) = e^{i\left(\frac{\theta}{2}+\frac{\pi}{2}\right)} \begin{bmatrix} e^{i\phi}\sin\left(\frac{\theta}{2}\right) & \cos\left(\frac{\theta}{2}\right) \\ e^{i\phi}\cos\left(\frac{\theta}{2}\right) & -\sin\left(\frac{\theta}{2}\right) \end{bmatrix}.$$

While the two models differ qualitatively by the entries of the matrices, there is also another important element that the first does not address: the *common mode phase* $e^{i\left(\frac{\theta}{2}+\frac{\pi}{2}\right)}$.

In general, if we are dealing with an isolated MZI the effect of the common mode can be disregarded. This is because we are typically interested in the splitting ratio of optical power, which is independent with respect to a global phase of the propagating field. However, in a network even as small as a 3-mode (Figure 6.4) the effect of a common mode phase can be felt if it comes from the MZI in the middle of the network.

Hence, we need to refine the model and make sure we can include the effect of the common mode phase. Considering the network of Figure 6.5, we see that the MZIs 1 and 4 contribute in a similar way on opposite sides. Both of these common mode phases affect the external phase ϕ_3 of MZI 3, but while $\phi_{c,1}$ will contribute positively to the differential phase shift between the arms, $\phi_{c,4}$ will contribute negatively.

Since the contribution of $\phi_{c,1}$ is positive, we have to remove it from the phase calculated by Clements' algorithm; likewise, we have to add $\phi_{c,4}$. In other words, we need to modify

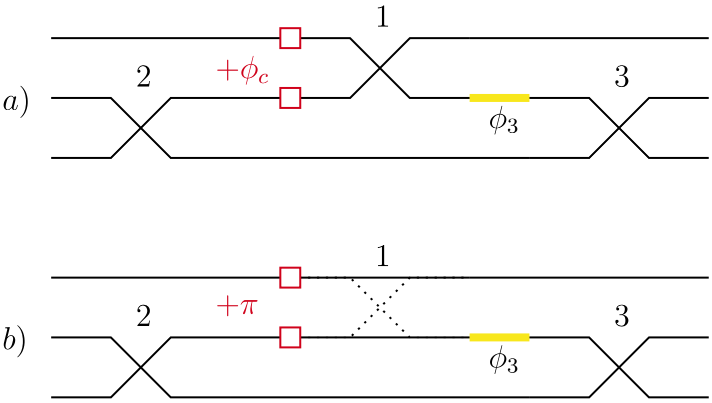

Figure 6.4: The diagram of a 3-mode network with an added common mode phase. The external phase shifter related to MZI 3 is highlighted by the thick yellow line. a) The network where the internal phase of MZI 1 is not set to any specific value. MZI 1 then adds some common mode phase, which acts as an extra phase on the middle waveguide. b) The case when MZI 1 is set to the reflection point ($\theta_1 = \pi$), represented by dotted lines and bridges between straight waveguides. Since the common mode phase is $\theta_1/2+\pi/2$, the field on the middle waveguide picks up an extra π phase. If this phase was not accounted for, the field would only pick up the phase due to the propagation in the straight waveguide.

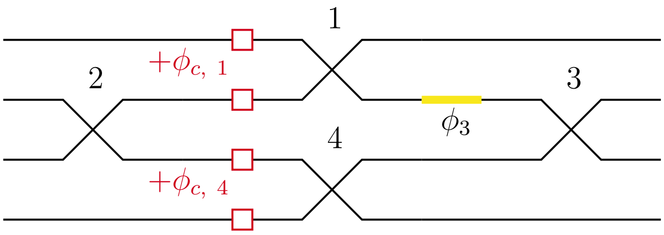

Figure 6.5: The diagram of a 4-mode network, with the external phase shift ϕ_3 highlighted in yellow. The effects of a common mode phase from the MZIs 1 and 4 are highlighted here; effectively, they contribute with their common mode phase to ϕ_3 with opposite signs.

the external phase obtained from Clements' algorithm as follows:

$$\phi_3' = \phi_3 - \frac{\theta_1}{2} + \frac{\theta_4}{2}. \tag{6.7}$$

ϕ_3' is the phase shift we need to set on the external microheater of MZI 3. Note that the constant terms have canceled out. In the case of the network shown in Figure 6.4, however, since the common phase contribution comes only from MZI 1, the constant does not cancel out and we have:

$$\phi_3' = \phi_3 - \frac{\theta_1}{2} - \frac{\pi}{2}. \tag{6.8}$$

Therefore, Clements' algorithm can still be applied as long as we use the correct transformation to account for the effect of the common mode phase on every ϕ_i. For the 6-mode UPP under scrutiny, this transformation is described by:

$$\begin{array}{lll}
\phi_1' = \phi_1 & \phi_6' = \phi_6 + \frac{\theta_5}{2} + \frac{\pi}{2} & \phi_{11}' = \phi_{11} \\
\phi_2' = \phi_2 - \frac{\theta_8}{2} + \frac{\theta_3}{2} & \phi_7' = \phi_7 - \frac{\theta_{15}}{2} + \frac{\theta_8}{2} & \phi_{12}' = \phi_{12} \\
\phi_3' = \phi_3 - \frac{\theta_9}{2} - \frac{\pi}{2} & \phi_8' = \phi_8 - \frac{\theta_{14}}{2} + \frac{\theta_9}{2} & \phi_{13}' = \phi_{13} - \frac{\theta_5}{2} + \frac{\theta_{12}}{2} \\
\phi_4' = \phi_4 & \phi_9' = \phi_9 - \frac{\theta_{13}}{2} + \frac{\theta_{10}}{2} & \phi_{14}' = \phi_{14} - \frac{\theta_6}{2} + \frac{\theta_{13}}{2} \\
\phi_5' = \phi_5 & \phi_{10}' = \phi_{10} - \frac{\phi_{12}}{2} - \frac{\pi}{2} & \phi_{15}' = \phi_{15} + \frac{\theta_{14}}{2} + \frac{\pi}{2}
\end{array}$$

where the numbering of the MZIs is done with reference to Figure 5.1. No transformation is required for the internal phases θ_i.

6.3.1. Thermal Cross-talk and Common Mode Phase

Going beyond the common mode phase of an ideal MZI, we looked at the physical effects that may influence the common mode phase in the 6-mode UPP. In the following, we describe how thermal cross-talk can affect the analysis of the common mode phase and we present a method we developed to measure such effect.

n fact the resistive microheater of a reconfigurable MZI heats up *both* waveguides. Even though we have only so far considered the differential as the relevant quantity for the purposes of phase shifting, we must consider that the heating of the waveguides induces what is effectively a common mode phase through thermo-optic effect.

Because of this effect we may alter our model for an MZI:

$$M(\theta,\phi) = e^{i\gamma\phi}e^{i\left(\left(\frac{1}{2}+\beta\right)\theta+\frac{\pi}{2}\right)}\begin{bmatrix} e^{i\phi}\sin\left(\frac{\theta}{2}\right) & \cos\left(\frac{\theta}{2}\right) \\ e^{i\phi}\cos\left(\frac{\theta}{2}\right) & -\sin\left(\frac{\theta}{2}\right)\end{bmatrix}. \tag{6.9}$$

In this refined model, β and γ are new cross-talk coefficients, which should be measured in order to fully calibrate the action of an MZI. This substantially alters the transformation described in the last section, as the common mode phase depends on both θ and ϕ. In order to retrieve the correct transformation, we need to operate the substitution:

$$\frac{\theta_i}{2} \mapsto \left(\frac{1}{2}+\beta\right)\theta_i + \gamma\phi_i. \tag{6.10}$$

Calibrating the effect of the thermal cross-talk on the common mode phase is therefore crucial to obtain a correct model of the operation of each MZI. We now describe a method to measure the coefficients β and γ.

Consider the network of Figure 6.4 again. We couple the light into the middle input, and we initially set the three MZIs as follows: MZI 2 and 3 are set to $\theta = \pi/2$, so that the optical power is split between the second and third waveguide, while their external phases ϕ_2, ϕ_3 stay untouched. Then, MZI 1 is set to an arbitrary θ_1 close to π (therefore, near the reflection point but not necessarily equal to it). With this setup, some of the optical power spills over to the first waveguide, while the rest can interfere with itself within MZI 3. Therefore, the field E at the two inputs of MZI 3 is of the form:

$$E = \frac{E_0}{\sqrt{2}}\begin{bmatrix} r\cdot e^{\left(\frac{1}{2}+\beta\right)\theta_1} \\ 1\end{bmatrix}. \tag{6.11}$$

Note that we have neglected any other phase that does not depend on θ_1 for the moment; the first entry of the vector corresponds to the top input of MZI 3, the second entry to the bottom input. The parameter r is the amplitude reflectivity of MZI 1, namely $|r|^2 = \mathcal{R}(\theta_1)$ which is the reflection function. At this point, the field is fed into MZI 3 and undergoes interference. At the output, we have:

$$E_{\text{out}} = \frac{E_0}{2}\begin{bmatrix} r\cdot e^{\left(\frac{1}{2}+\beta\right)\theta_1}+1 \\ r\cdot e^{\left(\frac{1}{2}+\beta\right)\theta_1}-1\end{bmatrix}. \tag{6.12}$$

As a function of θ_1, the power at the bar port of MZI 3 can be calculated as:

$$P_{\text{bar}} = P\frac{1+r^2+2r\cos\left(\left(\frac{1}{2}+\beta\right)\theta_1\right)}{4} \tag{6.13}$$

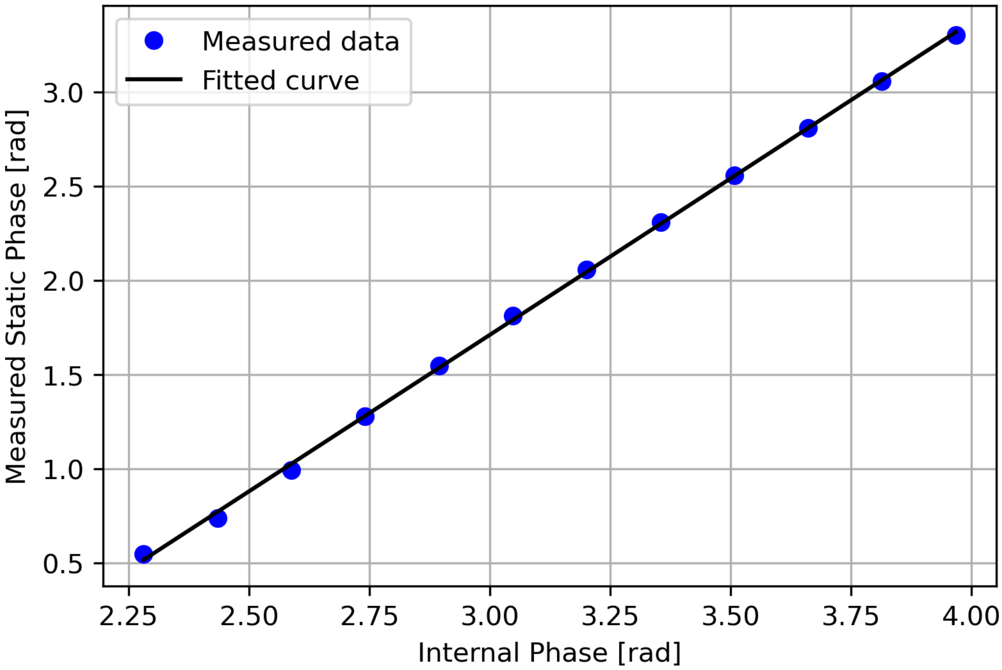

Figure 6.6: The linear graph extracted from the method described in this section. We see clearly that the linear coefficient is larger than 0.5, indicating that the cross-talk has a substantial impact on the common mode phase.

with $P = \frac{1}{2}\varepsilon c|E_0|^2$ input power. We can normalize by the input power of MZI 3 ($P_{\text{in } 3} = P/2 + r^2 P/2$) to obtain:

$$\mathcal{P} = \frac{1}{2} + \frac{r}{r^2+1}\cos\left(\left(\frac{1}{2}+\beta\right)\theta_1\right). \tag{6.14}$$

A similar calculation shows that if we were to add the effect of an external phase ϕ_3 to this model (from MZI 3), we would obtain:

$$f(\phi_3) = \frac{1}{2} + \frac{r}{r^2+1}\cos\left(\left(\frac{1}{2}+\beta\right)\theta_1 + \phi_3\right). \tag{6.15}$$

In terms of adjusted current square, we have:

$$f(Q) = \frac{1}{2} + \frac{r}{r^2+1}\cos\left(\left(\frac{1}{2}+\beta\right)\theta_1 + \phi_{03} + \alpha_{33}Q\right). \tag{6.16}$$

We now describe how to set up the experiment. We can simply send a current ramp on MZI 3, make a normalised measurement of its output, and perform a curve fit with 6.16 as our target curve. With the curve fit we can retrieve the value of $\left(\frac{1}{2}+\beta\right)\theta_1 + \phi_{03}$.

At this point, we can repeat the measurement choosing a different θ_1, which therefore will give a new value of $\left(\frac{1}{2}+\beta\right)\theta_1+\phi_{03}$. We can do this multiple times, exploring different values of θ_1 across a range. At the end of this process, we can plot the measured values against θ_1: what we see is a linear graph (Figure 6.6).
The graph has an intercept equal to ϕ_{03}, and its slope determines the coefficient that multiplies θ_1: if this slope is larger than 0.5, then $\beta > 0$. The process to measure γ is almost the same: it is not necessary to vary θ_1, which can be kept at $\theta_1 = \pi$, i.e. the reflection point. Sending a current ramp to ϕ_1 and extrapolating a linear graph is sufficient to determine the value of γ.

Due to time constraints, only one measurement was performed on the 6-mode UPP to determine the value of β. The value of β for MZI 15 was determined using the 3-mode3 subnetwork consisting of MZI 15, 7, and 14. All other MZIs during the experiment were set to their reflection point, and light was routed into the top input of MZI 14.
In this experiment, a value of $\beta = 0.17$ was found; this implies that the contribution of thermal cross-talk to the common mode phase is about 34% in air, which is perfectly consistent with the findings on thermal cross-talk between adjacent MZIs (Section 5.2.1). This contribution cannot be neglected in operating the device.
Also due to time constraints, no matrices have been implemented with a modified algorithm taking into account the β and γ coefficients.

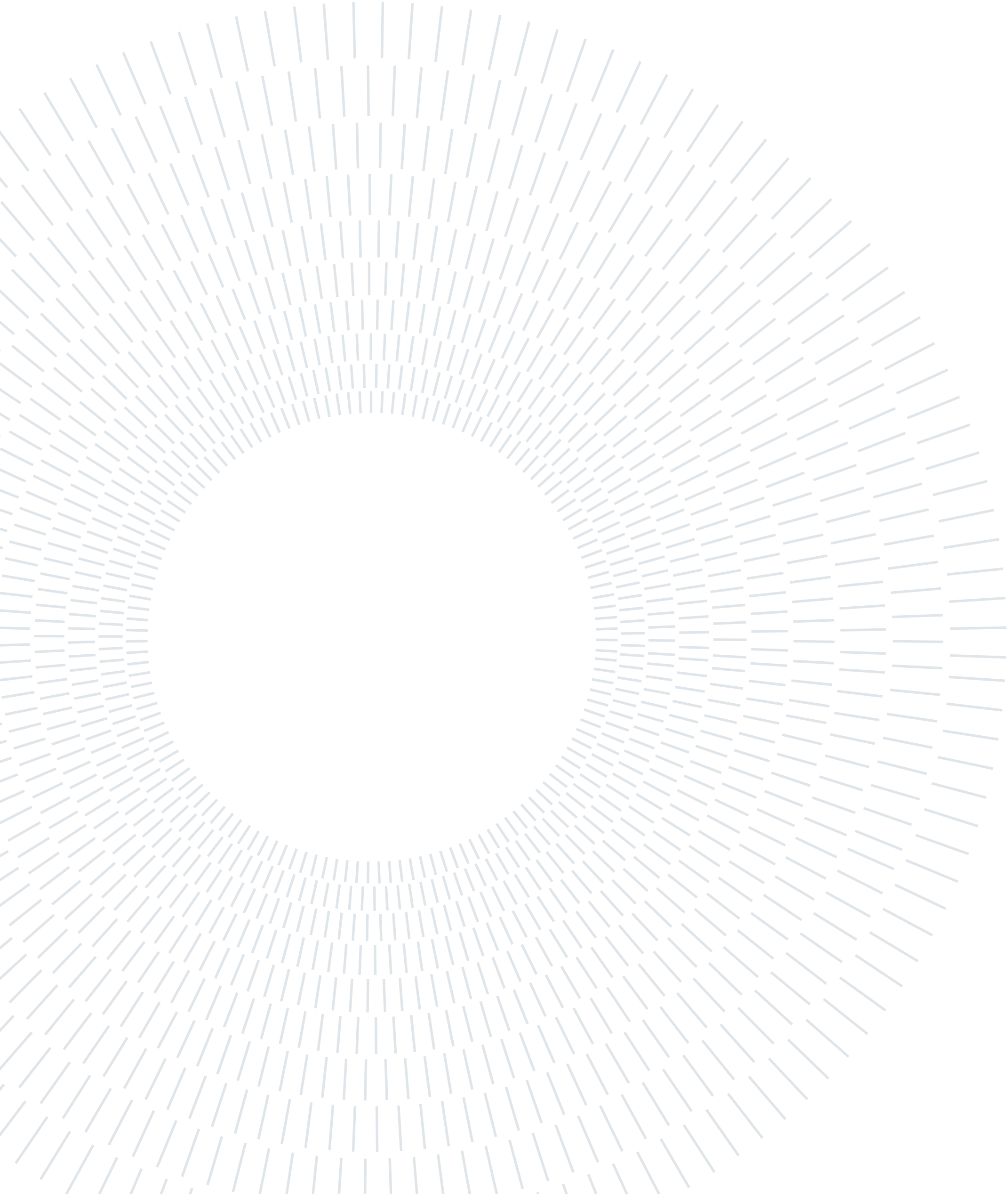

7 | Conclusions and Future Developments

Throughout this work we discussed Universal Photonic Processors (UPPs), devices capable of implementing an arbitrary unitary transformation between quantum states of light, as well as their calibration and operation. We introduced the general theory of how these devices are constructed and offer a rundown of the major technological platform used to produce them. Operating these devices effectively amounts to implementing the correct phase shifts to achieve the desired transformation.

Choosing the right phase shifts requires a series of nontrivial steps. In the first part of this work, we introduced a method to calibrate an N-mode UPP device built with the Clements configuration. In order to do so, we divided the phase shifters in two groups: *internal* phase shifters and *external* phase shifters. "Calibrating" in this context means finding the relation between the current flowing through the microheater and the amount of phase shift induced. We described a procedure with which to calibrate all internal phase shifters; by the end of this procedure, we could use the internal phase shifters to route the optical signal to any MZI in the network. Moreover, we introduced models to take into account specific phenomena arising from the FLM technology employed for the fabrication of the MZIs: we described how we model nonlinearities in the resistance, and we introduced a method to measure the thermal cross-talk between different parts of the network. Afterwards, we described our method to calibrate external phases using interferometric loops, including a discussion of how to take into account the cross-talk for this case. We also reported all the data obtained using the described procedures on two 6-mode UPP devices.

In the second part of this work, we used the calibration to implement unitary matrices on the two 6-mode devices. We discussed Clements' algorithm, which allowed us to retrieve the correct parameters for the matrix implementation, and we described how we solve the problem of inverting the relation between current and phase shifts. At this point, a series of measurements was performed on both UPP devices. In particular, on the Switching set we achieved an average fidelity of 0.99536 ± 0.00077 which is better than the current state of the art [10]; on the Haar Random set, we achieved an average fidelity of 0.89076 ± 0.04660 which is comparable to the state of the art, yet with room for improvement. The performance of the Haar Random set suggested us to go back and revisit the assumptions made along the way. In particular, we noticed that the basic building block of Clements' algorithm did not take into account the common mode phase of MZIs. Thus, we described a novel method to recover the correct phase shifts through a remapping of the phases; moreover, we analysed the effects of thermal cross-talk on the common mode phase, extracting a more refined model. The final model, however, requires a calibration with additional measurements on all the MZIs of the interferometric mesh. In order to have a first experimental hint of the validity of the model we performed one measurement on one MZI and we found that that this additional effect will play an important role to improve the fidelity of the UPP when implementing Haar random transformations.

In the future we expect to carry out the measurement for all MZIs as well as a new measurement of Haar Random matrices using a complete calibration of the refined model. The excellent performance of the device on the Switching set make us envisage that similar fidelities can be achieved on the Haar Random set also, and our aim for the future is to confirm experimentally these indications.

Bibliography

[1] E. Miller et al. “Integrated Optics: An Introduction”. In: *The Bell System technical journal* 48 (1969), pp. 2059–2069. DOI: `10.1002/j.1538-7305.1969.tb01165.x`.

[2] R. G. Hunsperger. *Integrated Optics, Theory and Technology*. 6th ed. Springer, 2009.

[3] M. Reck et al. “Experimental realization of any discrete unitary operator”. In: *Physical Review Letters* 73 (1994), pp. 58–61. DOI: `10.1103/PhysRevLett.73.58`.

[4] W. R. Clements et al. “Optimal design for universal multiport interferometers”. In: *Optica* 3 (2016), pp. 1460–1465. DOI: `10.1364/OPTICA.3.001460`.

[5] N. C. Harris et al. “Linear programmable nanophotonic processors”. In: *Optica* 5.12 (Dec. 2018), pp. 1623–1631. DOI: `10.1364/OPTICA.5.001623`.

[6] D. A. B. Miller. “Self-configuring universal linear optical component”. In: *Photon. Res.* 1.1 (June 2013), pp. 1–15. DOI: `10.1364/PRJ.1.000001`.

[7] Y. Shen et al. “Deep learning with coherent nanophotonic circuits”. en. In: *Nature Photonics* 11.7 (July 2017), pp. 441–446. ISSN: 1749-4893. DOI: `10.1038/nphoton.2017.93`.

[8] A. Annoni et al. *Unscrambling light-automatically undoing strong mixing between modes*. June 2017. DOI: `https://doi.org/10.1038/lsa.2017.110`.

[9] S. Rahimi-Keshari et al. “Direct characterization of linear-optical networks”. In: *Opt. Express* 21.11 (June 2013), pp. 13450–13458. DOI: `10.1364/OE.21.013450`.

[10] C. Taballione et al. “A universal fully reconfigurable 12-mode quantum photonic processor”. In: *Materials for Quantum Technology* 1.3 (Aug. 2021), p. 035002. DOI: `10.1088/2633-4356/ac168c`.

[11] J. Carolan et al. “Universal linear optics”. In: *Science* 349.6249 (2015), pp. 711–716. DOI: `10.1126/science.aab3642`.

[12] F. Hoch et al. *Boson Sampling in a reconfigurable continuously-coupled 3D photonic circuit*. 2021. arXiv: `2106.08260 [quant-ph]`.

[13] C. Sparrow et al. “Simulating the vibrational quantum dynamics of molecules using photonics”. In: *Nature* 557.7707 (2018), pp. 660–667. DOI: `10.1038/s41586-018-0152-9`.

[14] J. Carolan et al. “Variational quantum unsampling on a quantum photonic processor”. In: *Nature Physics* 16.3 (2020), pp. 322–327. DOI: `10.1038/s41586-018-0152-9`.

[15] L. Chen et al. “Photonic Switching for Data Center Applications”. In: *IEEE Photonics Journal* 3.5 (2011), pp. 834–844. DOI: `10.1109/JPHOT.2011.2166994`.

[16] R. Raussendorf, D. E. Browne, and H. J. Briegel. “Measurement-based quantum computation on cluster states”. In: *Phys. Rev. A* 68 (2 Aug. 2003), p. 022312. DOI: `10.1103/PhysRevA.68.022312`.

[17] R. Raussendorf and H. J. Briegel. “A One-Way Quantum Computer”. In: *Phys. Rev. Lett.* 86 (22 May 2001), pp. 5188–5191. DOI: `10.1103/PhysRevLett.86.5188`.

[18] Y. LeCun, Y. Bengio, and G. Hinton. “Deep learning”. en. In: *Nature* 521.7553 (May 2015), pp. 436–444. ISSN: 0028-0836, 1476-4687. DOI: `10.1038/nature14539`.

[19] N. H. Farhat et al. “Optical implementation of the Hopfield model”. In: *Appl. Opt.* 24.10 (May 1985), pp. 1469–1475. DOI: `10.1364/AO.24.001469`.

[20] A. C. Selden. “Pulse transmission through a saturable absorber”. In: *British Journal of Applied Physics* 18.6 (June 1967), pp. 743–748. DOI: `10.1088/0508-3443/18/6/306`.

[21] Y. A. Vlasov and S. J. McNab. “Losses in single-mode silicon-on-insulator strip waveguides and bends”. In: *Opt. Express* 12.8 (Apr. 2004), pp. 1622–1631. DOI: `10.1364/OPEX.12.001622`.

[22] X. Chen et al. “The Emergence of Silicon Photonics as a Flexible Technology Platform”. In: *Proceedings of the IEEE* 106.12 (2018), pp. 2101–2116. DOI: `10.1109/JPROC.2018.2854372`.

[23] F. Morichetti et al. “Roughness Induced Backscattering in Optical Silicon Waveguides”. en. In: *Physical Review Letters* 104.3 (Jan. 2010), p. 033902. ISSN: 0031-9007, 1079-7114. DOI: `10.1103/PhysRevLett.104.033902`.

[24] J. Teng et al. “Athermal Silicon-on-insulator ring resonators by overlaying a polymer cladding on narrowed waveguides”. EN. In: *Optics Express* 17.17 (Aug. 2009), pp. 14627–14633. ISSN: 1094-4087. DOI: `10.1364/OE.17.014627`.

[25] M. Mendez-Astudillo et al. “Compact thermo-optic MZI switch in silicon-on-insulator using direct carrier injection”. EN. In: *Optics Express* 27.2 (Jan. 2019), pp. 899–906. ISSN: 1094-4087. DOI: `10.1364/OE.27.000899`.

[26] G. T. Reed et al. “Silicon optical modulators”. en. In: *Nature Photonics* 4.8 (Aug. 2010), pp. 518–526. ISSN: 1749-4893. DOI: `10.1038/nphoton.2010.179`.

[27] S. Stepanov and S. Ruschin. “Phase and amplitude modulation of light by light in silicon-on-insulator waveguides”. en. In: *Electronics Letters* 41.8 (Apr. 2005), pp. 477–478. ISSN: 1350-911X. DOI: `10.1049/el:20058449`.

[28] X. Xiao et al. “High Speed Silicon Photonic Modulators”. In: *Optical Fiber Communication Conference*. Optica Publishing Group, 2017, Tu2H.1. DOI: `10.1364/OFC.2017.Tu2H.1`.

[29] N. C. Harris et al. “Quantum transport simulations in a programmable nanophotonic processor”. en. In: *Nature Photonics* 11.7 (July 2017), pp. 447–452. ISSN: 1749-4893. DOI: `10.1038/nphoton.2017.95`.

[30] A. Politi et al. “Integrated Quantum Photonics”. In: *IEEE Journal of Selected Topics in Quantum Electronics* 15.6 (2009), pp. 1673–1684. DOI: `10.1109/JSTQE.2009.2026060`.

[31] M. B. S. Martellucci A. N. Chester. *Advances in Integrated Optics*. Springer, 1994.

[32] J. Kim et al. “Hybrid integration methods for on-chip quantum photonics”. In: *Optica* 7.4 (Apr. 2020), pp. 291–308. DOI: `10.1364/OPTICA.384118`.

[33] K. Kato, M. Ishii, and Y. Inoue. “Packaging of large-scale planar lightwave circuits”. In: *IEEE Transactions on Components, Packaging, and Manufacturing Technology: Part B* 21.2 (1998), pp. 121–129.

[34] Y. Shi et al. “Fabrication of High Precision Self-Aligned V-Grooves Integrated on Silica-on-Silicon Chips”. In: *Photonics Technology Letters, IEEE* 26 (June 2014), pp. 1169–1171. DOI: `10.1109/LPT.2014.2316800`.

[35] T. Honjo, K. Inoue, and H. Takahashi. “Differential-phase-shift quantum key distribution experiment with a planar light-wave circuit Mach–Zehnder interferometer”. In: *Opt. Lett.* 29.23 (Dec. 2004), pp. 2797–2799. DOI: `10.1364/OL.29.002797`.

[36] T. A. Huffman et al. “Integrated resonators in an ultralow loss Si 3 N 4/SiO 2 platform for multifunction applications”. In: *IEEE Journal of selected topics in quantum electronics* 24.4 (2018), pp. 1–9.

[37] A. N. R. Ahmed et al. “Subvolt electro-optical modulator on thin-film lithium niobate and silicon nitride hybrid platform”. In: *Opt. Lett.* 45.5 (Mar. 2020), pp. 1112–1115. DOI: `10.1364/OL.381892`.

[38] C. Taballione et al. “8x8 reconfigurable quantum photonic processor based on silicon nitride waveguides”. In: *Opt. Express* 27.19 (Sept. 2019), pp. 26842–26857. DOI: `10.1364/OE.27.026842`.

[39] P. Zhang et al. “High-speed electro-optic modulator based on silicon nitride loaded lithium niobate on an insulator platform”. In: *Opt. Lett.* 46.23 (Dec. 2021), pp. 5986–5989. DOI: `10.1364/OL.446222`.

[40] C. G. Roeloffzen et al. “Low-loss Si3N4 TriPleX optical waveguides: Technology and applications overview”. In: *IEEE journal of selected topics in quantum electronics* 24.4 (2018), pp. 1–21.

[41] R. R. Gattass and E. Mazur. “Femtosecond laser micromachining in transparent materials”. en. In: *Nature Photonics* 2.4 (Apr. 2008), pp. 219–225. ISSN: 1749-4893. DOI: `10.1038/nphoton.2008.47`.

[42] K. M. Davis et al. “Writing waveguides in glass with a femtosecond laser”. In: *Opt. Lett.* 21.21 (Nov. 1996), pp. 1729–1731. DOI: `10.1364/OL.21.001729`.

[43] G. D. Valle, R. Osellame, and P. Laporta. “Micromachining of photonic devices by femtosecond laser pulses”. In: *Journal of Optics A: Pure and Applied Optics* 11.1 (Dec. 2008), p. 013001. DOI: `10.1088/1464-4258/11/1/013001`.

[44] R. Osellame, G. Cerullo, and R. Ramponi. *Femtosecond Laser Micromachining: Photonic and Microfluidic Devices in Transparent Materials*. Springer, 2012.

[45] G. Corrielli, A. Crespi, and R. Osellame. “Femtosecond laser micromachining for integrated quantum photonics”. en. In: *Nanophotonics* 10.15 (Nov. 2021), pp. 3789–3812. ISSN: 2192-8614. DOI: `10.1515/nanoph-2021-0419`.

[46] T. T. Fernandez et al. “Revisiting ultrafast laser inscribed waveguide formation in commercial alkali-free borosilicate glasses”. In: *Opt. Express* 28.7 (Mar. 2020), pp. 10153–10164. DOI: `10.1364/OE.387790`.

[47] G. Corrielli et al. “Rotated waveplates in integrated waveguide optics”. en. In: *Nature Communications* 5.1 (June 2014), p. 4249. ISSN: 2041-1723. DOI: `10.1038/ncomms5249`.

[48] G. Corrielli et al. “Symmetric polarization-insensitive directional couplers fabricated by femtosecond laser writing”. EN. In: *Optics Express* 26.12 (June 2018), pp. 15101–15109. ISSN: 1094-4087. DOI: `10.1364/OE.26.015101`.

[49] A. Ródenas et al. “Three-dimensional femtosecond laser nanolithography of crystals”. en. In: *Nature Photonics* 13.2 (Feb. 2019), pp. 105–109. ISSN: 1749-4893. DOI: `10.1038/s41566-018-0327-9`.

[50] G. D. Marshall et al. “Laser written waveguide photonic quantum circuits”. EN. In: *Optics Express* 17.15 (July 2009), pp. 12546–12554. ISSN: 1094-4087. DOI: `10.1364/OE.17.012546`.

[51] J. G. Titchener et al. “Scalable on-chip quantum state tomography”. en. In: *npj Quantum Information* 4.1 (Mar. 2018), pp. 1–6. ISSN: 2056-6387. DOI: `10.1038/s41534-018-0063-5`.

[52] A. Crespi et al. “Integrated multimode interferometers with arbitrary designs for photonic boson sampling”. en. In: *Nature Photonics* 7.7 (July 2013), pp. 545–549. ISSN: 1749-4893. DOI: `10.1038/nphoton.2013.112`.

[53] F. Ceccarelli et al. “Thermal Phase Shifters for Femtosecond Laser Written Photonic Integrated Circuits”. In: *Journal of Lightwave Technology* 37.17 (2019), pp. 4275–4281. DOI: `10.1109/JLT.2019.2923126`.

[54] F. Ceccarelli et al. “Low Power Reconfigurability and Reduced Crosstalk in Integrated Photonic Circuits Fabricated by Femtosecond Laser Micromachining”. en. In: *Laser & Photonics Reviews* 14.10 (2020), p. 2000024. ISSN: 1863-8899. DOI: `10.1002/lpor.202000024`.

[55] Z. Chaboyer et al. “Design and fabrication of reconfigurable laser-written waveguide circuits”. In: *Optics Express* 25.26 (2017), pp. 33056–33065.

[56] I. Dyakonov et al. “Reconfigurable photonics on a glass chip”. In: *Physical Review Applied* 10.4 (2018), p. 044048.

[57] R. M. Karp. “Reducibility among Combinatorial Problems”. In: *Complexity of Computer Computations: Proceedings of a symposium on the Complexity of Computer Computations, held March 20–22, 1972, at the IBM Thomas J. Watson Research Center, Yorktown Heights, New York, and sponsored by the Office of Naval Research, Mathematics Program, IBM World Trade Corporation, and the IBM Research Mathematical Sciences Department*. Ed. by R. E. Miller, J. W. Thatcher, and J. D. Bohlinger. Boston, MA: Springer US, 1972, pp. 85–103. ISBN: 978-1-4684-2001-2. DOI: `10.1007/978-1-4684-2001-2_9`.

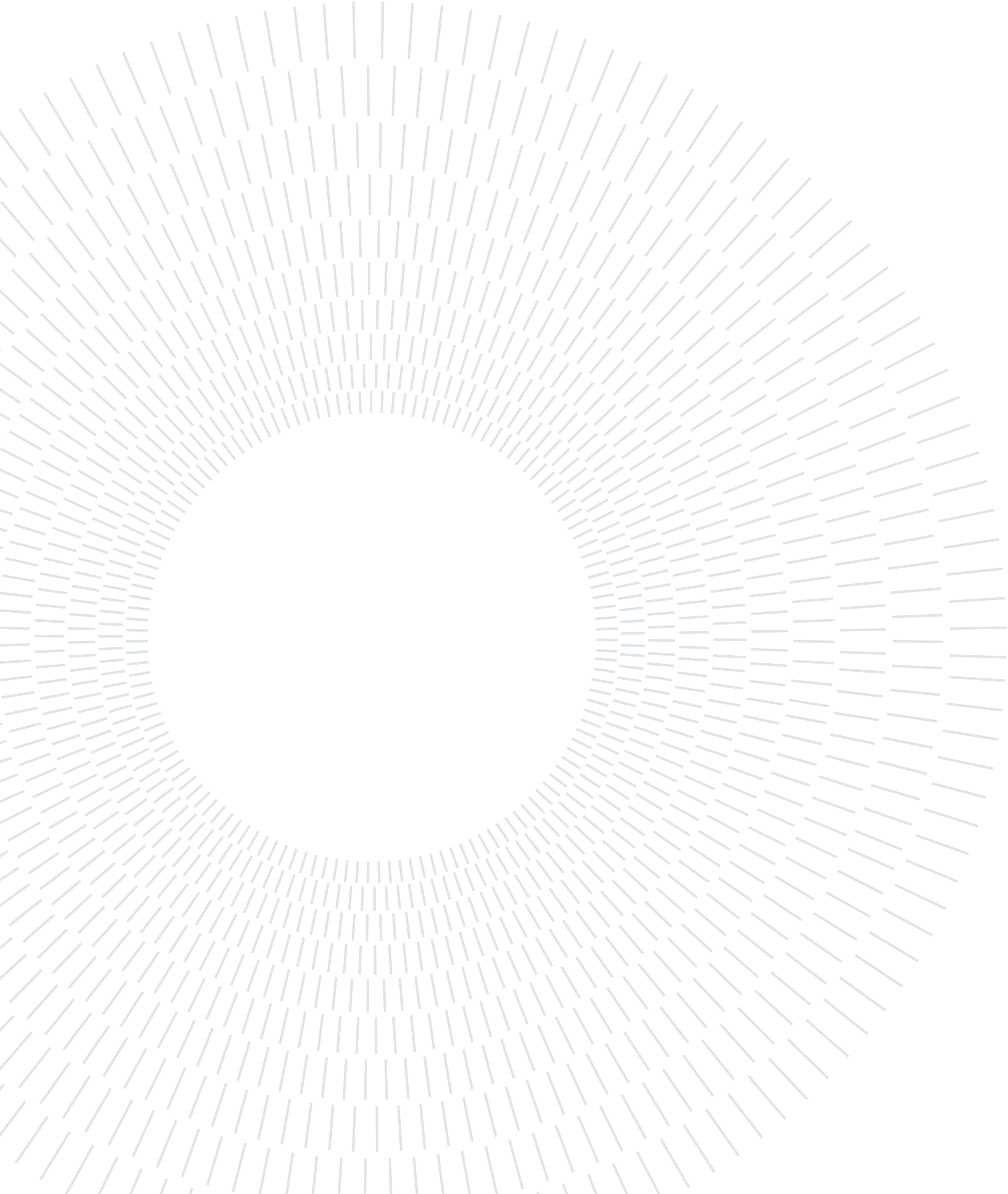

List of Figures

2.1 Step-index rectangular waveguide. The graph on the left shows the refractive index as a function of the x coordinate and a section of the waveguide. On the right, a three-dimensional view of the device. 4
2.2 Coupled waveguides in a three-dimensional view. 5
2.3 The two modes of the coupled waveguides. The refractive index profile is also shown for clarity. 6
2.4 Example field distribution where all the optical power is localised in one waveguide. The refractive index profile is also shown for clarity. 6
2.5 Schematic of a directional coupler. The waveguide distance is w_1 in the first and third section, and it becomes w_2 in the second section. The waveguides then interact for a total interaction distance d before parting ways in the third section once more. 7
2.6 Schematic of a Mach-Zehnder interferometer, made with a phase shifter embedded within two balanced directional couplers. The device can be reconfigured if the phase ϕ can be controlled. 9
2.7 Configurations for the implementation of a UPP using reconfigurable MZIs. (a) The topology proposed by Reck et al. [3]. (b) The topology proposed by Clements [4]. On the right, a schematic representation of the MZI that constitutes the elementary cell. Figures adapted from [5]. 11
2.8 Clements' algorithm for a 5-mode UPP. Each step determines T_{mn} for a certain m and n by nulling some entry of U. Figure from [4]. 15
2.9 Reconstruction of modes scrambled by time-varying mixing. a) Shows the 980nm laser configuration and the four modes; b1) shows the reference state used to initially configure the mode unscrambler with the laser turned off; b2) and b3) show the same measurement performed as soon as the perturbing laser source was turned on and after the application of the self-configuring algorithm respectively. Figure taken from [8]. 17

3.1 The scheme and physical realisation of the 26-mode UPP. Above, the schematic for the circuit. Below, the actual realisation; a) The whole chip seen from the top. b) Detail of the white inset of a). c) Phase versus voltage curve for all internal and external phase shifters on the chip. d) Transmission spectrum for an MZI with careful input polarization filtering. e) Setup of the experiment. Figures adapted from [29]. 22

3.2 The UPP presented by Carolan. a) Decomposition of a fully parametrized unitary for an m-mode circuit to realize any LO operation. Subunitaries D_i consist of MZIs $M_{i,j}$ built from phase shifters (yellow) and beam splitters, to control photon amplitudes ($\alpha_{i,j}$) and phases ($\varphi_{i,j}$). b) Multiphoton ensembles are generated with a dedicated setup. Photons are collected into polarization-maintaining fibers and delivered to the UPP via a packaged V-groove fiber array. The processor is constructed over six modes as a cascade of 15 MZIs, controlled with 30 thermo-optic phase shifters, and actively cooled with a Peltier cooling unit. Photons are then out-coupled into a second packaged array and counted by using a 12-channel Time-Correlated Single-Photon Counting (TCSPC) module. 24

3.3 Overview of the QuiX photonic processor. a) Schematic and SEM picture of the cross-section used for the waveguides. b) Functional design of the 12-modes photonic processor. The blue line represents a TBS that is implemented as an MZI with two 50:50 directional couplers (black lines) and a thermo-optic PS in red. c) Picture of the photonic assembly of the 12-modes processor as mounted inside the control box. d) Schematic for the QuiX control system. Figure from [10]. 26

3.4 Femtosecond Laser Micromachining process. a) Schematic of the laser incident on a transparent material. b) Diagram of the excitation of electrons to the conduction band. c) Microscope images showing the large variation in the feature characteristics depending on the experimental conditions. Left: single 10-nJ pulse and right: 25,000 5-nJ pulses at a frequency of 25 MHz (both with the same focal spot). Figure from [41]. 27

3.5 Timescale of the processes the material goes through after the interaction with a femtosecond laser pulse. The green bars represent the typical timescale; notice that while the interaction happens in a few femtoseconds, the "aftermath" of the interaction within the material may last for several microseconds. Figure from [41]. 29

3.6 The temperature profile induced by a resistive microheater. 1-4 are waveguides (size not to scale); 1-2 may belong to the reconfigurable MZI of the microheater, 3-4 may belong to a different one. The temperature profile clearly extends beyond just waveguide 1, inducing thermal cross-talk. Figure adapted from [55]. 32

3.7 The effect of adding a trench in an FLM device. a) Shows the device without a trench, with the waveguide structure detailed at the top. b) Shows the device with a trench; comparing this with a) the reach of the temperature profile is clearly reduced as highlighted below. Figure from [55]. 34

3.8 The structure of the reconfigurable MZIs in state of the art FLM UPPs. a) Basis structure of the device with no isolation structures. b) Cross section of the device with deep isolation trenches. c) Cross section of the device with the bridge waveguide. d) Photomicrograph of the isolation trenches (D_t = 150, 300, 450 µm) seen through the side of the substrate. e) Photomicrograph of the bridge waveguide seen through the side of the substrate. Figure from [54]. 36

4.1 The UPP device labeled A. The circuit is connected to the interposer board with the red cables with the pins provided by the printed circuit boards. The black cable instead connects the ground. 37

4.2 The scheme for the UPPs on which all experiments have been performed. The thin dark lines correspond to FLM waveguides; the yellow thicker lines correspond each to a microheater; the distance between straight waveguides is 80 nm while the distance between two ports is 127 nm. Around each microheater is a pair of deep trenches separating each waveguide with the next waveguide over. The group of 2 horizontally aligned directional couplers with microheaters constitutes an MZI of the network. 38

4.3 The electrical scheme of the UPP in the ideal case. There are 30 resistive microheaters, with resistance values R_i ($1 \leq i \leq 30$), all connected to the same ground node. In reality, between the common node of the microheaters and the ground a small resistor should be considered, with a ground resistance R_g. The electrical control can provide up to 24 mA or 5 V to each resistor separately. 38

4.4 The optical setup of the experiments. The laser sources (785 nm, 793 nm) are coupled into the single-mode fiber through a NA = 0.25 lens; the alignment is performed manually using a pair of mirrors, represented here by thick lines. After this stage, the fiber is aligned to an input port of the UPP; the light coming out of the UPP is then collected by another lens (NA = 0.68) in such a way that two output ports are focused on two different photodiodes (PD). 40
4.5 The Qontrol devices used for the current control. On the left, the main board with the four Q8iv microcontrollers mounted on top. On the right, the interposer board that allows easy connection between the channels and the actual circuit. 41
4.6 The automated stages used for the experiments. The Mercury Servo Controllers are shown on the left while the moving parts are shown on the right. The moving parts also have an extra manipulator (manual) used to adjust the position of the objective along the optical axis. 42

5.1 The compact version of the diagram of the 6-mode UPP. The MZIs are numbered according to the order in which Clements' algorithm solves their parameters (Section 2.2.4). With reference to Figure 4.2, a crossing in this diagram corresponds to an entire MZI including both microheaters. Then, MZI 1 in this diagram corresponds with the MZI circled in green in Figure 4.2. 46
5.2 Two typical graphs obtained from a current ramp measurement. The blue dots correspond to the measured data, while the curve fit is shown in black. Minima and maxima correspond respectively to reflection points and transmission points. 48
5.3 Dependence of $\Delta\theta$ on current squared. These results were extracted by inverting the transmission function of an internal phase of device B, obtaining the argument of the function. The data deviate substantially from linerarity in I^2. 49
5.4 The compact version of the diagram of the 6-mode UPP with the diagonals highlighted. The MZIs are numbered according to the order in which Clements' algorithm solves their parameters (Section 2.2.4). 51
5.5 Schematic representation of the setup to measure the cross-talk. T_1 is the temperature profile induced by the microheater of MZI 1 and the arrow represents the direction of increasing temperature. In this example, the result of the curve fit would determine the element α_{21}. 54

5.6 Typical graphs of cross-talk measurements. Both measurements have been performed on device B and represent different tuning coefficients. On the left, we are measuring the effect that an MZI has on the first neighbor located above it; the coefficient turns out to be negative, as evidenced by the negative derivative at zero of the sinusoid. On the right, we are measuring the effect that an MZI has on the second neighbor below; the coefficient is positive, but quite small, hence the graph looks more similar to a line than a sinusoid. 54

5.7 The explanation for the negative cross-talk coefficients. On the right, MZI 1 is inducing cross-talk on MZI 2; on the left, the situation is reversed. The blue (shorter) arrows represent the temperature gradient that increases $\Delta\theta$ according to Equations 3.6 and 5.2; the red (longer) arrows represent the gradient of temperature induced by the microheater. Since the cross-talk induced by the heater from below acts against the temperature gradient of increasing $\Delta\theta$, the resulting cross-talk coefficient α_{12} is negative. 57

5.8 The "virtual" MZI created using an arrangement of four MZIs. a) The arrangement. The dotted crossings represent MZIs that have been set to the reflection point, effectively creating a bridge to the next straight waveguide. The crossings with a thick bar represent MZIs that have been set to the $\theta = \pi/2$ point. The thick yellow line represents the microheater of MZI 3, which is the microheater that determines the parameter ϕ of Equation 5.16. b) The topology of the arrangement shown without any features. 58

5.9 A 5-by-5 network bare of any labels. Every crossing corresponds to an MZI. 59

5.10 Construction of equivalent circuits. In the three figures, the red squares (always on the left) signify the addition of a phase φ on that waveguide, while the blue squares (always on the right) signify the subtraction by a phase φ. The dashed shape can enclose any number of MZIs. In this Figure we report three examples of circuits equivalent to the 6-mode UPP. 60

5.11 A convenient equivalent circuit for the 6-mode UPP. We choose to add the unknown static phase on one side, and on the other side we interpret all results as having already subtracted this phase every time we calculate the static phase belonging to different loops. 61

6.1 Three examples taken from the results of the Switching set; the first coloumn shows the ideal target matrix, the second and third show the measurements on device A and B respectively. The first matrix is the identity, the second matrix is the Pauli X^3, the third matrix swaps inputs 2 and 3. In these graphs the numbering of the inputs and outputs is initialised to 0 rather than 1. 70
6.2 The histogram of the fidelities obtained from the 57 measurements. The distribution is roughly uniform across a large range centered around the mean, with a small set of matrices responsible for dragging the average down even further. 71
6.3 An example of Haar random matrix obtained with device A; the target matrix is on the left, while the measured matrix is on the right. This matrix was implemented with a fidelity of 0.953. The measured matrix and the target matrix are clearly different. 71
6.4 The diagram of a 3-mode network with an added common mode phase. The external phase shifter related to MZI 3 is highlighted by the thick yellow line. a) The network where the internal phase of MZI 1 is not set to any specific value. MZI 1 then adds some common mode phase, which acts as an extra phase on the middle waveguide. b) The case when MZI 1 is set to the reflection point ($\theta_1 = \pi$), represented by dotted lines and bridges between straight waveguides. Since the common mode phase is $\theta_1/2 + \pi/2$, the field on the middle waveguide picks up an extra π phase. If this phase was not accounted for, the field would only pick up the phase due to the propagation in the straight waveguide. 73
6.5 The diagram of a 4-mode network, with the external phase shift ϕ_3 highlighted in yellow. The effects of a common mode phase from the MZIs 1 and 4 are highlighted here; effectively, they contribute with their common mode phase to ϕ_3 with opposite signs. 73
6.6 The linear graph extracted from the method described in this section. We see clearly that the linear coefficient is larger than 0.5, indicating that the cross-talk has a substantial impact on the common mode phase. 76

List of Tables

5.1 The data measured for device A using the procedure detailed in this section. The numbering of the MZIs follows Figure 5.1. 52

5.2 The data measured for device B using the procedure detailed in this section. The numbering of the MZIs follows Figure 5.1. 53

5.3 The data measured for device A using the procedure detailed in this section, for external phase shifters only. The numbering of the MZIs follows Figure 5.1. The values I_π and I_0 in this context are the currents needed to set the interfermetric loop centered around the microheater to reflection and transmission respectively. 62

6.1 The fidelities measured on the three different sets of switching matrices. The data reported here is given by the average fidelity of the set plus or minus the standard deviation over the set. 69

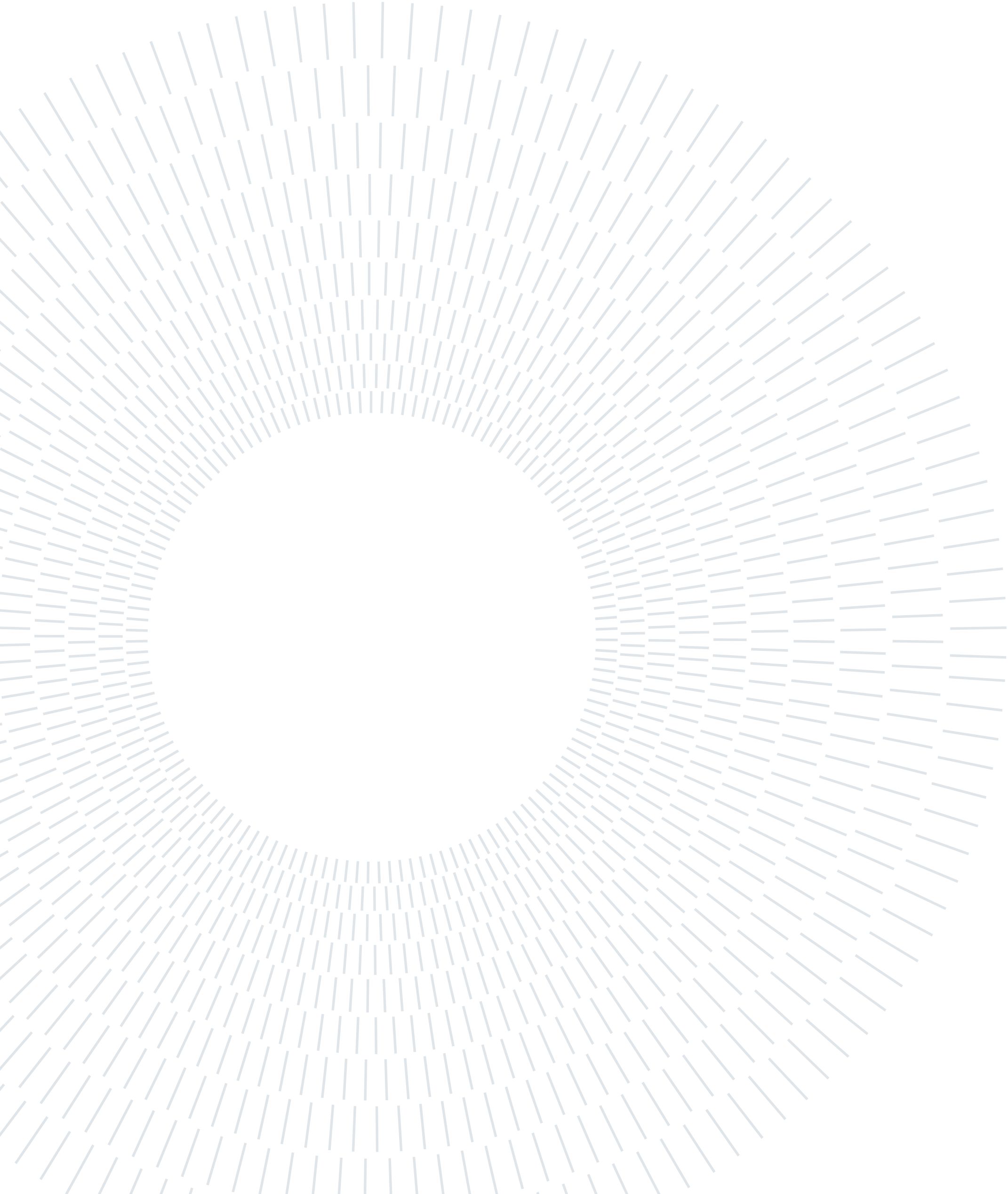

Acknowledgements

In questo percorso di cinque anni ho avuto modo di imparare molte nozioni accademiche, e sono grato per tutto quello che i miei professori mi hanno saputo insegnare. Ma ho imparato molto anche al di fuori dell'accademia in senso stretto, sono cresciuto attraverso esperienze di vita e lavorative che nessun libro potrebbe mai replicare.

Ringrazio tutte quelle persone senza le quali questo percorso non sarebbe stato lo stesso; a partire dai miei genitori Lidia e Francesco, senza il supporto dei quali nulla di tutto ciò sarebbe mai potuto accadere. Ringrazio i miei nonni, i quali non hanno mai smesso di credere in me. Ringrazio gli amici che mi hanno accompagnato e aiutato per gran parte di questo percorso: Matteo C., Matteo T., Federico, Marta, Venus.

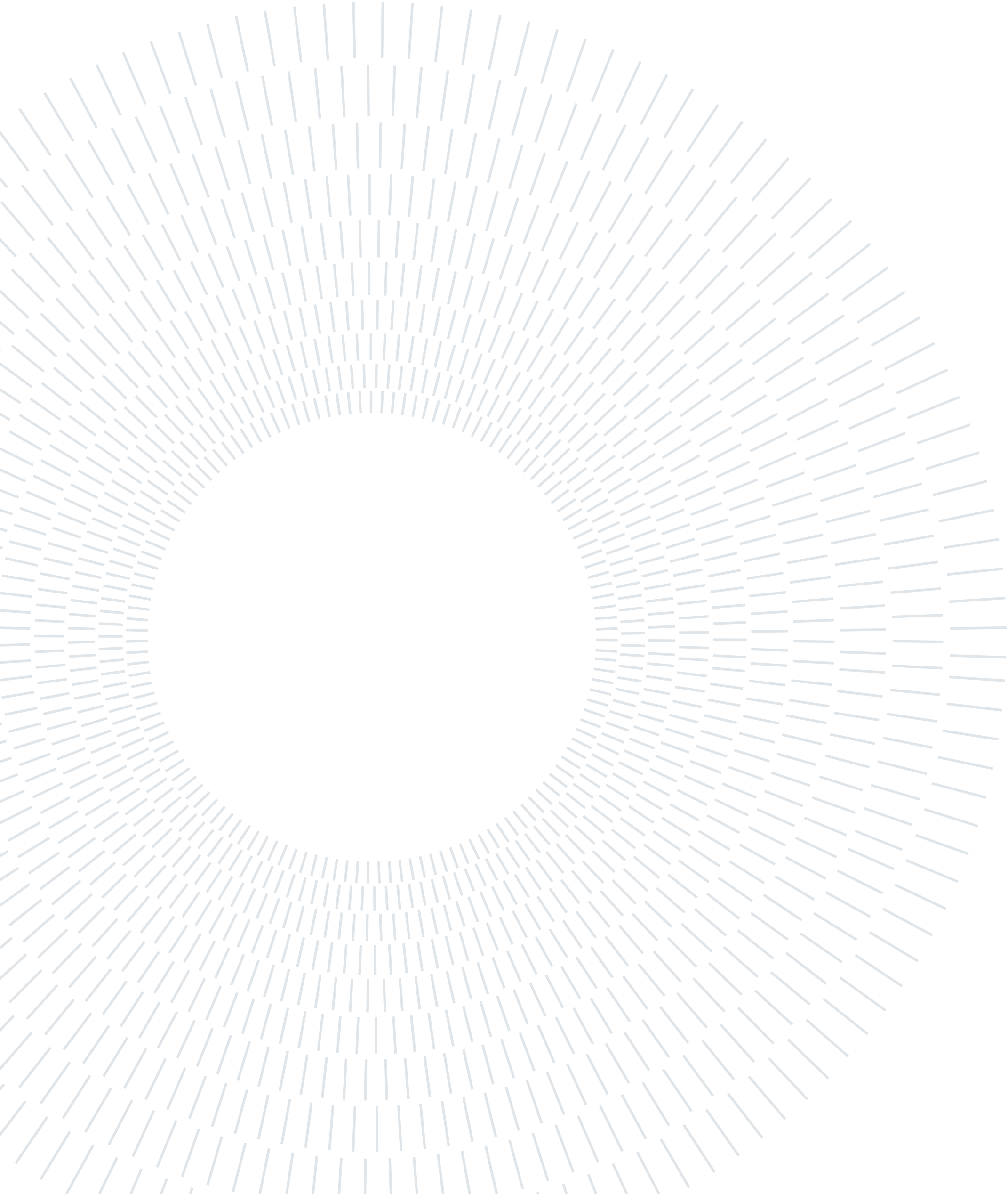Infine, ringrazio le persone che mi hanno sostenuto durante il periodo di tesi, amici ancor prima che tutori: Francesco, Ciro, Riccardo, Andrea. Questa tesi conclude un percorso che mi ha insegnato quanto varia e inaspettata sia la vita stessa, oltre le parole ed oltre l'immaginazione.